SINGLET FISSION IN LOW BANDGAP π-CONJUGATED POLYMERS FOR ORGANIC PHOTOVOLTAIC APPLICATIONS

by

Uyen Nguyen Vu Huynh

A dissertation submitted to the faculty of
The University of Utah
in partial fulfillment of the requirements for the degree of

Doctor of Philosophy

in

Physics

Department of Physics and Astronomy

The University of Utah

August 2015

Copyright © Uyen Nguyen Vu Huynh 2015

All Rights Reserved

The University of Utah Graduate School

STATEMENT OF DISSERTATION APPROVAL

The dissertation of **Uyen Nguyen Vu Huynh**

has been approved by the following supervisory committee members:

Zeev Valentine Vardeny	, Chair	**05/05/2015** Date Approved
Oleg Starykh	, Member	**05/05/2015** Date Approved
Ajay Nahata	, Member	**05/05/2015** Date Approved
Jordan Gerton	, Member	**05/05/2015** Date Approved
Gordon Thomson	, Member	**05/05/2015** Date Approved

and by **Carleton DeTar** , Chair/Dean of

the Department/College/School of **Physics and Astronomy**

and by David B. Kieda, Dean of The Graduate School.

ABSTRACT

Singlet fission (SF) is a process that occurs in some organic semiconductors whereby the photoexcited singlet exciton (SE) undergoes internal conversion to a multiexciton triplet-triplet (TT) state, which subsequently splits into two independent triplet excitons. This process was first observed in crystalline acenes (most notably pentacene) in the 1960s. Renewed interest on singlet fission has been seen dramatically increased in recent years because of its potential in harvesting charges from the triplet excitons in organic photovoltaic cells, thereby doubling the photocurrents. It was shown that the cell external quantum efficiency may exceed 100%, and thus it could potentially overcome the Shockley-Queisser PV efficiency limit under the sun illumination.

In this work, we used various optical techniques in our research arsenal to uncover the intrachain singlet fission in a new class of OPV materials, namely low bandgap π-conjugated polymers, which was used as the electron donor in bulk hetero-junction solar cells. These copolymers produced a record high power conversion efficiency of ~ 8% in an optimum OPV device. Particularly, we introduced two new novel techniques, the nanosecond to millisecond transient photo-induced absorption and transient magneto-photoinduced absorption, dubbed t-PA and t-MPA, respectively, to unravel the population exchange between the singlet exciton and triplet pair (TT) state, which is a new quantum state constituted by two correlated triplet excitons. Using the t-PA in

picosecond time domain, we detected the TT state that appears simultaneously with the singlet exciton SE within 300fs time resolution of our experimental setup. The picosecond t-MPA technique further elucidates the nature of TT state, showing its coupling to the SE through their spin exchange interaction with the interaction strength as large as ~30mT. Using the t-MPA together with the ns t-PA, we found that the TT state later separates into two uncorrelated triplets in microsecond time domain.

In the copolymers/$PC_{71}BM$ blend, which was used as the active layer in OPV devices, the TT state dissociates, by the unique spin conserved process, into one polaron pair in triplet configuration, PP_T ; leaving behind one triplet on the copolymer chains within 20ps. The PP_T could either dissociate into free charges to generate photocurrents in cell devices or recombine back to triplet excitons. Here we observed the "back reaction", PP_T → triplets, in nanosecond time regime, which we identify as a loss mechanism for charge photogeneration in solar cell devices. We also introduce a method to reduce the carrier loss mechanism by the "back reaction" of PP into triplet excitons on the copolymer chains, by adding spin ½ radicals; this method may be especially suitable for copolymer-based OPV cells.

To my family

TABLE OF CONTENTS

ACKNOWLEDGEMENTS

I would like to express the deepest gratitude to my advisor, Prf. Z. Valy Vardeny, whose persistent guidance and support let me fulfill my dream throughout my years at the Physics Department. His wisdom kept me constantly engaged with my research and his steady enthusiasm and dedication to research has planted the seeds of my expertise in future academic careers that I want to pursue. I am grateful to Prf. Eitan Ehrenfreund and Prf. Sumit Mazumdar for enlightening me with their beautiful theoretical models, as well as Prf. Yang Yang and his team for synthesizing the novel copolymer PDTP-DFBT. I would also like to express my sincere gratitude to my supervisory committee members, Prf. Oleg Starykh, Prf. Ajay Nahata, Prf. Gordon Thomson, and Prf. Jordan Gerton, for their guidance over the years.

I am thankful to Prf. Yan Li for sharing the fancy cryostat equipment for low temperature and magnetic field measurements and Prf. Tho Nguyen for being my best friend in the US as well as the “acting” second mentor, who has introduced me to Physics and been sharing with me his enthusiasm about our research topic.

I would like to thank Dr. Mathew Delong, Dr. Zhiheng Liu, and Wayne Wingert (when alive) for their technical assistance; my current group members, Ryan MacLaughlin and Dr. Evan Lafalce for their help to tame my English; Dr. Dali Sun, Dr. Charlie Zhang, Dr. Tek Basel, Yaxin Zhai, and Run Li for their valuable discussions,

support, and collaboration; my former group members, Dr. ChuanXiang Sheng and Dr. Bill Pandit for teaching me the ultrafast measurement; and Dr. Ella Ollejnik and Dr. Bhoj Gautam for useful discussions.

I am indebted to my family for their love, care, support, and motivation. Their spiritual encouragement helps me survive the stress on the way to pursue my PhD.

CHAPTER 1

INTRODUCTION

Polymeric materials have been used since prehistoric time in the form of wood, bone, skin, and fibers. These saturated polymers, in which four valence electrons of carbon are used up in covalent bonds, are insulators. In 1976, the conducting polymers were discovered by a talented group of scientists, Alan MacDiarmid, Hideki Shirakawa, and Alan Heeger, who were awarded a Nobel Prize in Chemistry in 2000 [1,2]. The discovery promised a new generation of photonic materials which possess the electrical and optical properties of metals or semiconductors, but sustain the attractive mechanical properties and processing advantages of polymers. Nowadays, the conducting or conjugated polymers have been applied in a wide variety of optoelectronic applications such as: organic light emitting diodes (OLEDs) [3,4], organic photovoltaics (OPVs) [5,6], organic field effect transistors (OFETs) [7], organic spin valves (OSVs) [8,9], and recently in biosensing applications [10,11], although their applications are still behind those of their inorganic counterparts partly due to some issues of stability, scalability, and efficiency. Despite their shortcomings, the conjugated polymers still attract many researchers around the world as they try to understand the fundamental chemistry and physics of these systems.

1.1 π-Conjugated Polymers

Conjugated polymers are π-bonded carbon-based large molecules in which the fundamental monomer unit is repeated many times. The electronic configuration of carbon in its ground state is $1s^2 2s^2 2p^2$. To form bonds, one of carbon's 2s electrons is promoted to a 2p orbital for hybridization of orbitals which subsequently creates two sp^1, three sp^2, or four sp^3 hybrid states. The sp^2 hybridization configuration in which one 2s and two 2p electrons combine to form three sp^2 hybrid orbitals, leaving the $2p_z$ orbital perpendicular to them as shown in Figure 1.1a, is typically found in the conjugated polymers. In the case of ethane shown in Figure 1.1b, three sp^2 orbitals of one carbon atom overlap with two 2s orbitals of hydrogen and one sp^2 orbital from a second carbon atom to form σ-bonds lying within the plane of the molecule, while the two remaining $2p_z$ orbitals overlap above and below the molecule plane to form a delocalized π-bond. In the conjugated polymer, the π-bonding orbitals of successive carbons along the backbone overlap, leading to electron delocalization along the backbone of the polymer. This delocalized π-electron system is responsible for the electronic and optical properties of the polymers. The theoretical formation of molecular orbitals in conjugated polymers will be discussed in detail in the next section of this chapter. In general, the π-bonds between carbon atoms in polymers form molecular orbitals; the π-bonding orbital or π band is the lowest energy state, known as the Highest Occupied Molecular Orbital (HOMO) while the antibonding π^* orbital or π^* band is the higher energy state, referred to as the Lowest Unoccupied Molecular Orbital (LUMO). Since each carbon contributes a single p_z electron to the bond and according to the Pauli exclusion principle which allows only two electrons (spin up and spin down) per quantum state, the π band is filled

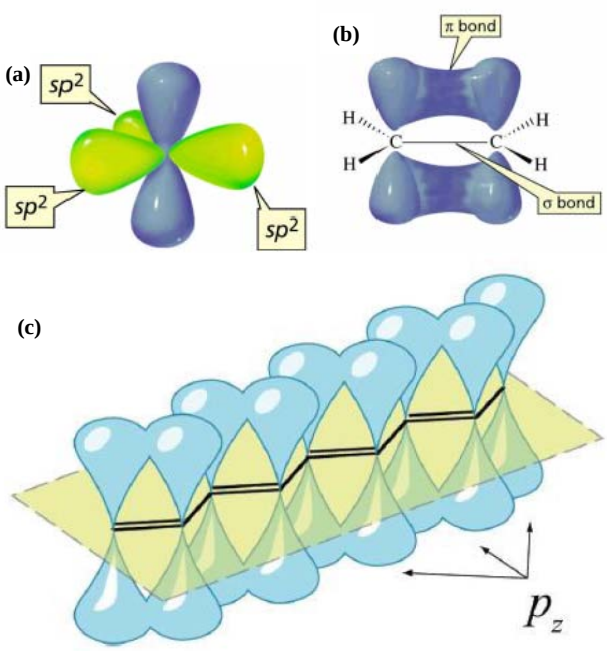

Figure 1.1: Formation of the π-bonding orbital (a) Schematic orbitals of a sp^2 hybridized carbon atom (green). Blue represents the p_z orbital perpendicular to the plane of the sp^2 orbitals. (b) π-bonding in ethene, the p_z orbital overlaps above and below the molecular plane formed by the σ-bonding. (c) A conjugated backbone showing the p_z orbitals overlapped.

and the π^* band is empty. Consequently, conjugated polymers are semiconductors whose energy gap E_g is the energy difference between the π band (HOMO) and the π^* band (LUMO). The size of the energy gap depends on the molecular structure of the unit cell, and can be easily controlled by design at the molecular level [12]. The typical energy gap of conjugated polymers is a few eV; 2.1 eV for MEH-PPV, for instance.

1.2 Symmetry Groups

The symmetry of linear polymer chains that possess a 2-fold rotation symmetry and a horizontal mirror plane is described by the C_{2h} point group [13]. The overall electronic wave function of linear polymers may be classified according to the symmetry operators.

If the molecular orbital wavefunctions change (do not change) sign under inversion operations, then they are named as u (g), and dubbed as B (A) if they change (do not change) sign under C_2 rotation operations. The irreducible representations of the C_{2h} point group to which the electronic wavefunctions of π-orbitals along the conjugated length belong can have either A_g or B_u symmetry [14]. Since the π-band (HOMO) in PCPs are even (under inversion operation), the ground state has A_g character. The next excited state (LUMO) carries B_u character and the state above that (LUMO+1) becomes A_g again, and so on. The term symbol describing different states of a polyatomic is $n^{2S+1}\Gamma$, where n is the overall quantum number, (2S+1) is the spin multiplicity (1 for singlet and 3 for triplet), and Γ is the irreducible representations of electronic wavefunctions. Therefore, the ground state exciton is labeled as 1^1A_g.

1.3 Optical Selection Rules

An optical selection rule is a condition constraining the physical properties of the initial and final states of an optical system that is necessary for an optical process (mostly absorption and emission of photon radiation) to occur with non-zero probability. The transition probability is governed by Fermi's Golden rule for the rate of a transition from an initial state $|\Psi_i\rangle$ to a final state $|\Psi_f\rangle$ as:

$$\omega_{fi}= \frac{dP_{fi}}{d_t} =\frac{2\pi}{\hbar}|H_{fi}|^2\delta(E_f-E_i), \tag{1.1}$$

where $H_{fi} = \langle\Psi_f|H_I|\Psi_i\rangle$, $H_I = \mathbf{p}.\mathbf{E}(t)$ is the interaction Hamiltonian, $\mathbf{E}(t)$ is the oscillating electric field of the light, and $\mathbf{p} = \sum_j e\boldsymbol{r}_j$ is the electric dipole moment operator.

Assuming the oscillating electric field to be $\mathbf{E}(t) = \mathbf{E}_0(e^{i\omega t} + e^{-i\omega t})$ where ω is the frequency of the light, we can rewrite equation (1.1) as

$$\omega_{fi} = \frac{dP_{fi}}{d_t} = \frac{2\pi}{3\hbar^2}|E_0|^2|\mu_{fi}|^2\,\delta(E_f - E_i \pm \hbar\omega), \tag{1.2}$$

where $\mu_{fi} = \langle\Psi_f|\mathbf{p}|\Psi_i\rangle$ is the transition dipole moment.

The transition dipole operator **p** is antisymmetric under the inversion symmetry. Thus for a transition to occur with non-zero probability, the transition dipole moment needs to be non-zero: the initial $|\Psi_i\rangle$ and final $|\Psi_f\rangle$ states must be of opposite parity. This means that the optical transitions are only allowed between the gerade, g , and ungerade, u, states with the same spin multiplicity: singlet to singlet or triplet to triplet, given that the electric dipole operator conserves total spin[15]. Note that the spin selection rule may be overrun by the spin orbital coupling which mixes singlet and triplet states and allows a spin-flip to occur [16].

The term “allowed or forbidden” in the optical selection rule discussed above often refers to the linear electric dipole transitions which have a much higher probability (or rate) than the alternative transitions which might be due to magnetic dipole moments, higher order electric dipole moments, or simply lack of the symmetry of the states caused by extrinsic factors such as disorder or applied electric field [17]. While those transitions may violate the optical selection rule, they are much weaker and take place on much longer time scales than purely allowed linear dipole transitions.

Conjugated polymers have inversion symmetry, which results in electronic states that possess either even (A_g) or odd (B_u) parity. If electron-electron interactions are neglected,

excited states with even symmetries are higher in energy than those with odd symmetry as seen in Figure 1.2, thus the ordering of the first two excited states is

$$E(1^1B_u) < E(2^1A_g)) \tag{1.3}$$

The electron-electron interaction may change the order of the first two excited states, bringing the 2^1A_g state below the 1^1B_u state, consequently affecting the optical properties of the PCP as [18]

$$E(2^1A_g) < E(1^1B_u) \tag{1.4}$$

Since the optical transition between the 2^1A_g and 1^1A_g are dipole-forbidden, the polymers of this type are nonluminescent as in the case of trans-polyacetylene and poly-diacetylene [19].

1.4 Frank-Condon Principle

The transition dipole moment matrix element, $\mu_{fi}= \langle\Psi_f|\mathbf{p}|\Psi_i\rangle$, governs the optical properties of conjugated polymers, including absorption, emission, etc. The Frank-Condon principle, a restatement of the Born-Oppenheimer approximation, provides a simple way to calculate it. Due to strong electron-phonon coupling, the wavefunctions describing the states which are dipole-connected are dependent on the electronic and nuclear (or vibrational) degrees of freedom, $|\Psi_{f,i}\rangle= |\Psi_{f,i}^{elec}\rangle |\Psi_{f,i}^{vib}\rangle$. The nuclear wavefunction $|\Psi_{f,i}^{vib}\rangle$ defines the motion of the nucleus in the electronic adiabatic

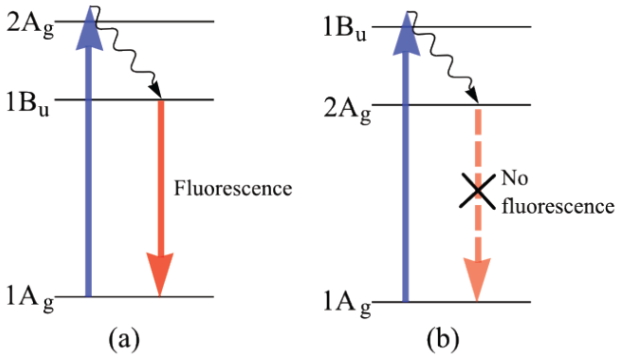

Figure 1.2: The excited state ordering of (a) $E(1B_u) < E(2A_g)$ which allows the polymer fluorescence. (b) $E(2A_g) < E(1B_u)$ for which fluorescence is forbidden.

potential energy surface. Since the nuclear Hamiltonian is coordinate-dependent and nuclear motions involve a different coordinate system, the normal coordinate [Q_k] is being used to describe their motion [20]. In that system, each vibrational mode has a coordinate and can be treated as a harmonic oscillator as displacements of the nuclei from their equilibrium positions are small. As seen in Figure 1.3a, the initial (ground) and final (excited) states have a shift in potential energy minimum in normal coordinate space.

The Frank-Condon principle assumes that electron transitions occur so fast that the heavier nuclei remain stationary. After the electronic transition takes place, the nuclei respond by moving along the adiabatic potential energy surface of the excited state to a new equilibrium position, bringing about a change of the molecule to the excited state configuration. This configurational change is known as relaxation (or reorganization) and the energy involved is known as the relaxation energy, E_{rel}. Emission follows the same route but in reversed order. In the potential surface energy diagram, the electron transition is vertical as shown in Figure 1.3b. The vibrational relaxation of the nuclei towards the bottom of the excited state's adiabatic energy potential leads to the so-called

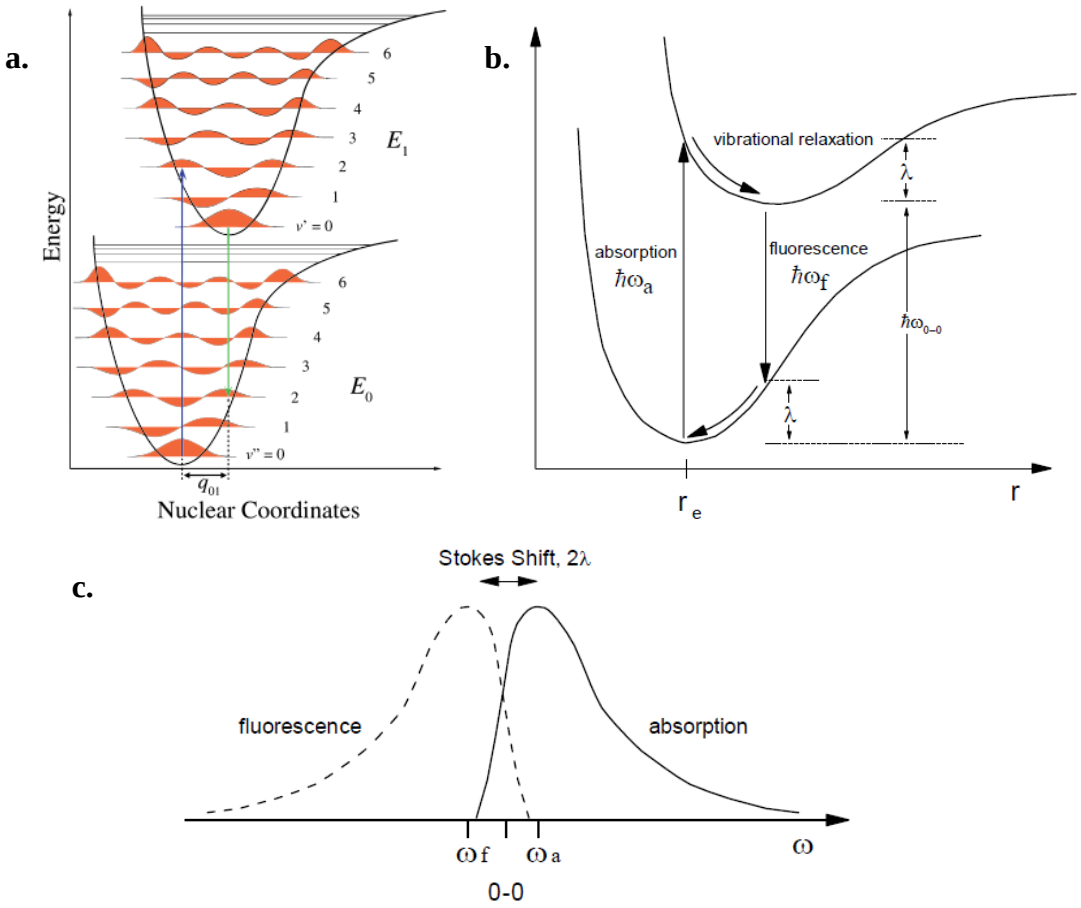

Figure 1.3: The Frank-Condon principle (a) Potential energy surface of the ground and excited states with the vibronic modes of wavefunctions plotted in the nuclear coordinate Q. The absorption and fluorescence electronic transitions are vertical according to the Frank-Condon principle. (b) Vibrational relaxation to the bottom of the potential surface upon the absorption and fluorescence, each with relaxation energy λ. (c) A mirror image of absorption and emission spectrum shows a stokes shift of 2λ (adapted from http://web.mit.edu/5.33/www/lec/spec6.pdf).

"Stokes-shift" between the absorption and emission spectra (Figure 1.3c). In general, the "Stokes-shift" can be attributed to the combined effect of vibrational relaxation of nuclei and exciton migration to longer and lower energy sites; the latter results in sharper emission spectra than absorption spectra.

The Frank-Condon principle allows the separation the nuclear and electronic parts of

the wavefunction $|\Psi_{f,i}\rangle = |\Psi_{f,i}^{elec}(Q_k)\rangle\,|\Psi_{f,i}^{vib}\rangle$, where the $|\Psi_{f,i}^{elec}(Q_k)\rangle$ represents the electronic part in the normal coordinate Q_k, and $|\Psi_{f,i}^{vib}\rangle$ represents the nuclear part associated with the $|\Psi_{f,i}^{elec}(Q_k)\rangle$. The transition dipole moment then becomes

$$\mu_{fi} = \langle\Psi_f|\mathbf{p}|\Psi_i\rangle = \langle\langle\Psi_f^{vib}|\langle\Psi_f^{elec}(Q_k)|\boldsymbol{p}|\Psi_i^{elec}(Q_k)\rangle\,|\Psi_i^{vib}\rangle\rangle = \langle\Psi_f^{elec}(Q_k)\big|\boldsymbol{p}\big|\Psi_i^{elec}(Q_k)\rangle$$

$$\mu_{fi} = \langle\Psi_f^{vib}|\Psi_i^{vib}\rangle = \mu_{fi}^{e}(Q_k)\,\langle\Psi_f^{vib}|\Psi_i^{vib}\rangle \qquad (1.5)$$

$\langle\Psi_f^{vib}|\Psi_i^{vib}\rangle$ is the overlap integral of nuclear wavefunctions, and $\mu_{fi}^{e}(Q_k)$ is the electric dipole moment evaluated at the equilibrium value of Q_k in the initial state.

The intensities of a given transition are proportional to the amplitude square of its dipole moment matrix element: $|\mu_{fi}|^2 = |\mu_{fi}^{e}(Q_k)|^2\,|\langle\Psi_f^{vib}|\Psi_i^{vib}\rangle|^2$. The set of all vibrational transitions belonging to a given electronic transition is called a band system. The intensities of various vibrational bands are governed by the squares of the vibrational overlap integral, which is called the Frank-Condon factor.

Ideally, an optical band, either absorption or emission, contains a series of sharp lines with spacing gap of $N\omega_{vib}$ and with weighting factors governed by the Frank-Condon factor. In reality, the line shape of transitions will have some broadening which is due to 1) inhomogeneous disorder (Gaussian lineshape) in which a long polymer chain can have defects along the chain such as twists or kinks, resulting in conformational disorder [21-23]; 2) homogeneous disorder (Lorentzian lineshape) in which there are fluctuations in site energy due to the changes in geometry associated with the torsions within conformational sub-units [21-23].

1.5 Low Bandgap Copolymers

Low bandgap copolymers form a new class of π-conjugated polymers which promise a breakthrough in power conversion efficiency (PCE) of OPV solar cells. Two excellent candidates, PDTP-DFBT and PTB7 (shown in Figure 1.4), which show a record PCE of ~ 8% are the main focus of my PhD dissertation work. While PTB7 is commercially available, the PDTP-DFBT was solely synthesized by our collaborators at the University of California-Los Angeles. The synthetic route, chemical structure, BHJ solar cell device fabrication, and PCE measurements are described in refs. [24,25]. The backbone structure of the low bandgap copolymer is different than that of the homopolymer (PCP) in that the unit cell of the copolymer is composed of two intrachain moieties with different electron affinities, an intrinsic donor-acceptor structure (Figure 1.4). The "D-A" structure of the low bandgap (LBG) copolymer makes its optical and electrical properties distinct among the π-conjugated family such as low optical gap extending to the NIR spectral region, strong singlet fission yield, and unique charge dissociation in polymer/fullerene blends.

1.6 Theoretical Models for π-Conjugated Polymers

The electrical and optical properties of π-conjugated polymers originate from their unique quasi-1D geometry. Various theoretical models have been developed in accordance with experimental studies to provide more insights into their electro-optical properties. Starting from the simplest form of molecular orbital theory developed by Mulliken in the 1940s, the Huckel model considers only the nearest molecular sites and ignores all electron-electron interactions, electron-nuclear interactions, and nuclear-nuclear interactions. The electron-phonon interactions were added in the SSH model,

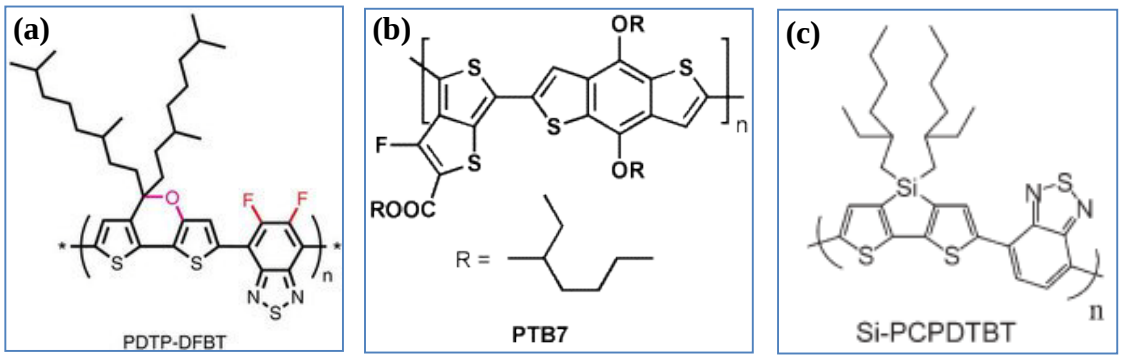

Figure 1.4: Chemical structure of three low bandgap copolymers (a) PDTP-DFBT, (b) PTB7, and (c) Si-PCPDTBT.

assuming that only one mode couples to the π-electrons. Including the electron-electron interactions leads to the Hubbard model. Finally, the PPP (Pariser-Parr-Pople) model expands the Huckel and Hubbard models to incorporate intersite interactions.

The Schrodinger equation for the spatial part of the molecular wave function Ψ(r,R) takes the form

$$H\,\Psi(r,R) = E\,\Psi(r,R) \tag{1.6}$$

where r and R are sets of electronic and nuclear coordinates, respectively, Ψ(r,R) is the molecular wave function, E is the energy eigen-value, and H is the molecular Hamiltonian given by

$$H = H_{el\text{-}el}(r) + H_{el\text{-}nuc}(r,R) + H_{nuc\text{-}nuc}(R) \tag{1.7}$$

where the electronic part includes the kinetic energy and Coulomb potential energy,

$$H_{el\text{-}el}(r) = \sum_i \frac{p_i^2}{2m_i} + \frac{1}{2}\sum_{i\neq j} \frac{e^2}{|r_i - r_j|} \quad (1.8)$$

the nuclear Hamiltonian also including the nuclear kinetic energy and potential energy contribution

$$H_{nuc\text{-}nuc}(R) = \sum_\alpha \frac{P_\alpha^2}{2M_\alpha} + \frac{1}{2}\sum_{\alpha\neq\beta} \frac{Z_\alpha Z_\beta e^2}{|R_\alpha - R_\beta|} \quad (1.9)$$

and the potential energy arising from the Coulomb interactions between the nuclei and electrons

$$H_{el\text{-}nuc}(r,R) = -\frac{1}{2}\sum_{\alpha,i} \frac{Z_\alpha e^2}{|R_\alpha - r_i|} \quad (1.10)$$

It is impossible to solve the full Hamiltonian exactly except for the case of the Hydrogen atom. Therefore, several approximations have to be made. Because the mass of a nucleus is much larger than that of an electron ($M_{nuc}/m_{el} > 10^3$), its acceleration is much smaller compared to electronic dynamics due to the electron's acceleration. Because of this, two simplifications within the Born-Oppenheimer approximation can be made: 1) the kinetic energy of the nuclear Hamiltonian can be ignored

$$H_{nuc\text{-}nuc}(R) = \frac{1}{2}\sum_{\alpha\neq\beta} \frac{Z_\alpha Z_\beta e^2}{|R_\alpha - R_\beta|} = V_{nuc\text{-}nuc}(R) \quad (1.11)$$

and 2) the electronic wave function can be separated from the nuclear component,

depending parametrically on a set of static nuclear coordinates, R.

$$\Psi(r,R) = \Psi_{aM}^{elec}(r,R)\,\Psi_{M}^{vib}(R) \tag{1.12}$$

where a denotes a particular electronic state and M is the set of vibrational quantum numbers corresponding to the electronic state a.

The molecular Hamiltonian then becomes

$$H_{BO} = H_{el\text{-}el}(r) + H_{el\text{-}nuc}(r,R) + V_{nuc\text{-}nuc}(R) \tag{1.13}$$

$$= \sum_{i,j} \tilde{t}_{ij} \left(|\psi_i\rangle\langle\psi_j| + |\psi_j\rangle\langle\psi_i|\right) + \sum_{ijkl} \tilde{V}_{ijkl}\,|\psi_i, \psi_k\rangle\langle\psi_j, \psi_l| + V_{nuc-nuc}, \tag{1.14}$$

where

$$\tilde{t}_{ij} = \int \psi_i^*(\boldsymbol{r}) \left[\frac{p^2}{2m} - \sum_\alpha \frac{Z_\alpha e^2}{|\boldsymbol{R}_\alpha - \boldsymbol{r}|}\right] \psi_j(\boldsymbol{r}) d\boldsymbol{r}^3, \tag{1.15}$$

is a one-electron transfer integral and

$$\tilde{V}_{ijkl} = \int \psi_i^*(\boldsymbol{r})\,\psi_k^*(\boldsymbol{r}') \frac{e^2}{|\boldsymbol{r} - \boldsymbol{r}'|}\,\psi_j(\boldsymbol{r})\,\psi_l(\boldsymbol{r}') d\boldsymbol{r}^3 d\boldsymbol{r}'^3, \tag{1.16}$$

is a two-electron integral representing the electron-electron interactions.

Further simplifications can be made by considering only the more mobile π-electrons. The σ-electrons do not participate in optical and electrical operations of

conjugated polymers because the σ to σ* transition requires much higher energy than the π to π* transition. Thus they only play a role of screening the Coulomb interactions between the π-electrons and nucleus, usually modeled as a static dielectric function and embedded in the effective interaction between nuclei and π-electrons, V_p, and the effective electron-electron interactions, $V_{el-el}^{eff}(r-r')$.

$$\tilde{t}_{ij} = \int \psi_i^*(\boldsymbol{r}) \left[\frac{p^2}{2m} + V_p(r,R)\right] \psi_j(\boldsymbol{r}) d\boldsymbol{r}^3 \tag{1.17}$$

$$\tilde{V}_{ijkl} = \iint \psi_i^*(\boldsymbol{r}) \psi_k^*(\boldsymbol{r}') V_{el-el}^{eff}(r-r') \psi_j(\boldsymbol{r}) \psi_l(\boldsymbol{r}') d\boldsymbol{r}^3 d\boldsymbol{r}'^3, \tag{1.18}$$

The integral in equation (1.18) is dominated by the diagonal terms which is the interaction between electrons in the same orbital

$$U_i = \tilde{V}_{iiii} = \iint \psi_i^*(\boldsymbol{r}) \psi_i^*(\boldsymbol{r}') V_{el-el}^{eff}(r-r') \psi_i(\boldsymbol{r}) \psi_i(\boldsymbol{r}') d\boldsymbol{r}^3 d\boldsymbol{r}'^3, \tag{1.19}$$

and the interaction between electrons in orbitals ψ_i and ψ_j.

$$V_{ij} = \tilde{V}_{iijj} = \iint \psi_i^*(\boldsymbol{r}) \psi_i^*(\boldsymbol{r}') V_{el-el}^{eff}(r-r') \psi_j(\boldsymbol{r}) \psi_j(\boldsymbol{r}') d\boldsymbol{r}^3 d\boldsymbol{r}'^3, \tag{1.20}$$

More simplifications can be made by including only nearest neighbor interactions with $\epsilon = \tilde{t}_{ii}$ and $t = \tilde{t}_{i,i+1}$

The Born-Oppenheimer (BO) Hamiltonian in the simplest form is

$$H_{BO}=\sum_i \epsilon \quad (|\psi_i\rangle\langle\psi_i| + \sum_i t\,(|\psi_i\rangle\langle\psi_{i+1}| + |\psi_{i+1}\rangle\langle\psi_i|) \; + \sum_i U_i\,|\psi_i\rangle\langle\psi_i| + \sum_{i\neq j} V_{ij}\,|\psi_i,\psi_j\rangle\langle\psi_i,\psi_j| + \quad V_{nuc-nuc}, \tag{1.21}$$

1.6.1 The Huckel Model

Considering a periodic linear chain of N identical sites (each site is a carbon atom with the $2p_z$ electron wave function in the simple case of polyacetylene, for instance), the BO Hamiltonian that describes this system in the Huckel model which assumes $U=V=V_p = V_{nuc\text{-}nuc}=0$ has the following form

$$H_{BO} = \sum_i \epsilon \quad (|\psi_i\rangle\langle\psi_i| + \sum_i t\,(|\psi_i\rangle\langle\psi_{i+1}| + |\psi_{i+1}\rangle\langle\psi_i|) \tag{1.22}$$

where ε is the energy of a single site and t is the interaction energy between two neighboring sites.

$$\varepsilon = \int \psi_i^*(\boldsymbol{r})\left[\frac{p^2}{2m} + V_p(r,R)\right]\psi_i(\boldsymbol{r})d\boldsymbol{r}^3\,, \tag{1.23}$$

$$t = \int \psi_i^*(\boldsymbol{r})\left[\frac{p^2}{2m} + V_p(r,R)\right]\psi_{i+1}(\boldsymbol{r})d\boldsymbol{r}^3 \tag{1.24}$$

The wave function of this system is a linear combination of $2p_z$ wave function of each carbon atom which takes the Bloch form

$$\psi_k(x) = \sum_n e^{ikna}\,\phi(x-na) \tag{1.25}$$

where a is the lattice constant and ϕ(x-na) represents a carbon $2p_z$ orbital on the n-th site.

The eigenvalues of this Hamiltonian are given by [26]:

$$E(k) = \epsilon \pm 2tcos(ka) \tag{1.26}$$

The lower energy π band corresponds to the dispersion relation:

$$E(k) = \epsilon - 2tcos(ka) \tag{1.27}$$

where $k = \frac{n\pi}{Na}$ with n is an integer taking values between $-N \leq n \leq N$

Filling the states with π electrons, one for each carbon atom, the π-band is half filled and thus the Fermi level is located at k=π/2a, as shown in Figure 1.5a. Under these approximation the material based on this structure, such as an individual chain of neutral polyacetylene would be a metal. However, experimental studies have shown that neutral polyacetylene is a semiconductor. This discrepancy can be resolved by the Peierls theorem. It states that a 1D metal is unstable with respect to a lattice distortion which opens an energy gap at the Fermi level [27]. The Peierls distortion results in the bond alternation of double (shorter) and single (longer) bonds, doubling the unit cell size from a to 2a to include two atoms and therefore lowering the energy of the system. This process is called dimerization. The energy spectrum for a linear dimerized chain becomes

$$E(k) = \epsilon \pm \sqrt{t_s^2 + t_d^2 + 2t_s t_d \cos{(2ka)}} \tag{1.28}$$

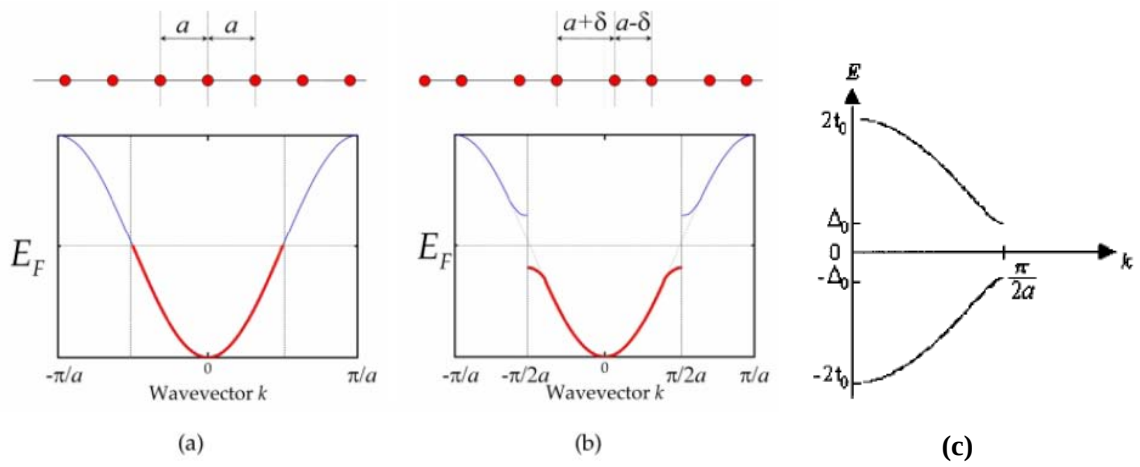

Figure 1.5: Energy band structure of (a) undimerized and (b) dimerized linear chains of conjugated polymers. (c) polyacetylene: the energy gap opens at k=π/2a as a result of the Peierls distortion (adapted from ref. [31]).

where t_s and t_d are the single-bond and double-bond transfer integrals. We can rearrange t_s and t_d to have the form of $t_s = t\ (1+ \delta)$ and $t_d = t\ (1- \delta)$, where δ is the distortion parameter [18]. Then the energy dispersion relation takes the form

$$E(k) = \epsilon \pm 2t\sqrt{\sin^2(2\mathrm{ka}) + \delta^2 \cos^2(2\mathrm{ka})} \qquad (1.29)$$

At the new zone boundary edge k=π/2a, the energy is E = ε ± 2δt, opening a bandgap of 2Δ =4δt (see Figure 1.5b).

The resulting band structure is shown in Figure 1.5c. Since the lower band (the valance band in semiconductor terminology) is fully occupied and the upper band (the conduction band) is empty, then a linear chain of π conjugated polymers is therefore a semiconductor.

1.6.2 SSH Model

In the SSH model, Su, Schrieffer and Heeger introduced electron-phonon interactions to the Huckel model for understanding more clearly the role of vibrations in the dimerization process. The SSH description of the electronic structure was proposed based on the simple molecular structure of polyacetylene, repeated -CH- units (Figures 1.6a and 1.6b) [28]. The construction of the SSH Hamiltonian was based on two assumptions: 1) The π-electronic structure can be treated in the tight-binding approximation, and 2) the electron-phonon interaction couples the electronic states to the molecular geometry so that the bond length-dependent transfer integral can be linearly corrected up to the first order Taylor expansion about the undimerized configuration as

$$t_{n,n+1} = t_0 + \alpha(u_{n+1}-u_n) \tag{1.30}$$

where $t_{n,n+1}$ is the bond length-dependent transfer integral from site n to n+1, t_0 is the first order transfer integral of the undimerized chain, α is the electron-phonon coupling constant, and u_n is the displacement of the n-th carbon atom from equilibrium.

The resulting SSH Hamiltonian is the sum of three terms [28]

$$H_{SSH}=H_{el\text{-}el}+H_{nuc\text{-}nuc}+H_{el\text{-}nuc} \tag{1.31}$$

where

$$H_{el-el} = -t_0 \sum_n (c_{n+1}^{\dagger} c_n + c_n^{\dagger} c_{n+1}) \tag{1.32}$$

representing the hopping of π-electrons to the nearest neighboring sites in which $c_n^\dagger$ and c_n are electron creation and annihilation operators;

$$H_{nuc-nuc} = \sum_n \frac{p_n^2}{2M} + \frac{1}{2}K_n(u_{n+1} - u_n)^2 \tag{1.33}$$

is the sum of the kinetic energy of all carbon atoms with mass M and the potential energy which results from their displacements from the uniform σ bond length; and

$$H_{el-nuc} = \alpha\sum_n(u_{n+1} - u_n)(c_{n+1}^\dagger c_n + c_n^\dagger c_{n+1}) \tag{1.34}$$

is the electron-phonon coupling term which arises from the σ bond length alternation.

The bond alternation in the ground state may be approximated as $\langle u_n \rangle = (-1)^n u_0$ where u_0 is the displacement position which minimizes the energy of the system. One can see that both u_0 and $-u_0$ minimize the energy for trans-polyacetylene because of the bond symmetry along the chain axis. Thus the ground state energy of trans-polyacetylene has a double minimum at $\pm u_0$, as shown in Figure 1.6d, which corresponds to two degenerate ground state structures as seen in Figure 1.6c. If the two degeneracies co-exist in one polyacetylene chain, then at the boundary between the two 'phases', there is a defect, known as soliton with associated mid-gap electronic states.

1.6.3 Hubbard and PPP Models

The Hubbard and PPP (Pariser-Parr-Pople) models take into account electron-electron interactions. While the Hubbard model assumes that the most important interaction

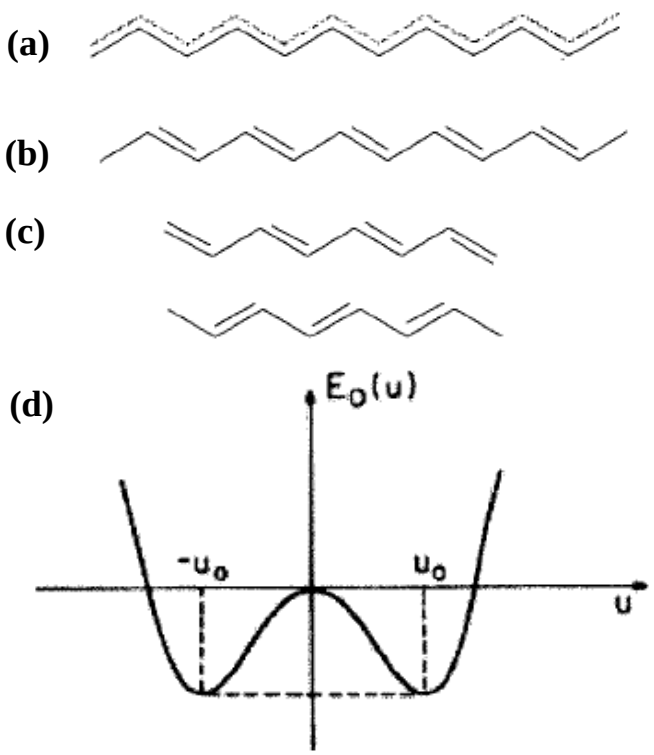

Figure 1.6: Polyacetylene (a) undimerized structure; (b) dimerized structure due to the Peierls instability; (c) degenerate A and B phases in trans-polyacetylene; (d) total energy of the dimerized polyacetylene chain with the double minimum associated with the spontaneous symmetry breaking and two-fold degenerate ground state. (Adapted from ref. [31]).

occurs between two electrons on the same site, the PPP model extends it to account for the intersite contribution. The on-site Hubbard Hamiltonian is

$$H_{Hub} = U \sum_i c_{i,\uparrow}^{\dagger} c_{i,\uparrow} c_{i,\downarrow}^{\dagger} c_{i,\downarrow} \tag{1.35}$$

where $\uparrow \; and \; \downarrow$ specify electrons with spin up and spin down, respectively, and

$$U = \langle \phi(1)\phi(2) | V_{el-el}^{eff} | \phi(1)\phi(2) \rangle \tag{1.36}$$

where U can be interpreted as the repulsion energy between two electrons on the same orbital.

The PPP model generalizes the Hubbard model to account for most electronic correlations. Its Hamiltonian includes an intersite contribution given by

$$V = \frac{1}{2}\sum_{ij} V_{ij}\left(c_i^{\dagger}c_i - 1\right)\left(c_j^{\dagger}c_j - 1\right) \tag{1.37}$$

where $V_{ij}$is the electron-electron interaction between sites i and j

$$V_{ij} = \langle \phi_i(1)\phi_j(2)|V_{el-el}^{eff}|\phi_i(1)\phi_j(2)\rangle \tag{1.38}$$

The PPP model has been used to analyze excitons in conjugated polymers both in weak and strong coupling limits [29,30].

1.7 Major Photoexcitations in π-Conjugated LBG Copolymers

The optically excited states, or photoexcitations, which determine the electrical and optical properties of conjugated polymers are electrically classified into two categories; these are charged and neutral photoexcitations. Here, I present the most critical photoexcitations which lay a foundation for understanding the charge photogeneration process in OPV devices and several spin-related physical phenomena in the field of magnetic field effect. These are polarons and polaron pairs (charged photoexcitations), and singlet, triplet excitons, and triplet pairs (neutral photoexcitations).

1.7.1 Charge Photoexcitations

1.7.1.1 Polarons and Polaron Pairs

By definition, the quasi-particle polaron is the combination of a charge carrier, either an electron or a hole, with its associated strain field [32]. In disordered organic materials, the polaronic effect originates from the local lattice deformation that occurs upon putting a charge carrier on a certain molecular site. When taking an electron away from the HOMO or adding it into the LUMO of a molecule, the electron-lattice interaction relaxes the molecular orbitals and the nuclei to a new position of minimum energy, creating states within the energy gap (between HOMO and LUMO) where polarons are populated. The “mid-gap” states, as shown in Figure 1.7, are symmetrically located about the center of energy gap and alternate in parity with respect to the HOMO level which is gerade. Unlike in crystalline inorganic materials where the lattice structure is rigid leading to a small polaronic effect and highly mobile charge carriers [32], in the organic counterpart, charge carrier polarons are more localized and their mobility is much lower than that of the inorganic counterpart [33].

Polarons can be positive (P^+) or negative (P^-) charges with spin ½. They can be created by chemically doping [34] with strong electron acceptor materials or optically by photon absorption; or by electrically injecting electrons and holes into organic layers in OLEDs [35]. They can be detected optically by observing their absorption signature transitions, P_1 and P_2 (Figure 1.7), using the photoinduced absorption technique (see experimental section); or magnetically by measuring the magnetic field response on conductivity, MC [36].

A polaron pair PP is loosely bound, subjected to Coulombical attraction of two

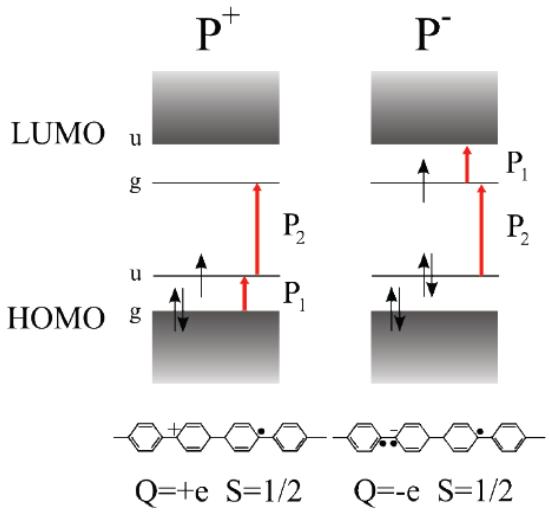

Figure 1.7: Band diagrams showing the mid-gap state occupations associated with polarons and the allowed optical transitions related to them; u and g represents the parity of the states. In the structural schematics, black dots represents spin while + and – signs indicate charge**.**

oppositely charged polarons, P^+ and P^-, on adjacent chains [37] . Like the exciton (discussed in the next section), the PP can be formed in spin singlet (spin 0) or triplet (spin 1) configuration depending on the spin alignment of two composites P^+ and P^-. The energy difference between the singlet and triplet PPs is small, within the order of the hyperfine coupling constant, given that their binding energy is mainly Coulombic and because of their large spatial extent [38]. PPs can recombine into singlet or triplet excitons depending on their initial spin state. In OLEDs, due to the spin statistic, the recombination ratio between singlet and triplet is 1:3.

1.7.2 Neutral Photoexcitations

1.7.2.1 Singlet and Triplet Excitons

An exciton is a Coulombically bound state of electron-hole pairs that can move together and remain associated as a quasi-particle. Taking electron-electron interactions into account, excitons in conjugated polymers can be modeled successfully by the Hubbard and PPP models. Excitons can be generated by photon absorption, exciting electrons from the HOMO to the LUMO, or by capture of PPs. The exciton binding energy is lower than the HOMO-LUMO difference partly due to the attractive Coulomb interaction and the structural relaxation. Depending on the strength of the Coulomb interaction between electrons and holes, excitons can be generally described as a Wannier-Mott or Frenkel type. The Wannier-Mott exciton is often found in inorganic crystalline semiconductors where they are weakly bound with a small binding energy on the order of E_b~50meV and therefore delocalized over many atoms or molecules because of a large dielectric constant. On the other hand, the Frenkel exciton is a molecular exciton that is localized to a single molecule or atom, although it can hop from one molecule to another by virtue of coupling between neighboring monomers. The binding energy of Frenkel excitons is on the order of E_b~1eV.

The excitons in conjugated polymers often fall into the intermediate regime between the Frenkel and Wannier-Mott types in which they can be spatially extended along sections of polymer backbone (intrachain excitons) or stretch across different chains or folded sections of the same chains (interchain excitons). Their binding energy has been reported experimentally in a wide range from 0.1eV [39] to 1eV [40,41].

The initial photoexciton in conjugated polymers should be in the singlet configuration

S=0, namely a singlet exciton which is considered to be the primary photoexcitation in these compounds. The singlet exciton might convert at a later time to the spin triplet manifold having total spin S=1, namely a triplet exciton. This occurs via intersystem-crossing due to the spin-orbital coupling, or by the recently investigated phenomenon of 'singlet fission' in which one singlet exciton dissociates into two separated triplets via the coherent triplet-pair state (discussed in the next section). The overall wavefunction of two fermions, singlet and triplet excitons, must be antisymmetric in spin and electronic coordinates as follows:

$$\psi^{singlet} = \frac{1}{2}(\psi_1(1)\psi_2(2) + \psi_2(1)\psi_1(2))(\uparrow(1)\downarrow(2) - \uparrow(2)\downarrow(1)) \quad (1.39)$$

$$\psi^{triplet} = \frac{1}{2}\big(\psi_1(1)\psi_2(2) - \psi_2(1)\psi_1(2)\big)(\uparrow(1)\downarrow(2) + \uparrow(2)\downarrow(1)) \quad (1.40)$$

$$\psi^{triplet} = \frac{1}{2}(\psi_1(1)\psi_2(2) - \psi_2(1)\psi_1(2))(\uparrow(1)\uparrow(2)) \quad (1.41)$$

$$\psi^{triplet} = \frac{1}{2}(\psi_1(1)\psi_2(2) - \psi_2(1)\psi_1(2))(\downarrow(1)\downarrow(2)) \quad (1.42)$$

where ψ_i is the electronic part of the wavefunction and ↑ and ↓ are the spin up and spin down projection of the spin part.

The singlet and triplet energy levels are degenerate in the noninteraction case. Taking electron-electron interactions into account splits the energy levels between the lowest singlet 1^1B_u and triplet 1^3B_u states with the triplet taking the lower energy. The lower energy triplet is due to the antisymmetric nature of the spatial part of the triplet wavefunction, resulting in electrons that are more tightly bound to nuclei and thus a lower energy. The splitting energy between 1^1B_u and 1^3B_u state is sensitive to the

exchange interactions that scale with the electron and hole wavefunction overlap. Experimental results showed that the triplet 1^3B_u state is 0.7±0.1eV below the singlet 1^1B_u state in most conjugated polymers [16].

Figure 1.8 shows the picture of exciton bands with various possible optical transitions in singlet and triplet manifold. To conclude, we list several possible decay paths of singlet excitons; these are :1) recombine radiatively via fluoresce emission for singlet and phosphoresce emission for triplet; 2) recombine nonradiatively by emitting phonons; 3) experience intersystem crossing to a triplet via spin orbital coupling; 4) fission into two coherent triplets; 5) dissociate into polaron pairs at the donor-acceptor interface.

1.7.2.2 Singlet Fission and Triplet Pairs

A triplet pair (TT) is a pair of two correlated triplet excitons which are formed via the singlet fission (SF) process. Singlet fission has been identified in several organic compounds such as crystalline tetracene [42], crystalline pentacene [43,44], 1,3-diphenylisobenzofuran (DPIBF) [45], zeaxanthin [46], and more recently also in low bandgap copolymers [47]. Singlet fission is a spin allowed process in which a singlet exciton dissociates into two separated triplets via the intermediate TT state. The intermediate TT state is initially an overall singlet S=0 ^{1}(TT) state. However, the TT state might also be in spin triplet, S=1 ^{3}(TT) or quintet S=2, ^{5}(TT) configuration, resulting from the dipole coupling of two triplets. If the interaction between the two adjacent chromophores is weaker than the coupling of two triplets, then the singlet ^{1}(TT) state is almost degenerate with the triplet ^{3}(TT) and quintet ^{5}(TT) states. In this case magnetic field effects can be observed based on the SF process. If the interaction is strong enough

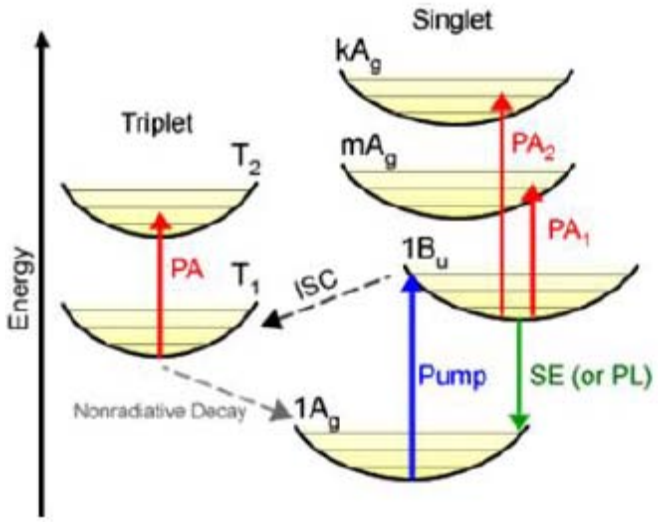

Figure 1.8: Neutral photoexcitations in conjugated polymers with nondegenerate ground states. Various optical transitions associated with the absorption and fluorescence in singlet and triplet manifolds. Formation of triplet exciton through intersystem crossing (ISC) (broken line arrow).

to lift the degeneracy of the ^{1}(TT), ^{3}(TT), and ^{5}(TT) states beyond the dipole coupling, a pure singlet ^{1}(TT) state is generated in the SF event. While the former ^{1}(TT) state can efficiently separate into two free triplet excitons, resulting from the gradual loss of its spin coherence, in the latter case of a pure singlet ^{1}(TT), two triplets might not be generated on the equivalent timescale [48].

The SF reaction can occur in sub-picosecond timescale. This process can be isoenergetic, $E(S_1) = 2E(T_1)$; exoenergetic, $E(S_1) > 2E(T_1)$; or even endoenergetic, $E(S_1) < 2E(T_1)$. Of the three, the isoenergetic or resonant SF is the most efficient route and this is the case in the low bandgap copolymers that we studied (see Chapter 3). When SF is endoenergetic, then the process depends on temperature and excitation energy. In crystalline tetracene, SF was first believed to be endothermic and absent at temperatures below 160K [49-51], but later results showed that this is not true [42]. High energy

photons can also be used to put singlet excitons into higher energy sates or vibrational levels; in this case, SF has to compete with the ultrafast internal conversion and vibrational relaxation and is far less efficient but is nevertheless still possible.

Finally, SF can be a one-step mechanism [42,52,53], which proceeds directly from the singlet exciton state to the ^{1}(TT) without going through an intermediate charge transfer CT state, or a two-step process [52,54,55], in which the initial singlet exciton is first transformed into a CT state by electron transfer and then to ^{1}(TT) by a back electron transfer (Figure 1.9b). SF can be intrachain (intramolecular) [56], resulting in two separated triplets on the same chain; or interchain (intermolecular), in which two triplets are coherently formed on two adjacent chains (or molecules) from one singlet exciton.

1.8 Organic Photovoltaic

The photovoltaic effect observed in organic materials dates back to the 1950s with devices fabricated from a single layer of organic materials sandwiched between two metallic electrodes [57,58]. The organic layer absorbs light to generate excitons which are then split into electrons and holes by an internal electric field built up from the difference in work function of two electrodes. The internal field subsequently attracts electrons to the positive electrode and holes to the negative electrode. The single cell OPV has very low power conversion efficiency (PCE) (<0.1%) because of the extremely low efficiency of the exciton ionization process, given the large exciton binding energy of ~1eV, insufficient built-in electric field, and the short exciton lifetime (~ps).

The second generation, bilayer OPV was first implemented by Tang in 1986 [59]. In

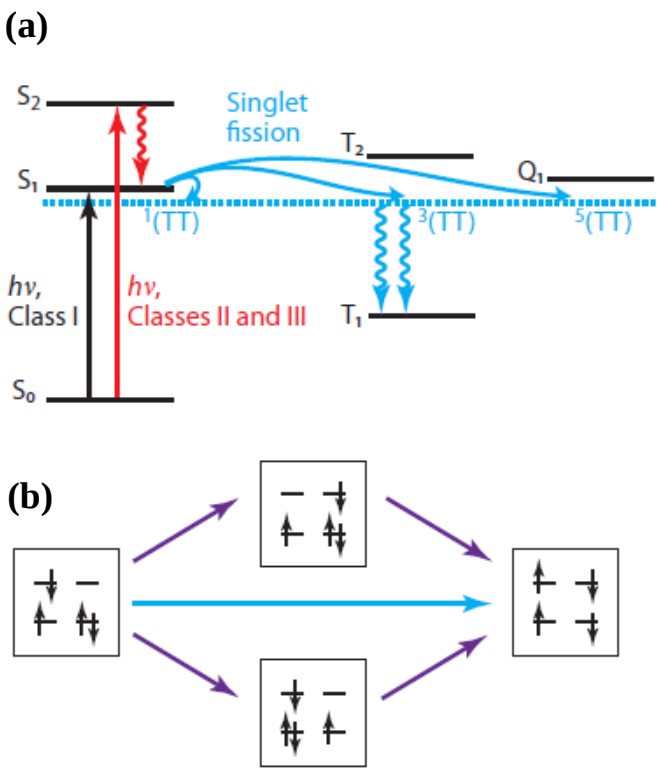

Figure 1.9: The singlet fission process (a) An expanded Jablonski diagram depicting singlet fission from the lowest excited state S_1 of singlet exciton following ground state excitation; an initially formed triplet pair ^{1}(TT) dissociates into two independent triplets. (b) One-step (blue) and two-steps (purple) mechanism in singlet fission (adapted from ref. [54]).

his patent filed in 1979, a bi-layer PV device consisting of copper PC (acting as electron donor and hole transporter) and perylene derivative (acting as electron acceptor and transporter) achieved a PCE of 1%. The exciton is first created in the donor and then diffuses to the D-A interface where it can dissociate into a “free” electron and hole that are transported to the metal electrodes. The exciton dissociation at the heterojunction interface was aided by the local field originating from the lower acceptor’s LUMO level compared to that of the donor. Since the diffusion length of excitons in PCPs are ~10 nm [60,61], only a small fraction of excitons generated in the typical ~100nm film thickness

reach the interface and dissociate, leading to loss of absorbed photons and consequently, also the OPV cell efficiency is low. This problem can be overcome using the bulk heterojunction (BHJ) cells based on blends of donors and acceptors.

The third generation BHJ cells were reported independently by Yu et al. [62] and Halls et al. [63] in 1995. In this cell (see Figure 1.10), the blend of donor and acceptor materials formed an interpenetrating network of a microphase-separated blend with typical domain size of ~ 10nm, which is within the exciton diffusion length, leading to much higher quantum efficiency of charge separation. Today, 8% PCE of BHJ OPV cells was realized with the π-conjugated low bandgap (LBG) copolymers (PDTP-DFBT and PTB7 in blend with the C_{71}-PCBM fullerene) which are the main subject matter of this dissertation work [24,25]. In these OPV devices, the charge dissociation dominantly originates from a new TT state which forms through the singlet fission process (see Chapters 3 and 4).

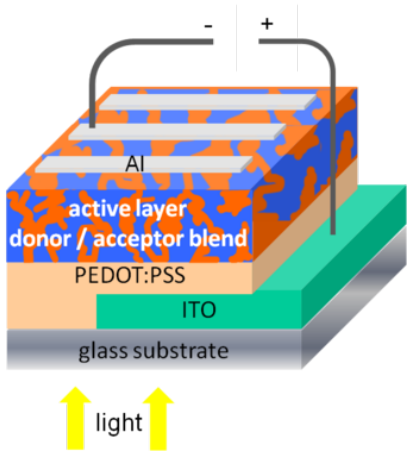

Figure 1.10: Typical device structure of bulk hetero-junction solar cell with ITO and aluminum are two electrodes. PEDOT:PSS acting as a buffer layer for hole transport (adapted from http://www.uni-oldenburg.de/en/physics/research/ehf/ohpv/research/).

1.9 Magnetic Field Effect

The magnetic field effect in organic semiconductor (OSEC) devices, such as magneto conductance (MC) and magneto electroluminescence (MEL) in organic light emitting diodes (OLED), and magneto-photoconductivity (MPC) in organic photovoltaic (OPV) solar cells, has been intensively studied in recent years. Various models have been proposed for explaining the magnetic field response including the field response of carrier mobility and carrier density [38,64-76]. Recently, magneto-photoinduced absorption (MPA) and magneto-photoluminescence (MPL) have also been applied to OSEC thin films; it has been realized that these effects are related to the photoexcitation spin density that is modulated by the applied field [77,78]. This finding has unified the explanations for the organic magnetic field effect in both devices and thin films. A number of mechanisms that have been advanced for explaining the spin-mixing that figures in MPA(B) response include: (i) the hyperfine interaction (HFI) that mixes singlet and triplet polaron pairs; (ii) the zero-field splitting interaction for spin triplets; (iii) the difference in *g*-factor of the photogenerated electron and hole polarons in polymer/fullerene blend used as the active layer in OPV cells. In contrast, the MPL originates indirectly through the collision of singlet and triplet excitons which causes an increase of nonradiative decay channel and consequently decreases the luminescence emission.

So far the magnetic field effect has been applied at steady state conditions, in which the spins of the long-lived excitations approach equilibrium. Since the discovery of singlet fission in some π-conjugated polymers, we have searched for a new experimental technique for studying this ultrafast, spin-dependent physical phenomenon in which the

spin photoexcitations are not in thermal equilibrium. With our long-accumulated experience in the field of magnetic field effect and transient dynamics, coupled with the unique capability to probe the dynamics of photoexcitations in the time domain from picoseconds to milliseconds in the spectral range from mid-IR to UV/VIS, the time-resolved magnetic field effect, dubbed transient magneto-photoinduced absorption (t-MPA), has emerged as the most suitable experimental technique. The t-MPA technique will be discussed in more detail in Chapter 2, Experimental Setup.

The t-MPA has been used to study the singlet fission process in low bandgap copolymers that can occur in sub-picoseconds time scale and form an intermediate TT state. The intermediate TT state, which might dissociate into two separated triplets at a later time, or recombine to the ground state, appears instantaneously with the singlet exciton within our experimental time resolution of 300fs. The observed t-MPA(B) response on the TT pair in the ps time domain can be generally explained as follows: In the absence of a magnetic field, three of nine TT states have a singlet character. The magnetic field, B can redistribute the singlet character among the nine states, leading to changes in the initially populated levels by the fission process (see Appendix). As time progresses, the total population of the SF-born TT pair becomes magnetic field-dependent through the spin-dependent decay rate of each level.

CHAPTER 2

EXPERIMENTAL SETUP

2.1 Overview of Optical Processes

2.1.1 Linear Absorption

When light passes through materials, it can be transmitted, absorbed, reflected, and scattered. Thus the intensity of incident light on materials is a total sum of

$$I_0=I_t+I_a+I_r+I_s \; . \tag{2.1}$$

Experimentally, we can measure the transmission and use it to calculate the amount of light that has been absorbed. Assuming that no light is scattered, and that the incident light is not strong enough for nonlinear effects to occur, and that there is no emission in the direction of detection, the transmitted light is described by the Beer-Lambert law as

$$I_t = I_0 \, (1-R) \, e^{-\alpha d} \tag{2.2}$$

where $R = (I_r/I_0)$ is the reflection coefficient, α is the absorption coefficient, and d is the sample thickness.

The absorption coefficient is defined as

$$\alpha(\omega) = N\,\sigma(\omega), \tag{2.3}$$

where N is the optical density of absorbers and $\sigma(\omega)$ is the optical cross-section, which is frequency-dependent.

The measurable quantity defining absorbance, A, measured through the transmittance loss through a sample at a given wavelength is defined by

$$A = -\ln(T) = -\ln\left(\frac{I_t}{I_0}\right) \tag{2.4}$$

Equations (2.2) and (2.4) can be used to obtain A as

$$A = \alpha d - \ln(1-R) \tag{2.5}$$

If the reflection R is small, then $A = \alpha d$, which is defined as the optical density (OD).

2.1.2 Photoinduced Absorption

Photoinduced absorption (PA) is the change in the absorption of materials under illumination. A light source that is called the 'pump' beam is used to excite the material, populating the excited states with neutral and charged photoexcitations. Then a second light source called a 'probe' beam is designed to monitor the absorption of the photoexcitations. This would be done by measuring the transmission of the probe beam with (T_L) and without (T_D) the pump beam. Using modulation spectroscopies, the PA is obtained by modulating the pump beam with a mechanical chopper or an acousto-optic

modulator at a specific frequency, *f* that is also used as the reference source for a lock-in amplifier (see section 2.4.2). If the change in reflectivity is small, then the PA is obtained as follows:

$$PA = - \Delta T/T_D = - (T_L-T_D) / T_D \quad (2.6)$$

$$T_L = T_D\, e^{-\Delta\alpha d} \quad (2.7)$$

$$\frac{T_D+\Delta T}{T_D} = 1 + \frac{\Delta T}{T_D} = e^{-\Delta\alpha d} \quad (2.8)$$

$$\Delta\alpha d = -\ln\,(1 + \frac{\Delta T}{T_D}) \quad (2.9)$$

When $\Delta T << T_D$, we then can write

$$\Delta\alpha d \approx -\frac{\Delta T}{T_D} = PA \quad (2.10)$$

2.1.3 Recombination Kinetic Analysis

In photomodulation spectroscopies, the PA signal is proportional to the photoexcitations density, N(t) as follows

$$-\frac{\Delta T}{T} = \Delta\alpha d = N\sigma d \quad (2.11)$$

The photoexcitation dynamics in the time-domain is described by a single rate equation for the photoexcitation density

$$\frac{dN}{dt} = G(t) - R(N) \tag{2.12}$$

where G(t) is the photoexcitation generation rate that is proportional to the pump intensity I_L, $G(t) = aI_L$, and R(N) is the recombination rate.

Under steady state conditions, e.g. in CW measurements at small *f*, the photoexcitations density is constant with time, leading to:

$$\frac{dN}{dt}|_{ss} = 0 \text{ and } G = R \, . \tag{2.13}$$

In transient spectroscopy, N=N(t) and N(0) is the photoexcitation density following complete absorption of the pump pulse.

The photoexcitations kinetics depends on various generation and recombination conditions. The recombination process may be monomolecular, where only a single excited species is involved, bimolecular which involves two excited species, or dispersive kinetics in which there is a distribution of photoexcitation lifetimes. Each recombination process carries its own signature in the steady state as well as in the transient excitation conditions.

2.1.3.1 Monomolecular Recombination

The monomolecular recombination rate is

$$R = \frac{N}{\tau}. \tag{2.14}$$

Under transient excitation condition: G = 0 then equation (2.12) becomes

$$\frac{dN}{dt} = -\frac{N}{\tau} \tag{2.15}$$

which has the solution

$$N(t) = N(0)e^{-t/\tau} \tag{2.16}$$

Thus *a single exponential decay is the signature of the monomolecular process.*

Under steady state excitation condition: $\frac{dN}{dt}|_{ss} = 0$. Equation (2.12) becomes

$$G - \frac{N_{ss}}{\tau} = 0 \tag{2.17}$$

with the solution

$$N_{ss} = G\tau = aI_L\tau \tag{2.18}$$

Therefore, *a linear dependence of the PA signal on pump laser intensity signifies the molecular recombination in CW spectroscopy*.

2.1.3.2 Bimolecular Recombination Dynamics

The bimolecular recombination rate has the form of

$$R = bN^2 \tag{2.19}$$

Under transient condition, equation (2.12) becomes

$$\frac{dN}{dt} = -bN^2 \tag{2.20}$$

with the solution of

$$N(t) = \frac{N(0)}{1+bN(0)t} \tag{2.21}$$

In the steady state, equation (2.12) and its solution are

$$G - bN_{ss}^2 = 0 \tag{2.22}$$

$$N_{ss} = \sqrt{G/b} = \sqrt{aI_L/b} \tag{2.23}$$

The ½ power law dependence of the PA signal on the laser intensity shows the bimolecular process in CW spectroscopy.

2.1.3.3 Dispersive Recombination Dynamics

In disordered materials such as polymers, there is a distribution of recombination times. Thus the photoexcitation density, N(t), generally has the form

$$N(t) = \int_0^\infty e^{-t/\tau} G(\tau) d\tau \tag{2.24}$$

where $G(\tau)$ is the distribution function of lifetimes. We summarize here several cases.

***Case 1**:* A bi-exponential decay in which the distribution function is

$$G(\tau) = N_1\delta(t-\tau_1) + N_2\delta(t-\tau_2) \tag{2.25}$$

Then

$$N(t) = N_1 e^{-t/\tau_1} + N_2 e^{-t/\tau_2} \tag{2.26}$$

***Case 2**:* A power law decay occurs when

$$G(\tau) = \left(\frac{\tau}{\tau_1}\right)^{-(1+\alpha)} \tag{2.27}$$

with $\alpha < 1$. Equation (2.24) then becomes

$$N(t) \propto (\frac{t}{\tau_1})^{-\alpha} \tag{2.28}$$

***Case 3**:* A stretched exponential decay arises when the distribution function is:

$$G(\tau) = e^{-(\tau/\tau_0)^{\upsilon}} \tag{2.29}$$

The solution for N(t) is

$$N(t) \propto e^{-(\upsilon+1)(\frac{t}{\upsilon\tau_0})^{\beta}} \tag{2.30}$$

with $= \frac{\upsilon}{\upsilon+1}$.

2.1.4 The Analysis for the Background in the Ultrafast Pump/Probe Technique

When using pulses at 80 MHz repetition rate in the ps pump-probe experiment from a Ti-Sapphire laser as pump excitation (having 80 MHz rep. rate), the time elapsed between successive pump pulses is ~12.5 ns. In this case, some of the long-lived photoexcitations generated from one pulse do not completely recombine until the arrival of the next pulse, and thus contribute to a background PA signal [79,80]. In fact, the transient PA rides on top of a 'background PA' as seen in Figure 2.1. The accumulation of the background photoexcitations from many pulses generates a steady state 'background PA'. This 'background PA' is in fact modulated at frequency, *f*= 50 kHz, which is the pump modulation frequency in the ps setup and thus can serve as a convenient way for measuring the ss-PA at fast modulation frequency.

We measured the 'background PA' in the present study of pristine PDTP-DFBT (isolated chains) at *f*=1 kHz. The pump in this case was the Ti-Sapphire laser beam, and the probe originates from the OPO 'signal' and 'idler' beams. This probe beam is much stronger than the probe beam from an incandescent light source, especially in the mid-IR spectral range. The combination of strong probe beam and fast modulation frequency (away from 1/*f* noise) is ideal for measuring weak ss-PA that originates from photoexcitations that decay in the μsec time domain. As a matter of fact, the 'background PA' in the pump-probe experiment is the only way of measuring weak ss-PA in the mid-IR, and we used it here for measuring the triplet PA spectrum at room temperature, since

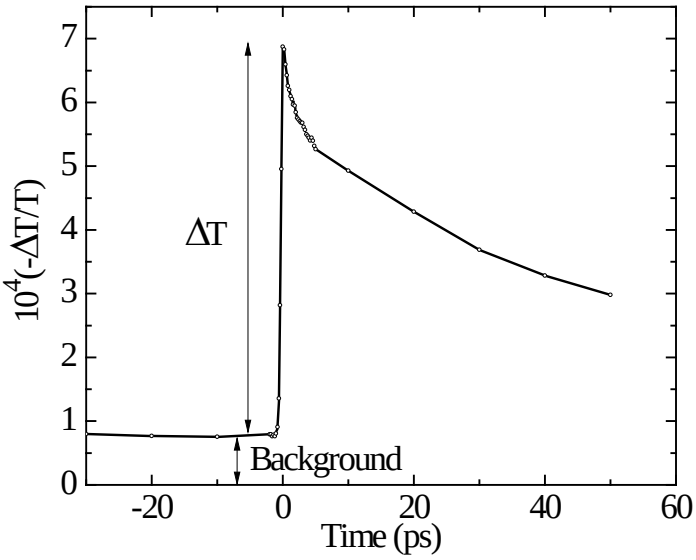

Figure 2.1: An example of the ps pump-probe measurement in the mid-IR spectral range of pristine PDTP-DFBT film using the pulsed laser setup having 80 MHz repetition rate that shows the transient PA response at $t>0$ and the background PA for $t<0$. The background PA results from the accumulation of many pulses; it originates from the long-lived photoexcitations, of which lifetime is longer that the time interval between successive pulses (or 12.5 ns).

the triplet density at room temperature is quite small, due to their relatively short lifetime.

2.2 Transient Pump-Probe Spectroscopies

2.2.1 Femtoseconds MIR OPO System

The femtoseconds OPO system, bought from Spectra Physics, is composed of a series of commercial lasers to pump an optical parametric oscillator (OPO), which uses a lithium triborate (LBO) nonlinear crystal to generate new infrared wavelength frequencies. A pair of 980 nm laser diodes was used to pump a solid state laser (Millennia Prime) to generate a 10 Watts, 532 nm laser beam. The Millennia then pumps

the Tsunami, a 150fs titanium-sapphire pulsed laser with the repetition rate of 80 MHz, which in turns pumps the OPO system.

2.2.1.1 Experimental Methods

The transient picoseconds experimental setup is depicted in Figure 2.2; it is a version of the well-known pump-probe correlation spectroscopy. The pump excitation beam was composed of pulses of 150 fs duration, 0.1 nJ/pulse, at 80 MHz repetition rate from a fs Ti:sapphire laser that was set at 1.55 eV photon energy. A pump excitation at 3.1 eV was generated by doubling the 1.55 eV beam using a second harmonic generation crystal. The pump beam was focused on the sample with a diameter of ~300nm in order to generate an initial photoexcited exciton density of the order of 10^{16} cm^{-3}/pulse. The photoexcited species were monitored by the changes, ΔT of the probe transmission, T (i.e. PA) that was produced by the pump excitation. The probe spectral range was extended from 0.55 eV to 1.05 eV that was generated from an OPO Ti:sapphire based laser from Spectra Physics that gives both 'signal' and 'idler' beams. We also extended the probe spectral range from 0.25 eV to 0.43 eV by phase matching the "signal" and "idler" beams in a differential frequency crystal ($AgGaS_2$) [81]. The probe beam with a beam diameter of ~ 100nm was kept inside the larger pump beam.

The pump beam was modulated at frequency f=50 kHz using an acousto-optic modulator (AOM), and changes in transmission, ΔT were measured with an LN-cooled InSb detector (Judson IR) and a lock-in amplifier (SR830) set at f. An optical chopper operating at 300Hz was used to modulate the probe beam for measuring its transmission through the sample, T. The PA signal ($-\Delta T/T$) was calculated and recorded on the

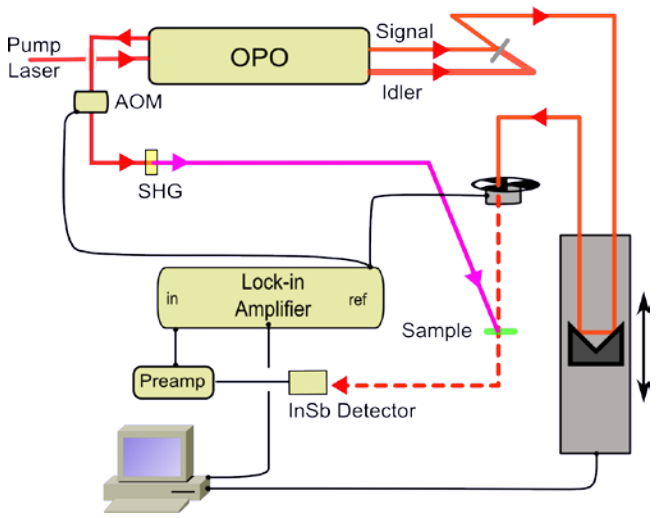

Figure 2.2: Experimental setup of the femtoseconds mid-IR OPO system. The Millennia and Ti:sapprire Tsunami are hidden from this diagram.

computer. A translation stage was introduced to the probe beam that could delay the probe pulses mechanically (1 ps=300 μm mechanical delay) thereby measuring the PA at time, *t* set by the delay line. For each probe wavelength, we swept the delay line back and forth several times until a reasonable S/N ratio was achieved. The t-PA spectrum was then constructed from the t-PA at ~50 different wavelengths.

For a weak probe beam at 1.24 eV used to monitor the PP dynamics in the PDTP-DFBT/C_{71}-PCBM blend, we used a 'double frequency' NLO crystal to generate the second harmonic from the 0.62 eV idler beam. We also used a 1300 nm 'short-pass filter' before the sample to block the 0.62 eV fundamental beam and a 'band-pass filter' centered at 1000±10 nm in front of InSb detector.

Because the lock-in amplifier is synchronized to detect the phase of the pump pulse, the in-phase signal corresponds to the transient absorption of the short-lived photoexcitations induced by the pump pulse whereas the out-phase signal carries information about the long-lived photoexcitations, and thus should be flat in the

measuring time interval up to 12.5 ns. Therefore any step-like feature in the out-phase signal at t=0 suggests that the lock-in phase is not synchronized properly to the pump pulse. Moreover, a linear slope in the quadrature signal signifies that there is a “beam walk” issue in the pump-probe optical pass. *The “beam walk”* is a ‘wandering’ of the probe beam on the sample when the stage translates to generate a time delay, *t*. This problem may originate from a combination of improper position of the “collimated lens” and/or the misalignment of the “critical mirror” sitting right before the stage. The beam walk *must be corrected physically* by realigning the “mirror” and repositioning the “collimated lens” or at least (in the exhausted case) *adjusted* (divided the transient in-phase signal by the out-phase response) using software to retrieve the true ultrafast dynamics.

The samples were thin films deposited on CaF2 substrate, which were placed in the cryostat (Montana Instrument) with a built-in electromagnet so that it can be measured at any temperature between 3K and 300K. The bipolar magneto-optic option makes the magnetic effect measurement possible at the maximum B field up to 800 mT with a pole gap of 12mm. This cryostat is state-of-the-art equipment that features low vibration (<5 nm) and stable thermal performance (±5mK).

2.2.1.2 Optical Parametric Oscillator

The Optical Parametric Oscillator (OPO) operates in a very different principle than that of a conventional laser in that it deduces its gain from a nonlinear frequency conversion process which can be viewed as sum frequency mixing. An input pump photon impinging on the Brewster-cut lithium triborate (LBO) nonlinear crystal is

converted into lower energy “signal” and “idler” photons, which satisfy the energy and momentum conservation as

$$\omega_p = \omega_s + \omega_i \tag{2.31}$$

$$k_p = k_s + k_i \tag{2.32}$$

Signal and Idler wavelengths can be turned by varying the temperature of the LBO crystal. The high conversion efficiencies in OPOs can be achieved by a synchronous pumping scheme, which matches the cavity length of the OPO to that of the Ti:sapphire pump laser so that the signal and pump pulses arrive on the crystal at the same time. The OPO was pumped by Ti:sapphire laser with 2 Watts of average power at pump wavelengths of 775nm or 810nm. When pumped at 775nm and 810nm, the OPO was configured to adapt the 1.3μm and 1.5μm optical sets, respectively, the full probe spectra capability would be obtained, ranging from 0.53eV to 1.07eV.

2.2.1.3 Polarization Memory

Since the pump and probe beams are linearly polarized, we could also measure the polarization memory and its dynamics as a function of the probe photon energy. For the transient polarization memory, we measured $\Delta T(t)$ where the pump/probe polarization were parallel, ΔT_{para} or perpendicular ΔT_{per} to each other. The polarization memory, P(t) is defined as:

$$P(t) = [\Delta T_{para}(t)-\Delta T_{per}(t)]/[\Delta T_{para}(t)+\Delta T_{per}(t)] \tag{2.33}$$

for films and

$$P(t) = [\Delta T_{para}(t)-\Delta T_{per}(t)]/[\Delta T_{para}(t)+2\Delta T_{per}(t)] \quad (2.34)$$

for solutions (because of another degree of freedom normal to the plane)

A half-wave plate was used to rotate the vertically polarized pump beam 45^0. It is better to place the half-wave plate as close to the sample as possible to avoid any circular components induced by mirror surfaces to the "not purely vertically or horizontally" polarized lights. The broadband polarizers were placed in front of the detector to measure the changes in transmission ΔT for both parallel, ΔT_{para}, and perpendicular, ΔT_{per}, polarizations with respect to the pump beam.

2.2.2 Femtoseconds VIS-IR OPA System

The high intensity, low repetition rate OPA is a home-built system, consisting of a Ti:sapphire oscillator and a Ti:sapphire amplifier. The oscillator pumped by a CW 5W, 532nm Millennia Pro from Spectra Physics is a passively mode-locked Ti:sapphire laser with an output power of 350mW at 800nm central wavelength, 76MHz repetition rate, and less than 100fs pulse duration. The low intensity pulse train from the oscillator was used to feed into a regenerative amplifier cavity. The Ti:sapphire regenerative amplifier was constructed based on the configuration from Positive Light Inc. [82]. It generates a train of pulses with 1kHz repetition rate, 800nm wavelength, and 150fs pulse duration.

The experimental arrangement is shown in Figure 2.3. The output of amplifier is split by a 90/10 beam splitter into two beams that were respectively used to pump samples

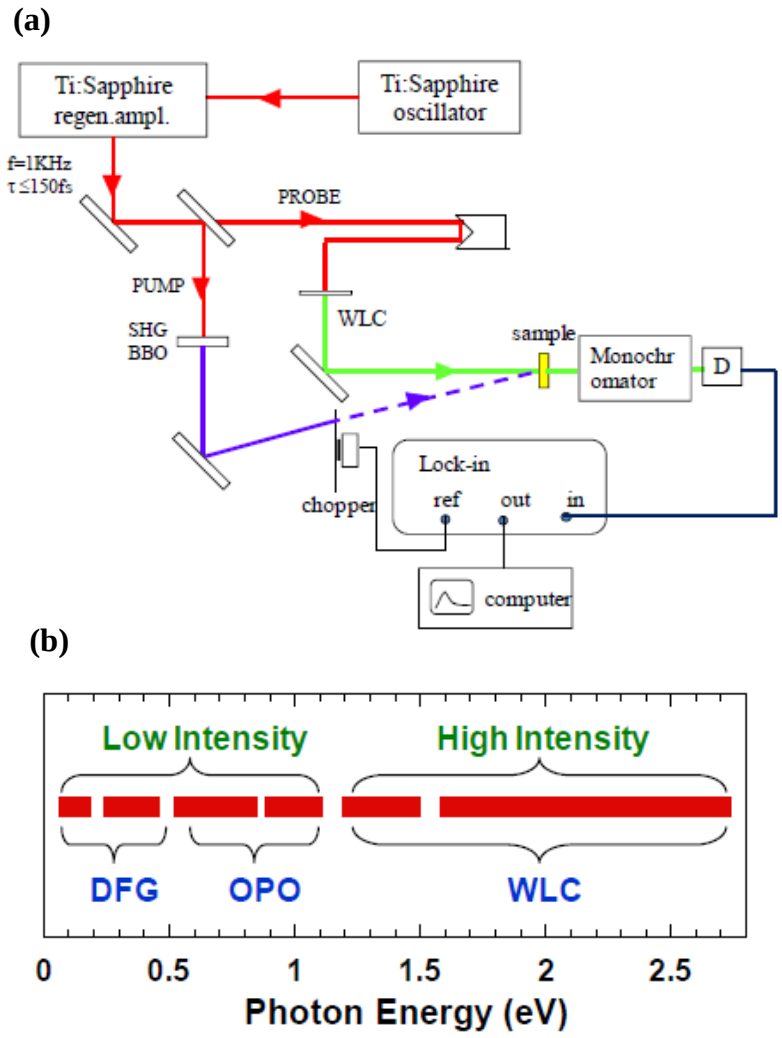

Figure 2.3: The femtosecond VIS-IR OPA system a) Experimental setup; b) The probe spectral range of both systems.

(90% power beam) and generate the broadband 400nm-1000nm white light continuum (used as the probe source WLC) by focusing a 10% power beam onto a 1mm thick sapphire plate. The pump beam is delayed with respect to the probe beam by a computer-controlled translational stage with an accuracy of ~ 100 μm (or 30 fs). A nonlinear BBO crystal was introduced to generate the pump excitation at 400nm (3.1eV). The probe WLC was collected into 0.6mm entrance and exit slits of CM-110 Digikrom

monochromator (4nm resolution). The pump beam was modulated by a mechanical chopper at 500Hz, and changes in transmission of the WLC probe, ΔT, were monitored by the Si photodiode with a phase-sensitive technique provided by the SR830 lock-in amplifier. The pump intensity was usually kept lower than 0.3 mJ/cm^2 to avoid any nonlinear-induced optical transition. Both pump and probe beams were focused onto samples so that the pump beam contains the probe beam inside its beam diameter of ~300nm.

It is critical that when measuring the PA spectrum, the chirp of WLC which is due to group velocity dispersion presenting at a different frequency part of its spectrum must be taken into account. Calibration of the WLC chirp was done by a cross-correlation or two photon absorption (TPA) of a known material.

2.2.3 Nanosecond-microsecond VIS-MIR OPO System

The block diagram of the system is shown in Figure 2.4. This is a “hybrid” version of the previous optical pump/probe spectroscopies in which the probe beam is a steady state source and the pump beam is a pulsed excitation. The pulsed excitation for this time domain was an OPO laser (Quanta-ray Indi model) operating at 10 Hz repetition rate having 10 ns pulse duration. The OPA pump at 355 nm ‘center-wavelength’ excited a basiScan OPO for generating pulses that are tunable across a broad spectral range from 410 nm to 2500 nm. The probe beam was an incandescent Tungsten/Halogen lamp at 1 kW power or a laser diode with specific wavelength. The experiment was designed for measuring small changes, ΔT in transmission, T of the probe beam induced by the pump pulse. In this case, the probe intensity seen at the detector is composed of a small AC

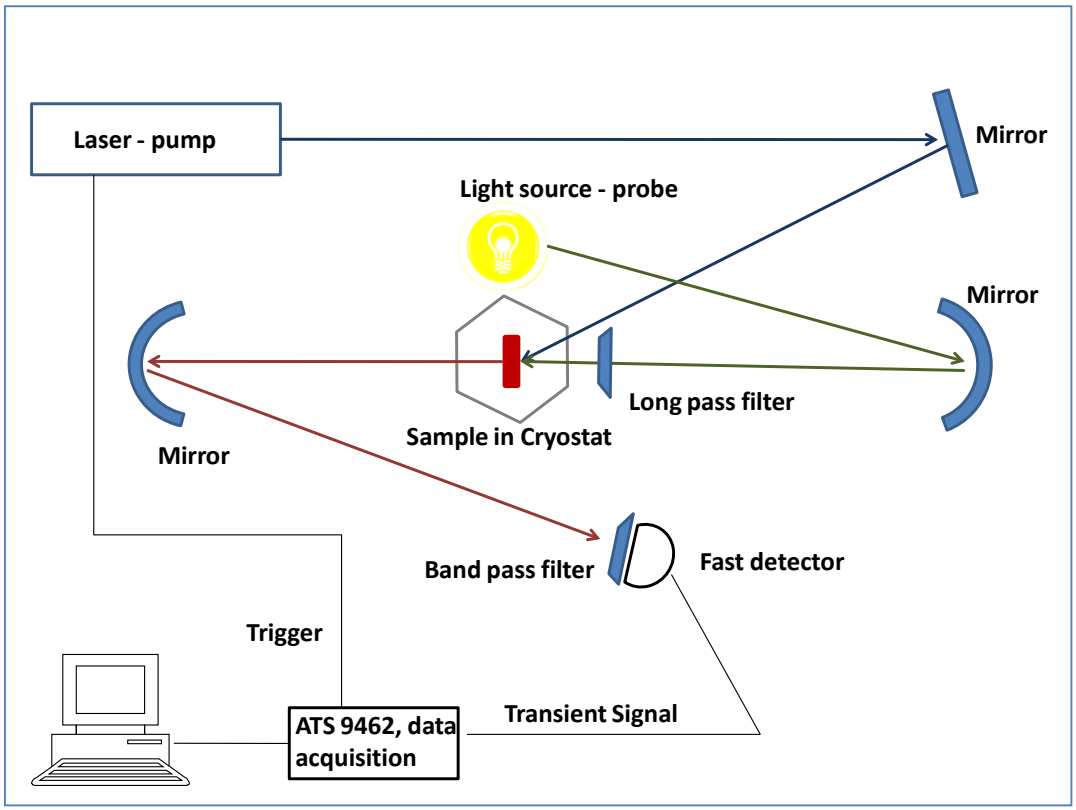

Figure 2.4: Experimental sketch of the nanoseconds VIS-MIR system.

component, ΔT, riding on the large background T. The transient part that can be easily separated and independently measured from the large DC signal represents the dynamics of photoexcitations generated by the pump pulse at particular probe wavelength. Therefore, the time resolution of this system is limited by: 1) 10ns pulse duration of the pump in convolution with the detector's electronic response; and 2) the bandwidth of the data acquisition module or digital oscilloscope.

We used three fast detectors which cover the probe energy from visible to mid-IR range; these are: the ultrafast Thorlabs Silicon DET25AL model, the ultrafast Thorlabs InGaAs DET08CL model, and the LN2 cooled InSb. The Thorlabs models, which are good for the wavelength range from 400nm to 1700nm, operate in photoconductive mode

with the rise and falling time within the picosecond time range at 50Ω load resistor as specified. We used a potentiometer to set the detector gain which can be changed from 50Ω to 10kΩ.

The InSb detector that covers the probe wavelength ranging from 1μm to 5μm works in 'photovoltaic mode' of operation, which requires a fast preamplifier to interface with. For some reason, the commercial preamplifier built specifically for this detector does not work nicely in the transient mode, showing a "ringing" pulse response in microseconds time domain. As a result, I designed and built a high-gain (up to 100kΩ) ringing-free preamplifier shown schematically in Figure 2.5. Figure 2.6 summarizes the time response of the system with 10ns pump pulse for three different detectors.

The heart of this nanoseconds setup is the data acquisition module ATS9462 (from AzalarTech) with 100MHz bandwidth which is broad enough to accommodate the 10ns pulse duration of the pump. The signal detected at the detectors was fed through the potentiometer to the channel 1 or 2 of the ATS9462 module where it will be digitized with the maximum sampling rate of 180MS/s. The input channel was set at 1MΩ input impedance and AC coupling to detect only the transient signals which carry the dynamics of the photoexcitations in nanoseconds to milliseconds time scale.

For monitoring the transient ΔT, we used several band-pass filters on the probe beam as needed, or a laser diode with specific wavelength. For this project, the pump was set at 680 nm and ΔT(t) was measured at 1300 nm using a laser diode. This wavelength was chosen because it is possible to detect both triplet and 'triplet pair' species in the PDBT-DFBT copolymer. A potentiometer was set to 1 kΩ to establish the detector gain. The time response of this setup was <0.5 μsec. The thin films were mounted in a closed cycle

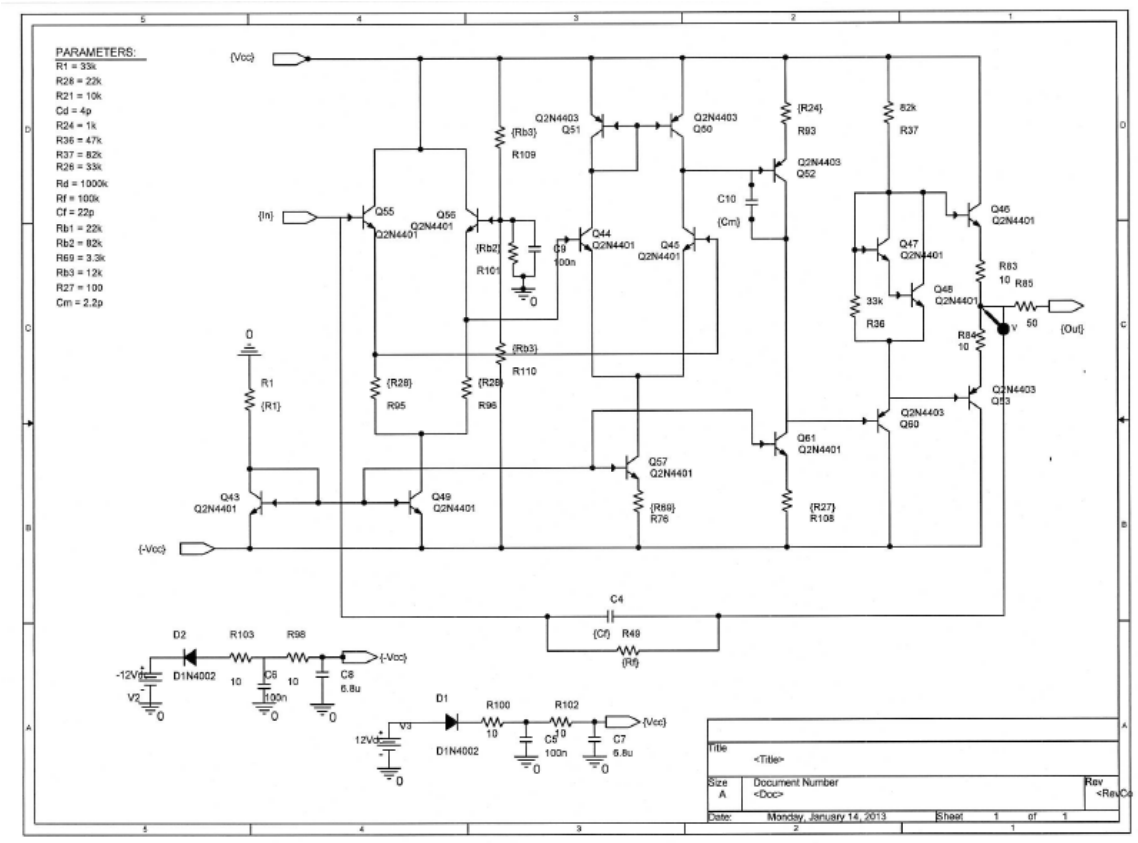

Figure 2.5: Schematic of the fast preamplifier used to interface with InSb detector.

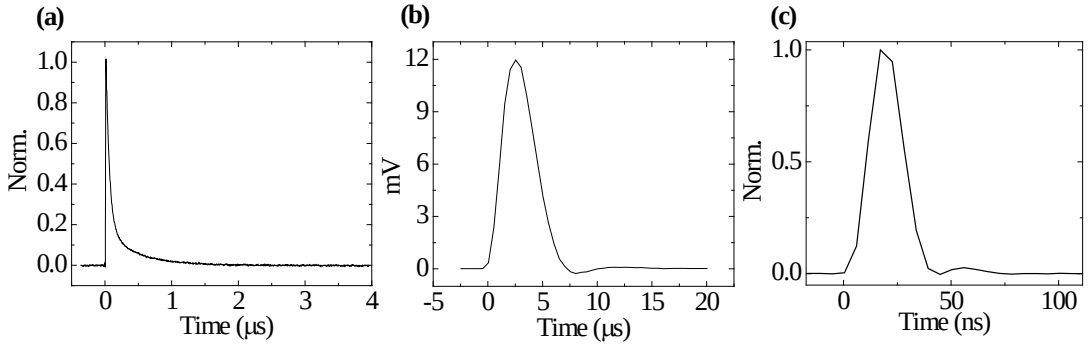

Figure 2.6: Time response of the nanoseconds VIS-IR OPA system detected with three different detectors: a) Thorlabs InGaAs DET08CL model with 1kΩ gain; b) Teledyne Judson's InSb detector and the home-built preamplifier; and c) Photo-multiplier tube PMT detector.

He refrigerator cryostat for low temperature measurements.

2.3 Magneto-Photoinduced Absorption and Magneto-Photoluminescence Spectroscopies

The ss-MPx stands for steady state magneto photoinduced absorption (ss-MPA) or steady state magneto photoluminescence (ss-MPL). The ss-MPx(B) response is defined by the relation, ss-MPx(%) = (Px(*B*)-Px(0))/Px(0), where Px(*B*) is either the PA or PL at field *B* [77,83]. It shows the percentage change of the ss-Px under the influence of a magnetic field. For measuring the ss-MPx(*B*) response, we used the same setup as for the ss-PA experiment described above (section 2.4.2) except for the magnetic field. The samples were mounted in the He cryostat and placed in between the two poles of a bipolar electro-magnet. With the limit of 2.8 Amp feeding current and the gap between the poles of 5 cm, a maximum *B* field that is achieved is ~180 mT (as measured by a magnetometer). For measuring the ss-MPx(*B*) response, we swept the feeding current of the magnet from 2.8A to -2.8A several times until a satisfactory S/N ratio was obtained.

t-MPx stands for transient magneto photoinduced absorption or transient magneto-photoluminescence, which is dubbed either t-MPA or t-MPL, respectively. Similar to ss-MPx(B), the t-MPx(t,B) response is defined as t-MPx(%) = (t-Px(t,*B*) – t-Px(t,0))/t-Px(t,0), where t-Px(t,*B*) is either the t-PA or t-PL at field *B* and time t. The t-MPx(t,*B*) response in the μsec time domain was measured using the same electromagnet as in the ss-MPx. In the t-MPx technique which is based on the nanosecond transient spectroscopy discussed in section 2.2.3, the time degree of freedom must be however taken into account. The absolute time delay in the recorded Px dynamics with respect to a

trigger event initiated by a pump pulse, which is considered to be at t=0 time, is indentified by the relation $t_d = N_{rs}/\nu_{sr}$, where N_{rs} is the number of recorded samples and ν_{sr} is the sampling rate. To measure the t-MPx(t,B) response, we first streamed several records of the t-Px(B) dynamics into the computer, averaged them, and then selected the specific data samples at the corresponding delay times for recording. This response was compiled from PA(*B*,t) dynamics at about 100 different field values from -180 to 180 mT and therefore, the S/N ratio is inferior to that of the ss-MPA.

In the picosecond time domain, the time degree of freedom was easily controlled by the mechanical delay stage (see section 2.2.1.1). However, in this time regime, there is a complication due to the background PA. Under these conditions the t-MPA(*B*) was obtained by subtracting the MPA(*B*) response of the background PA that was measured separately at *t*=-10 ps. This response is similar to the ss-MPA(*B*) response. The procedure to obtain the t-MPA is therefore the following: t-MPA(t,B)=[ΔPA(t,*B*)-ΔPA(t=-10ps,*B*)]/[(PA(t,*B*=0)-PA(t=-10ps,*B*=0)], where the terms ΔPA(t,*B*)= PA(t,*B*)-PA(t,*B*=0); PA(t=-10ps) is the background PA component; and PA(t) is the total PA signal, namely the summation of the transient PA *and* background PA.

2.4 Other Optical Spectroscopies

2.4.1 Linear Absorption Spectroscopy

The linear absorption measurement was conducted with the UV-VIS-NIR absorption CARY 17 spectrophotometer in the spectral range 300nm-2400nm at ambient conditions. For lower energy range, it was carried by the FTIR spectrometer (see next section). The absorption spectrum reveals general information about the absorptivity of materials such

as the energy bandgap, vibronic sidebands, and electronic excited states of materials. To eliminate the substrate effect, mainly reflection, the spectrum of a blank substrate was measured and then subtracted from the absorption spectra. There is no correction for reflection and scattering from samples, assuming they are negligible. Absorption was measured in units of optical density (OD) by the relation, $A = \alpha d = \log(T_0/T)$, where T_0 and T are the transmission through the blank substrate and samples, respectively, d is sample thickness, and α is the absorption coefficient.

2.4.2 Steady State PA and PL Spectroscopies

The experimental setup for the steady state photoinduced absorption and photoluminescence is schematically shown in Figure 2.7. Samples were placed in a closed cycle He refrigerator cryostat operating at low temperatures. Various laser sources, such as a 488nm Ar^+ laser, a 488nm solid-state laser, or diode lasers with changeable laser diodes from Thorlabs (the LTC100 series), were used as a pump excitation and an incandescent tungsten/halogen lamp was used as a probe source. The pump beam was modulated at frequency *f*=310 Hz with a mechanical chopper. The changes of the probe transmission, ΔT induced by the laser pump excitation, were measured using an Acton 300 monochromator, various combinations of gratings, filters, and Si, InSb photodetectors spanning the spectral range $0.3 < \omega(h\ probe) < 2.3$ eV. To increase the S/N ratio, the detector preamplifier (the PA-7-60 model from Teledyne Judson) was connected to a lock-in amplifier (SR830) referenced at *f*. It is noteworthy that the preamplifier was adjusted to high gain when using the Si detector and medium gain for the InSb detector. Before taking any measurement, it is important that the phase

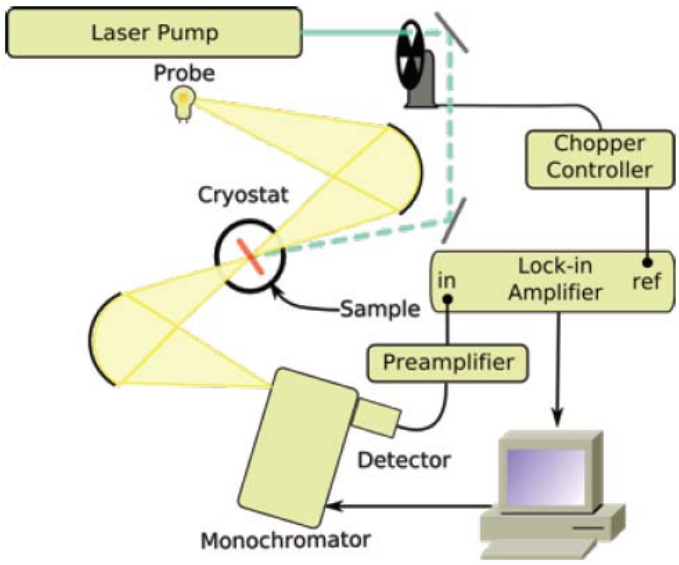

Figure 2.7: Experimental setup for steady state PA and PL measurements.

of the lock-in should be synchronized with the phase of the pump laser by blocking the probe, scattering the pump beam into the detector and auto-phasing the lock-in. By doing that, the PA signal is completely in the in-phase component.

The PA measurements were conducted in three subsequent steps: 1) Measuring the transmission of the probe beam without the pump beam, T_D; 2) Measuring the transmission changes of the probe beam, ΔT under illumination of the pump beam; and 3) Measuring the sample emission PL spectrum and subtracting it from the resulting spectra from step 2).

2.4.3 Electro-Absorption Spectroscopy

2.4.3.1 Overview of Electric Field-induced Absorption

The electric-field induced absorption (or EA) comes from two basic manifestations: the Stark effect, which is due to the mixing of discrete states by changing the

polarizability of excited states, and the Franz-Keldysh (FK) effect [84], which originates from acceleration of a free charge by the electric field through a continuum of states. While the FK effect is usually observed in inorganic materials in which the charged carriers electrons and holes are free and acquire large spatial coherence over tens of unit cell, the Stark effect is often occurred in organic counterparts such as conjugated polymers as a redshift of the π-π^* transition.

Generally, the applied electric field mixes eigenstates to create new states, described as

$$\psi_j = a\left\{\psi_j^0 + \sum_{l\neq j}\frac{\left\langle\psi_l^0\middle|\vec{\mu}_{lj}\cdot\vec{F}\middle|\psi_j^0\right\rangle}{E_j^0-E_l^0}\psi_l^0\right\}, \tag{2.35}$$

where ψ_j^0 is the zero field wavefunction, and $\vec{\mu}_{lj}$ is the transition dipole to the state ψ_l^0.

Applying second order perturbation theory results in the energy shift, which is proportional to the quadratic in the electric field

$$\Delta E_j = \sum_{l\neq j}\frac{\left|\left\langle\psi_l^0\middle|\vec{\mu}_{lj}\cdot\vec{F}\middle|\psi_j^0\right\rangle\right|^2}{E_j^0-E_l^0} = p_j\frac{F^2}{2}, \tag{2.36}$$

The polarizability p_j comes from virtual optical transitions to all states with non-vanishing dipole matrix elements.

The EA signal for π-conjugated polymers is proportional to the imaginary part of the third order nonlinear susceptibility, and can be written as

$$EA = -\frac{\Delta T}{T} = \Delta\alpha d = Im\left\{\chi^{(3)}(-\omega;\omega,0,0)\right\}.F^2, \quad (2.37)$$

where the EA signal scales with F^2, exhibiting a quadratic Stark effect.

The linear Stark-shift signal is absent in films in which the polymers are randomly oriented because there is no preferential dipole orientation that cancels the effect [85,86]. The EA technique helps to reveal forbidden optical transitions between two states with the same parity which are hidden from the linear absorption spectrum. The applied electric field breaks the spatial symmetry of electronic wavefunctions and hence relaxes transition restrictions. In general, the EA spectrum consists of two dominant optical features: a derivative of the linear absorption with respect to photon energies (dα/dE) and a field-induced absorption which is absent from the absorption spectrum.

2.4.3.2 Experimental Setup

Figure 2.8 shows the experimental setup for EA measurements. A “200V-300V at 500Hz” AC electric field, generated using a signal generator and transformed using a step-up transformer, is applied to an EA substrate with deposited films in the form of an interdigitated gold electrode array pattern with a 40μm gap between the adjacent electrodes fingers as also shown in Figure 2.8. To minimize the effect of carrier injection into the organic layer from the applied electric field, which might contribute some unexpected absorptions to EA spectrum, the resistance of the EA substrate should be checked to make sure it is as large as possible, say in MΩ range. A xenon or tungsten light source was used as the probe light which was dispersed through the grating monochromator and guided through the sample onto detectors as described in section

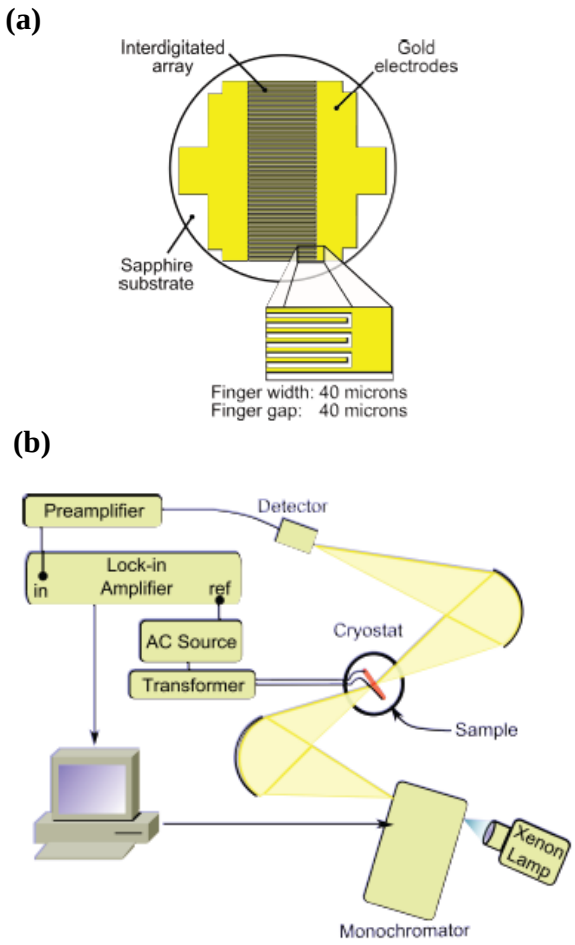

Figure 2.8: Schematic of EA experimental setup a) Structure of the EA interdigitated array electrodes substrate; b) The experimental stretch of EA measurements.

2.4.2. The sample was mounted on the cold finger cryostat. Using the phase-sensitive modulation technique, a reference signal was taken from the signal generator and the detectors were connected to an input of the SR830 lock-in amplifier. The EA spectrum was detected at the second harmonic 2*f*, indicating a quadratic EA signal is generated.

2.4.4 FTIR Spectroscopy

The working principle of Fourier Transform Infrared spectroscopy (FTIR) is based on the Michelson interferometer in which an input beam I_0 is split by a beam splitter into

two beams, I_1 and I_2, which are subsequently reflected from a fixed mirror and a moving mirror, respectively. The moving mirror can change optical path length of the I_2 beam by x. The two reflected beams are combined at the beam splitter and then pass through samples to generate an interferogram spectrum described by

$$I_{out}(x) = \frac{1}{4}\int_{-\infty}^{+\infty} I_0(\bar{\nu})[1 + \cos(2\pi\bar{\nu}x)]d\bar{\nu} = constant + \frac{1}{4}\int_{-\infty}^{+\infty} I_0(\bar{\nu})\cos(2\pi\bar{\nu}x)\,d\bar{\nu}, \quad (2.38)$$

where $I_{out}(x)$ is the interferogram spectrum as function of displacement x. The inverse Fourier transform of the second part of the equation (2.38) describes the interference spectrum as function of wavenumber $\bar{\nu}$ as

$$I_0(\bar{\nu}) = \frac{2}{\pi}\int_{-\infty}^{+\infty} I_{out}(x)\cos(2\pi\bar{\nu}x)\,dx, \quad (2.39)$$

The FTIR spectrometer was mainly used to measure the linear absorption in the optical range from mid-IR to far-IR for which a Globar lamp is used as the input beam I_0. Alternatively, we also used it to construct the mid- to far-IR PA spectrum as follows:

$$-\frac{\Delta T}{T} = (T_{on} - T_{off})/T_{off}, \quad (2.40)$$

where $T_{on}\ and\ T_{off}$ are the spectrum with and without illumination by a pump laser, respectively. The PA-FTIR experimental setup is outlined in Figure 2.9. The pump laser passes through a shutter switch controlled by the FTIR computer. An IR beam from the

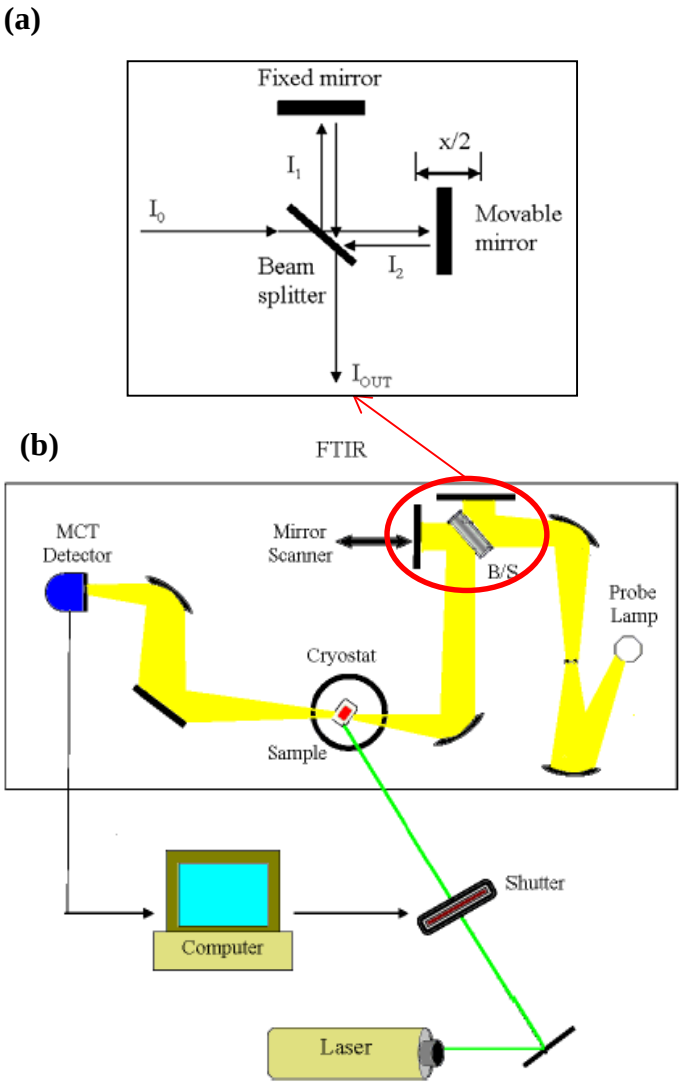

Figure 2.9: FTIR experimental setup a) Structure of Michelson Interferometer extracted from the FTIR experiment; b) Block diagram of the FTIR experimental setup.

Globar lamp used as the probe is split by the KBr beam splitter. The probe beam passes through samples to a MCT detector that is cooled by liquid nitrogen.

CHAPTER 3

PHOTOPHYSICS OF LOW BANDGAP COPOLYMERS FOR OPV APPLICATIONS

3.1 Introduction

With the introduction of the low bandgap (LBG) copolymers, PTB7 and PDTP-DFBT (see Figure 1.4 for their chemical structure), by researchers at the University of Chicago and the University of California-Los Angeles, a new obtained record PCE of ~8% for a single layer BHJ OPV cell was reported[24,25]. Other LBG copolymers with similar D-A structure in the unit cell have also been recently reported having a comparable or even higher PCE value of ~ 10% [87]. These copolymers exhibit smaller energy (or optical) gap compared to the homopolar polymer counterparts, extending the absorption of the solar spectrum beyond 600 nm into the near-IR spectral range [88]. There were several explanations given for the high PCE of the LBG copolymer OPV [24,88,89]. Among them, the ability to absorb more solar irradiation has been the principal explanation. However, because of the lower bandgap, there is more energy dissipation following the photon absorption and, in addition, the polymer donor does not absorb light at high photon energies; these cast doubts on the previous explanations given for the high PCE in OPV cells based on the LBG copolymers.

Despite the promise for a novel class of OPV materials, there is still a lack of thorough spectroscopic studies on the LBG copolymers, probably since the optical probes should cover the mid-IR spectral range that is not accessible with standard, commercially available pump-probe setups. The motivation behind the present work is to better understand the charge photogeneration dynamics in this new class of OPV materials compared with the basic model for charge photogeneration in more regular π-conjugated polymers [90-93]. The OPV fundamental operating process is the photogeneration of singlet excitons in the donor polymer chains followed by their separation into electron-hole polaron pairs at the D-A interfaces. Thus understanding the kinetics of different photoexcitations in the pristine copolymer donors and their blend with fullerene acceptors (PCBM) is a crucial step for elucidating the mechanism for charge carrier photogeneration in the BHJ OPVs. In this chapter, we thoroughly study the optical properties of two LBG copolymers, namely PTB7 and PDTP-DFBT, and their blend with $PC_{71}BM$ that gives a record high PCE of 8% in the optimal BHJ solar cell. The photophysical studies have revealed an interesting physical phenomenon, dubbed 'singlet fission' (SF) and its crucial role in the charge photogeneration process. This understanding may shed light on the possibility of designing new organic compounds that may be used in various device fabrication techniques for extracting two electrons and two holes from one absorbed photon, thereby doubling the photocurrent.

Various optical spectroscopies that include transient photoinduced absorption (t-PA), steady state photoinduced absorption (ss-PA), electro absorption (EA), and doping-induced absorption (DIA) have been used to study the photophysics of the thin film copolymers and their blend with $PC_{71}BM$ (see Chapter 2, Experimental Setup for detailed

description).

3.2 Materials

The PDTP-DFBT copolymer was synthesized at the University of California-Los Angeles. The synthetic route, chemical structure, BHJ solar cell device fabrication, and PCE measurements were described in refs. [25,47], respectively. For the PTB7 copolymer, it was either synthesized at the University of Chicago [24] or bought from Sigma Aldrich. Neat films were prepared by drop casting or spin coating from a solution of pristine copolymers (or copolymers/$PC_{71}BM$ blend with mixing ratio 1:2 by weight) dissolved in dichlorobenzene (7mg/ml for PDTP-DFBT or 10mg/ml for PTB7) on CaF_2 substrates for t-PA measurements, and on sapphire substrates for all other optical measurements. Thin films of isolated chains of pristine copolymers were also prepared by drop casting from a dilute solution of pristine copolymers mixing with polystyrene in dichlorobenzene with mixing ratio 1:1000 by weight. The $PC_{71}BM$, [6,6]-Phenyl C_{71} butyric acid methyl ester > 99% fullerene powder were bought from Sigma Aldrich and used as received. All solutions and films were prepared in a glove box filled with N_2.

For the doping-induced absorption measurements, a pristine PDTP-DFBT film was doped with $HAuCl_4$, which is known to be a strong acceptor. The $HAuCl_4$ powder was first dissolved in acetonitrile at 0.01M concentration, and stirred overnight to mix uniformly. The film was then dipped in the solution for ~1 minute. For the PTB7, a pristine film was exposed to iodine vapor for 1 minute, and the linear absorption was measured before and after the iodine exposure.

3.3 Photophysics of Pristine Copolymers

3.3.1 PDTP-DFBT Copolymer

The PDTP-DFBT copolymer absorption and photoluminescence (PL) spectra are shown in Figure 3.1a. The Stokes shifted 0-0 PL band peaks at 1.38 eV, considerably lower than in any traditional PCP. This enhances the absorption from the solar spectrum, which may contribute to the high efficiency OPV performance of this compound [94]. In order to more precisely determine the energies E(1^1B_u) and E(m^1A_g) in this copolymer, we measured the electro-absorption (EA) spectrum of pristine PDTP-DFBT film deposited on an inter-digitated electrode substrate subjected to a modulated voltage at frequency *f* (see Chapter 2, Experimental Setup). In general, the EA spectrum of PCPs shows two dominant optical features; a derivative-like Stark effect feature at E(1^1B_u), and a field-induced absorption at E(m^1A_g) due to the partial symmetry breaking associated with the applied field [17,95]. The EA spectrum of PDTP-DFBT (Figure 3.1b) exhibits a derivative-like feature with zero-crossing at ~1.55 eV, which we identify as E(1^1B_u); and a positive band with 0-0 at ~1.95 eV, which we assign as E(m^1A_g) (see Figure 3.2b). The energy difference, $\Delta E = E(m^1A_g) - E(1^1B_u) \approx 0.4$ eV, is an estimation of the exciton binding energy in PDTP-DFBT, which is considerably lower than that in traditional homopolymer PCPs [96,97]. The low exciton binding energy may also be behind the high efficiencies of OPV cells based on this copolymer. We note that ΔE is also expected to be the transition energy of the photoinduced absorption (PA) band from the photogenerated 1^1B_u into the m^1A_g, namely PA_{SE} (Figure 3.2b) [97,98].

Figure 3.2a depicts the steady state PA (ss-PA) spectrum in a film of solid state solution, in which isolated pristine PDTP-DFBT chains are embedded in polystyrene (see

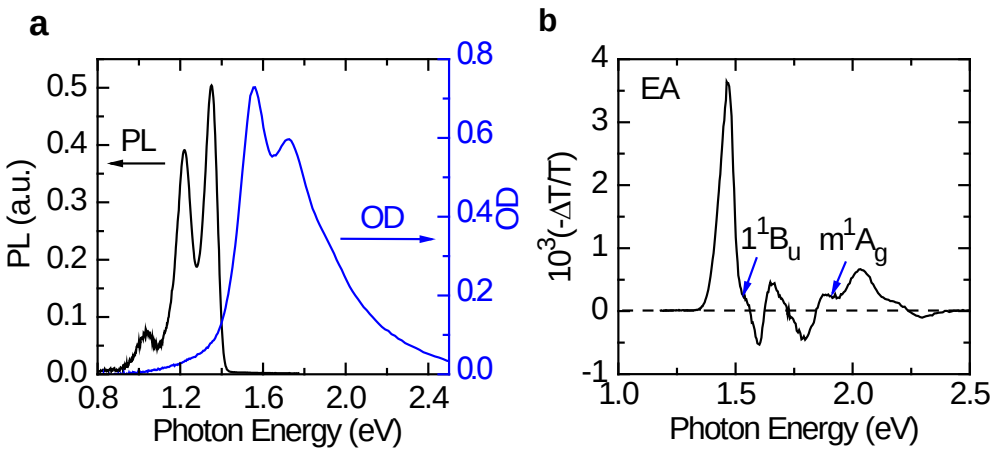

Figure 3.1: Materials characterization (a) The photoluminescence (PL) and absorption spectra of the PDTP-DFBT copolymer film. (b) The electroabsorption (EA) spectrum, where the two important excited states in the singlet manifold are assigned.

Materials section 3.2). The spectrum was measured at 1 kHz modulation frequency and 300K, using the background PA in the ps pump-probe measurement (see experimental setup, Figure 2.1). The ss-PA spectrum is dominated by a single PA band (PA_T) that peaks at ~0.95 eV, which we assign, as in many other PCPs, to the strongest transition from the lowest triplet exciton [97,99]. To strengthen this assignment, we performed PL-detected magnetic resonance (PLDMR) and magnetic field-dependent PA (ss-MPA) (see Chapter 2, experimental setup) to identify the spin state of these long-lived species (Figure 3.2). The PLDMR(*B*) response shows a 'full-field' powder pattern around B_0=1010 Gauss, which is typical to triplet excitons, T (or 1^3B_u) [99,100] . From the PLDMR powder pattern, we can determine the zero-field splitting (ZFS) parameters, *D* and *E*, of the triplet exciton in PDTP-DFBT. In general, the spin triplet full-field powder pattern has singularities at $B_0 \pm D$ and peaks at $B_0 \pm (D \pm 3E)/2$, and thus we obtain *D*=38 mT and *E*=15 mT from the PLDMR(*B*) spectrum. We also performed steady state magneto-PA (ss-MPA(*B*)), where MPA=[PA(*B*)-PA(0)]/PA(0) and *B* is the magnetic field, at the

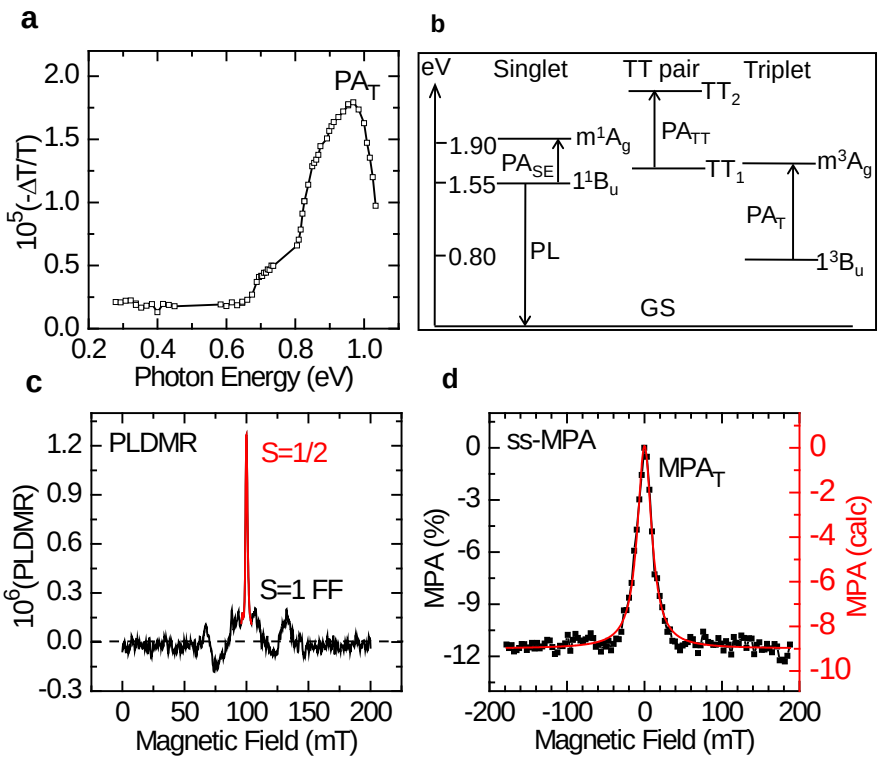

Figure 3.2: Steady state (ss) spectroscopies of pristine PDTP-DFBT π-conjugated copolymer. (a) The steady state photoinduced absorption (ss-PA) spectrum measured via the background PA in the pump-probe correlation, modulated at 1 kHz. The triplet PA (PA_T) is assigned. (b) Schematics of the main energy levels and associated optical transitions in three different manifolds of the copolymer, namely: singlet, TT pair, and triplet, respectively. (c) The PL-detected magnetic resonance (PLDMR) spectrum of the copolymer measured at 10K. The full-field (FF) triplet powder pattern (black) and spin ½ resonance line (red) are assigned. (d) The steady state magneto-PA (ss-MPA(*B*)) response of the PA_T band measured at 40K. The line through the data points is a fit based on individual triplet exciton using the zero-field splitting parameters D=38 mT and E=15 mT.

PA_T band (Figure 3.2d), which shows a typical response of triplet excitons [100]. In fact, the ss-MPA(*B*) response can be fit using the same ZFS parameters extracted from the PLDMR(*B*) response.

Since we determined $E(m^1A_g)\approx1.95$ eV from the EA spectrum, we can estimate its triplet counterpart, $E(m^3A_g)$, that is lower by about 0.2 eV [95,97], namely $E(m^3A_g)\approx1.75$ eV. Consequently, from $E(m^3A_g)$ and PA_T transition energy, we can determine the energy

of the lowest triplet exciton in PDTP-DFBT, $E(1^3B_u)= E(m^3A_g)-E(PA_T)\approx 0.8$ eV (Figure 3.2b). This value is in agreement with an alternative estimation starting from $E(1^1B_u)$, since the energy gap, Δ_{ST} between 1^1B_u and 1^3B_u in PCPs is of the order of 0.7-0.8 eV [101]. It is thus clear that the lowest singlet in PDTP-DFBT (=1.55 eV) is nearly resonant with twice the lowest triplet (2x0.8=1.6 eV), i.e. $E(1^1B_u) \approx 2E(1^3B_u)$), which signifies the isoergic or slightly endoergic nature of singlet fission in this copolymer [102].

Figures 3.3 shows the picosecond (ps) transient PA (t-PA) study in the mid-IR spectral range of pristine PDTP-DFBT in a solid state solution film, measured by the two colors pump-probe correlation method (see the experimental setup in Chapter 2). At pump excitation of 1.55 eV, rather surprisingly, the t-PA spectrum consists of *two PA bands* at 0.4 and 0.82 eV, respectively, which are formed within the experimental time resolution (~350 fs). This is in sharp contrast to t-PA spectra of traditional homopolymer PCPs, which are dominated by a *single* PA band that corresponds to PA from the SE to m^1A_g (i.e. $1^1B_u \rightarrow m^1A_g$; [79,97]). The two PA bands in PDTP-DFBT have different polarization memory values (Figure 3.3c and 3.3d). We therefore conclude that the two PA bands do not belong to the same photoexcitation species. We identify the low-energy PA band as due to SE, PA_{SE} ($1^1B_u \rightarrow m^1A_g$, Figure 3.2b), since it matches the energy difference $\Delta E = E(m^1A_g) - E(1^1B_u)$ obtained from the EA spectrum. In contrast, the high energy PA band does not match any known transition in the singlet manifold of traditional PCPs [103] or copolymers [104]. It is also different from the PA of triplet exciton PA_T in energy, and has much faster dynamics. It also does not match optical transitions related to polarons or polaron-pairs (PP) in PDTP-DFBT. We thus tentatively identify the high energy PA band as due to a transition in the TT manifold, i.e. PA_{TT}

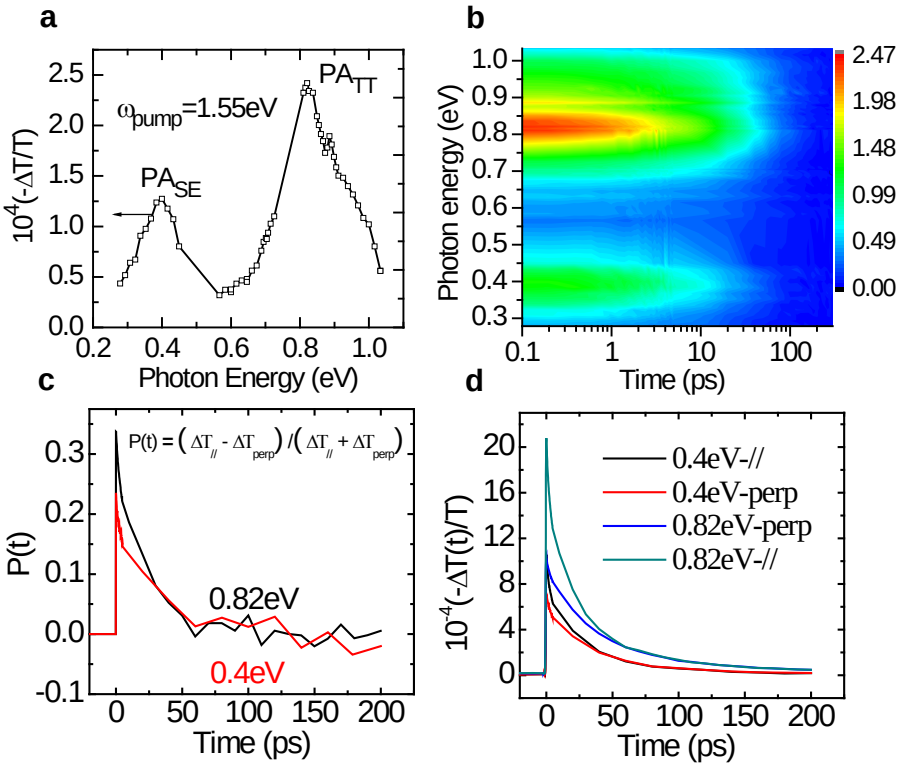

Figure 3.3: Room-temperature ps transient spectroscopies of pristine PDTP-DFBT embedded in a polystyrene matrix. (a) The transient PA (t-PA) spectrum in the mid-infrared measured at t=0, with pump excitation at 1.55 eV. The transient PA bands PA_{SE} (singlet exciton) and PA_{TT} (TT pair) are assigned. (b) 2D presentation of the t-PA spectrum evolution excited at 1.55 eV, using false colors. (c) Polarization memory (POM) decay of the SE (measured at 0.4 eV) and TT pair (measured at 0.82 eV) in pristine PDTP-DFBT film. Note that the initial POM value, P(0), as well as the POM decay, P(t), are different for the SE and TT photoexcitations. (b) The PA decays of the SE and TT photoexcitations measured with pump-probe polarization parallel and perpendicular to each other. We note that P(t) in (c) was calculated using these decays.

(Figure 3.2b). The transient magnetic field effect t-MPA (to be discussed in Chapter 4) gives additional support to our assignment (see Chapter 2, section 2.3 for descriptions of the t-MPA technique).

Interestingly the two PA bands, PA_{SE} and PA_{TT} in Figure 3.3a, establish dynamics equilibrium with each other, showing the similar dynamics as well as the polarization dynamics within several hundred ps decay time (Figure 3.4). It also means that these two

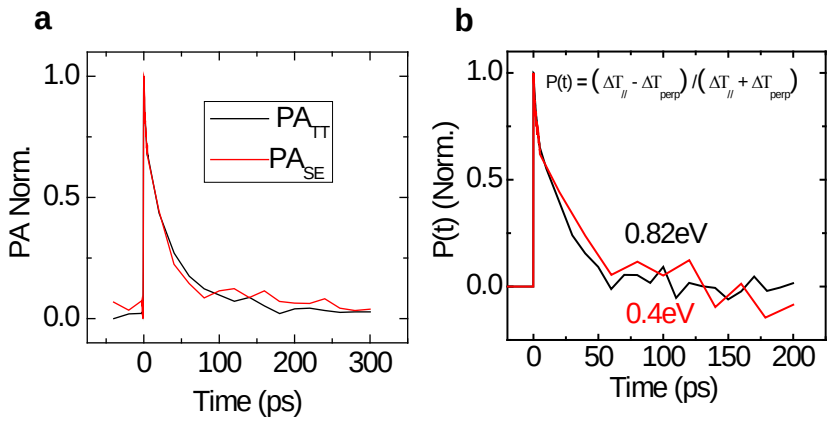

Figure 3.4: PA dynamics comparison (a) Picosecond dynamics of PA_{TT} and PA_{SE} and (a) Polarization memory dynamics of PA_{TT} and PA_{SE}**.**

states coherently interact with each other in which they exchange the population through the forward fission and backward fusion processes. Taking all these analyses together, the 1.55eV optical excitation may initially generate a coherent superposition of SE and TT states in which the TT state can be populated instantaneously with the SE, as observed by Chan et al. in polycrystalline thin films of pentacene and tetracene [53,105], which supports the quantum coherent model proposed by several authors and their coworkers [55,106-108]. Then the route of singlet fission in the PDTP-DFBT copolymer is described as follows

$$1^1A_g \longrightarrow [1^1B_u \Leftrightarrow TT] \longrightarrow TT \longrightarrow 1^3B_u + 1^3B_u \qquad (3.1)$$

where the TT decouples from the $[1^1B_u \Leftrightarrow TT]$ state through the interaction of the $[1^1B_u \Leftrightarrow TT]$ state to the phonon bath and it dissociates into two individual triplets though the coherent loss of their spin. It also notes that the superposition state of $[1^1B_u \Leftrightarrow TT]$ might

last for hundreds of picoseconds that leads to the dynamics equilibrium of the SE and TT states in the same time scale.

Figure 3.5 shows the t-PA spectrum of PDTP-DFBT pristine in solution and its evolution. Similar to that of the isolated chains embedded in polystyrene, the t-PA in solution at time t=0ps (Figure 3.5a, black curve) shows two bands at 0.4eV and 0.82eV, which were identified as the absorption of the SE and triplet pair, respectively. The t-PA spectral evolution up to 500ps (Figure 3.5b) clearly shows a blue-shift to the triplet extiton band, which is at 0.95eV as determined by PLDMR and ss-MPA (Figure 3.2). This early blue-shift results in a significant buildup of triplet excitons in the background spectrum (Figure 3.5a, red curve) which is the same as the ss-PA of triplet excitons in the isolated chains (Figure 3.2a). The blue-shift of the TT band in picosecond time domain signifies the fast coherent loss of two triplets in the TT pair, probably resulting from the tumbling motion of the polymer chains in solution under excitation.

Figure 3.6 shows the t-PA spectrum in thin films of the pristine PDTP-DFBT. Rather

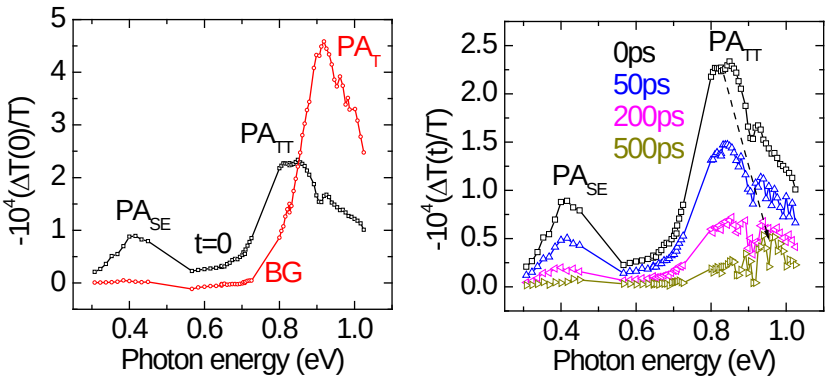

Figure 3.5: Picosecond t-PA measured in pristine PDTP-DFBT solution, (a) t-PA spectrum at t=0 (black curve) and background spectrum (red curve). (b) t-PA spectral evolution up to 500ps shows a blue-shift to the triplet exciton band.

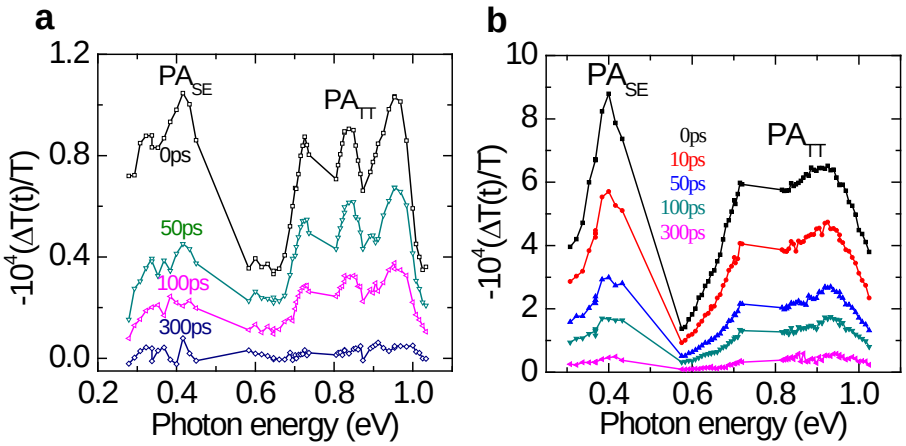

Figure 3.6: Picosecond t-PA measurement of the pristine PDTP-DFBT film (a) at room temperature and (b) at low temperature 40K.

surprisingly, at room temperature, the PA_{TT} band splits into three sub-bands with a main peak of 0.82eV and the other two shifted ~ 100meV equally around it (Figure 3.6a). The equal distribution of three sub-bands in energy may originate from the three phonon side bands of TT transitions. Another possibility is the interchain interaction in films which causes the splitting. However, at low temperature, the middle 0.82eV peak is suppressed (Figure 3.6b), which casts doubt on the first speculation of vibronic contribution. The difference in decay dynamics of SE and TT states, the PA_{SE} decays faster than the PA_{TT}, in thin films suggests that the TT state may decouple from the superposition state of [SE⇔ *TT*] at very early time, resulting from the strong interaction of these two states to the phonon reservoir.

3.3.2 PTB7 Copolymer

Figure 3.7 shows the absorption and photoluminescence spectra of PTB7 films measured at room temperature. The absorption spectrum has two peaks at 1.84eV and

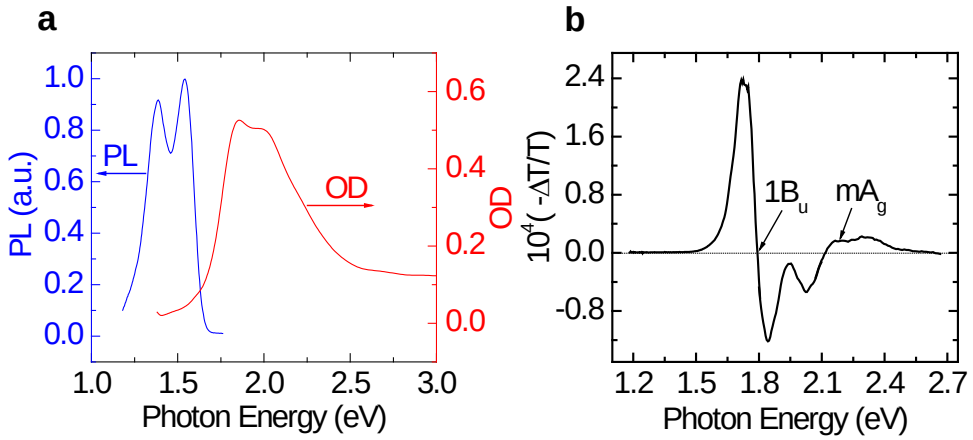

Figure 3.7: Materials characterization (a) The photoluminescence (PL) and absorption spectra of the PTB7 copolymer film. (b) The electroabsorption (EA) spectrum, where the two important excited states in the singlet manifold are assigned.

2.02eV, which corresponds to the 0-0 and 0-1 vibrational transitions, mainly due to the C=C stretching mode with vibration frequency 1500 cm^{-1} (180 meV). The photoluminescence spectrum has an unprecedentedly large Stoke shift of ~300 meV, the distinct feature of low bandgap copolymers, which might be due to the existence of a triplet pair TT with overall spin singlet configuration.

In order to check the energetic requirement for singlet fission in the PTB7, ideally $E_{SE} \sim 2E_T$ should occur for high efficient singlet fission yield [54,102]; thus we measured the electro-absorption spectrum to determine the lowest singlet exciton energy level $E(1^1B_u)$ and the most strongly coupled singlet exciton state $E(m^1A_g)$. Even though the PTB7 backbone structure does not share the same group symmetry of traditional pi-conjugated polymers PCP, for convenience, we still use the same notations of the PCP irreducible representations to refer to various excited states of this copolymer, such as 1^1B_u for the lowest singlet exciton, m^1A_g for the most strongly coupled singlet exciton, and their equivalence in the triplet manifold, namely 1^3B_u and m^3A_g. The EA experimental setup is

described in Chapter 2. The EA-spectrum of the PTB7 pristine film deposited on an inter-digitated electrode gold substrate shows a derivative-like feature with first zero crossing at 1.8eV, which we assign to the lowest energy level of the 1^1B_u state; and a first positive band 0-0 at 2.2eV, which we identify as the lowest E(m^1A_g) (Figure 3.7b). The energy difference, $\Delta E = E(m^1A_g) - E(1^1B_u) \approx 0.4$ eV, is an estimation of singlet exciton binding energy in this copolymer. It also equals the optical transition of singlet excitons, namely PA_{SE} observed in the transient PA spectrum of isolated chains of pristine PTB7 as follows.

Figure 3.8a shows the steady state PA (ss-PA) spectrum of the PTB7 pristine film. The spectrum is dominated by a band at 1.1eV, which we assign for the triplet exciton transition from 1^3B_u to m^3A_g, E(PA_T). To further strengthen this assignment, we measured the PA-detected magnetic resonant (PADMR) spectrum of the pristine film (see ref. [109] for the experimental setup). The PADMR spectrum (Figure 3.8b) measured at 1.1 eV depicts both spin triplet full-field powder pattern around B_0=1006 Gauss, with divergences at B_3 =1160 Gauss and B_4= 817 Gauss; and the half-field one with a divergence at B_{HF}=416 Gauss. Using equations for full-field and half-field's divergences, $B_{3,4} = B_0 \mp \frac{D-3E}{2}$ and $B_{HF} = \frac{1}{2}\sqrt{B_0^2 - (D+E)^2}$, we can estimate the ZFS parameters D ~ 510 Gauss and E ~ 56 Gauss [110], respectively. These D and E values are not different from those of homopolymers [77,78], signaling that the triplet exciton is indeed a localized photoexcitation species that is robust against changes in the polymer backbone structure. Furthermore, the ss-MPA spectrum (Figure 3.8c) measured at the PA at 1.1eV shows a typical triplet pattern which was also used to identify the triplet exciton in the literature [77]; this further confirms that the 1.1eV peak in the ss-PA spectrum is

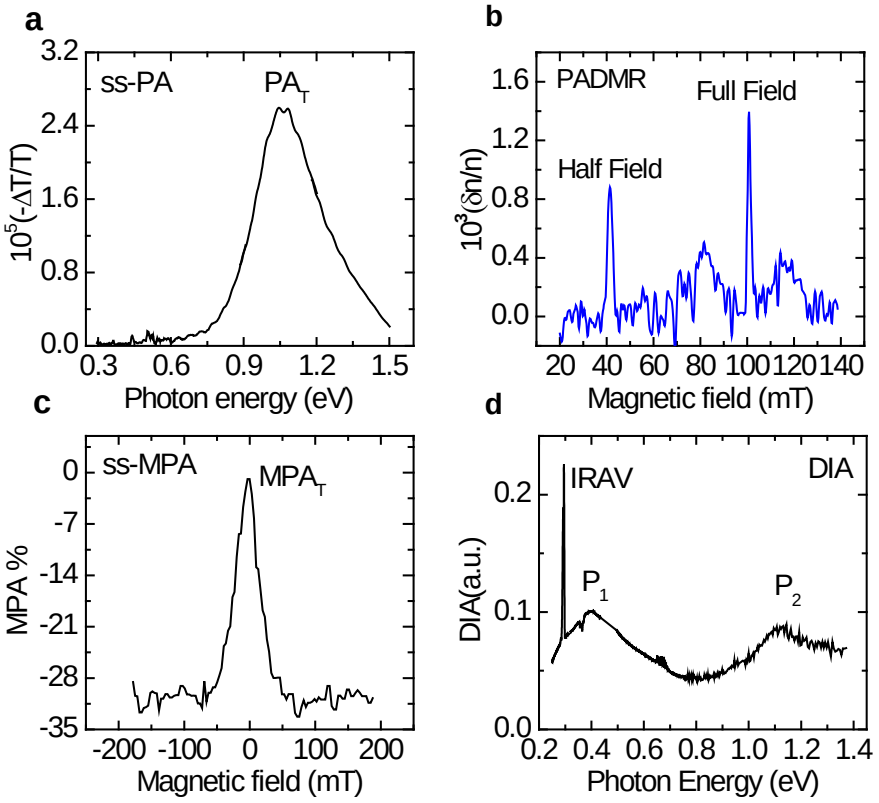

Figure 3.8: Steady state measurements on PTB7 thin films (a) The steady state photoinduced absorption (ss-PA) spectrum in which the triplet PA (PA_T) is assigned. (b) The PA-detected magnetic resonance (PADMR) spectrum of the PTB7 copolymer measured at 10K. Both the full-field (FF) and the half-field (HF) triplet powder pattern are assigned. (c) The steady state magneto-PA (ss-MPA(*B*)) response of the PA_T band measured at 40K. (d) Doping-induced absorption (DIA) spectrum of pristine PTB7 films doped with Iodine vapor measured at room temperature. The DIA and PA bands P_1 and P_2 of polarons in the copolymer chains are assigned.

due to the absorption of the triplet exciton.

We are now in good position to check the energetic requirement for singlet fission in this copolymer. Since we know $E(m^1A_g)$ = 2.2 eV from the EA-spectrum, we can estimate $E(m^3A_g)$~ 2 eV that is generally 0.2 eV lower than $E(m^1A_g)$. As a result, the lowest triplet energy $E(1^3B_u)$ can be determined by $E(1^3B_u) = E(m^3A_g) - E(PA_T)$, which is about 0.9 eV. It is thus clear that the lowest energy level of singlet excitons,

$E(1^1B_u)$~1.8eV, in PTB7 is approximately twice that of the lowest triplet, $E(1^1B_u) \sim 2\ E(1^3B_u)$, which calls for the high singlet fission yield in the PTB7 copolymer too.

Figure 3.9 shows the t-PA spectrum of isolated chains of the pristine PTB7 embedded in PS at time t=0 and its time evolution in the picosecond time domain, measured with the transient pump-probe photomodulation spectroscopy (see Chapter 2, section 2.2). At pump energy 1.55eV, it is clear that there are two PA bands, which are formed within the experimental resolution 300fs; the low energy (LE) band that peaks at 0.4eV and the higher energy PA(HE) at 0.95eV. They have different dynamics (Figure 3.9b), in particular the LE band decays faster than the HE t-MPA responses, discussed in Chapter 4; and also excitation dependence, the HE band is much stronger than the LE when pumped at 3.1eV energy (Figure 3.9a). We therefore conclude that these PA bands do not originate from the same photoexcitation species. From the EA spectrum (Figure 3.7), we know that the LE band is due to the absorption of singlet excitons PA_{SE}. However, the HE band does not match any transitions in the singlet manifold or the PA of triplet exciton PA_T, which is about 1.1eV (see Figure 3.8a). It is also different from the optical transition of polarons or polaron pairs in the PTB7 film doped with Iodine vapor (see Figure 3.8d). Taking all of the above analyses into account, we can assign the HE band to the optical transition of a new photoexcitation species, namely the PA_{TT} in the triplet pair manifold. The transient magneto-photoinduced absorption studies presented in Chapter 4 will provide more evidence for this assignment.

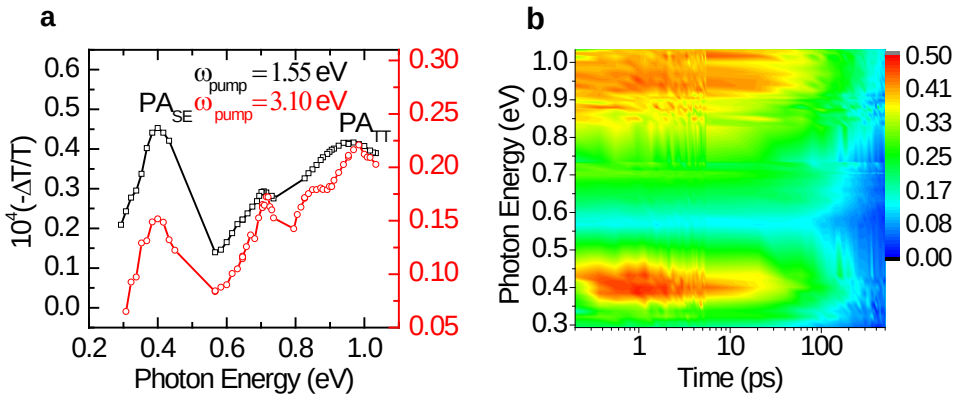

Figure 3.9: Picosecond PA spectrum (a) The transient PA (t-PA) spectrum of PTB7 pristine embedded in PS in the mid-infrared measured at *t*=0, with pump excitation at 1.55 eV (black) and 3.1 eV (red), respectively. The transient PA bands PA_{SE} (singlet exciton) and PA_{TT} (TT pair) are assigned. (b) 2D presentation of the t-PA spectrum evolution at 1.55 eV excitation energy, using false colors.

3.4 Photophysics of Copolymers/fullerene Blends

Photophysics of pristine copolymers has shown the existence of intrachain singlet fission with the novel triplet pair (TT) state which is the state of two correlated triplets. The role of singlet fission and TT state in charge photogeneration and charge loss processes in bi-layer hetero-junction OPVs has been extensively studied in recent years [105,111]. Several reports have demonstrated the possibility of TT dissociation into "one or even two" free electrons and holes at the D-A interfaces [105]. Since the efficiency of bi-layer solar cells is limited by the exciton diffusion length as discussed in Chapter 1, it is common that none has reported a breakthrough in power conversion efficiency of these OPV cells. Moreover, attempts to harvest more than 100% EQE obtainable triplets from singlet fission [53,112] for free charges to generate photocurrent has not been successful, given that the energy of triplet is lower than that of the CT state formed at the D-A interfaces. In this section, we investigate the role of intrachain singlet fission and triplet pairs in the copolymers for charge carrier photogeneration and charge carrier loss

processes in the BHJ film of donor copolymers doped with the PC_{71} BM fullerene acceptor.

3.4.1 PDTP-DFBT/ PC_{71} BM Blend

We now determine whether the TT state can be ionized in donor-acceptor (D-A) blend, thereby generating e- and h-polarons that contribute to OPV applications. For recognizing the signature of charge excitations in PDTP-DFBT copolymer, we first obtained the charge polaron absorption spectrum in pristine film by doping with a strong acceptor, $HAuCl_4$ (see the Materials section 3.2) shown in Figure 3.10a. We identify two broad doping-induced absorption (DIA) bands due to polarons that peak at 0.35 eV and 1.2 eV, respectively, which are typical for polarons in PCPs [92,113] and copolymers [93]. Figure 3.8a also shows the ss-PA spectrum of a PDTP-DFBT/C_{71}-PCBM D-A blend that gives the maximum OPV efficiency in a cell device [94]. The ss-PA shows the two polaron PA bands at 0.3 and 1.25 eV, respectively, and a third PA band due to triplets (i.e. PA_T at 0.95 eV) that we identify from its MPA(*B*) response (Figure 3.2d). The occurrence of ss-PA_T in the D-A blend shows that a direct dissociation of independent triplets into e-h polaron pairs (PP) across the D-A interfaces is unlikely in this copolymer blend [114].

The ps PA(t) spectrum evolution in the D-A blend is shown in Figure 3.10b, which was measured at 1.55eV pump energy. At t=0, the PA(t) spectrum is similar to that in the pristine copolymer (Figure 3.3a) that contains the two primary PA bands, namely PA_{SE} and PA_{TT}. At t>0 the spectrum evolves, showing a red-shift of the low energy PA band and a blue-shift of the high energy PA band. We interpret the low energy PA red-shift as

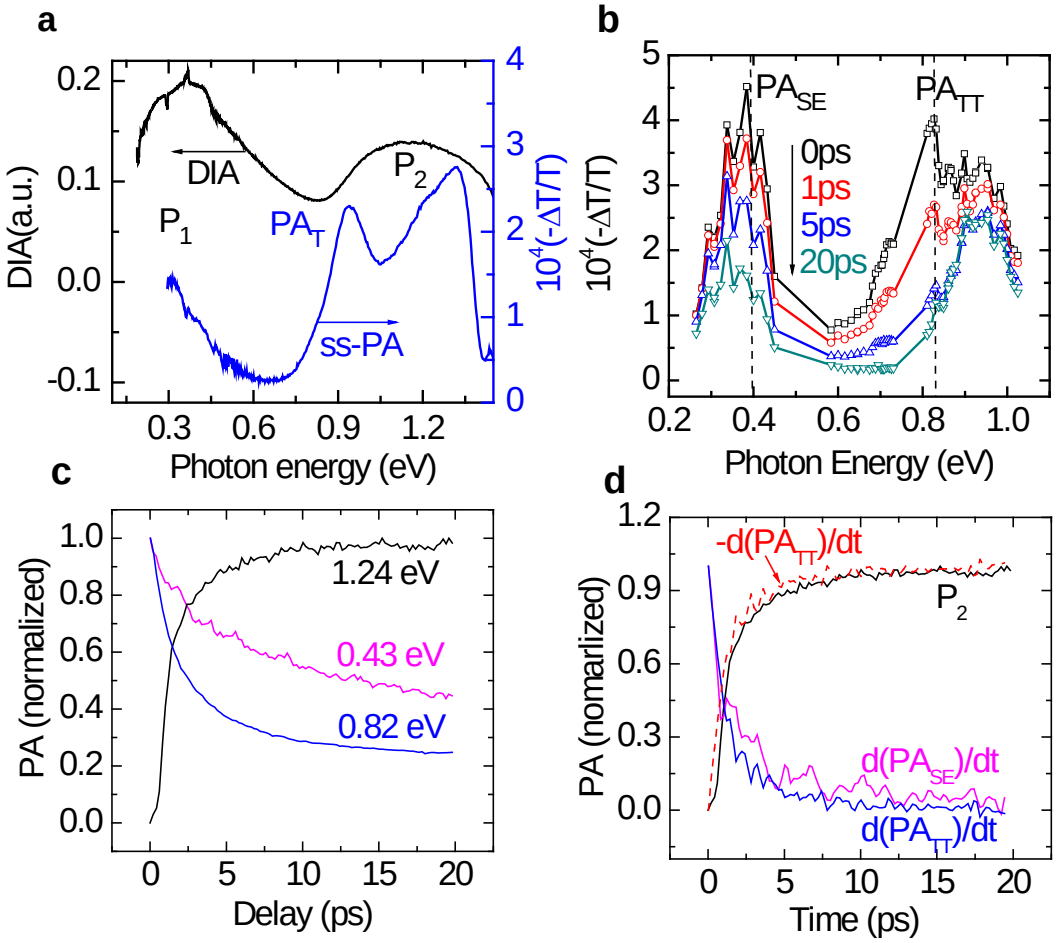

Figure 3.10: Steady state and ps transient PA spectroscopies of PDTP-DFBT/C_{71}-PCBM blend film up to 20 ps. (a) Doping-induced absorption (DIA) spectrum (black line) of pristine PDTP-DFBT, and steady state PA (ss-PA) spectrum (blue line) of the PDTP-DFBT/C_{71}-PCBM blend measured at 40K. The DIA and PA bands P_1 and P_2 of polarons in the copolymer chains, and the PA band of triplet (PA_T) are assigned. (b) The evolution of the t-PA spectrum of the blend excited at 1.55eV pump energy at various times as indicated, up to t=20 ps. The PA bands PA_{SE} and PA_{TT} are assigned for t=0; at t>0 these PA bands transform into P_1 (polarons) and PA_T (triplets), respectively. (c) The t-PA dynamics up to 20 ps measured at three different photon energies as indicated. (d) Comparison between the t-PA dynamics at 1.25 eV (P2; black line) and the time derivatives of the t-PA dynamics at PA_{SE} (purple line) and PA_{TT} (blue line). -d(PA_{TT})/dt dynamics (red broken line) is compared to P_2(t) dynamics (black line).

due to SE dissociation into PP at the D-A interfaces, namely $PA_{SE} \rightarrow P_1$ [92,115,116]. The SE dissociation dynamics are shown in Figure 3.10c at probe energy of 0.4 eV (at the PA_{SE} band). We note that the low energy PA(t) shows a fast decay into a plateau, because P_1 transition is close to that of PA_{SE} and the polarons are long-lived in the blend. Similarly, we interpret the blue-shift of the high energy PA band as dissociation of the TT pair into PP that follows the unique reaction:

$$TT \rightarrow PP_T + T, \tag{3.2}$$

where PP_T is a PP state in the triplet spin configuration. This reaction is spin-allowed, since the left- and right-hand sides of equation (3.2) both can have total spin S=0. Energetically, this reaction may be exothermic since the TT state lies above the $E(1^1B_u)$ (see Figure 3.2b), and both PP_T and T are located at mid-gap. The energy of PP_T state can be estimated from the emission spectrum of the singlet charge transfer CT state (or PP_S) in the blend film, adding that the PP_S is approximately close to the $E(PP_T)$. Figure 3.11a shows the PL spectra of pristine and blend films measured at ambient condition at 488nm excitation wavelength. The PL spectrum of blend films (black curve) shows: 1) the high energy band at 1.8eV which is due to the emission of $PC_{71}BM$, 2) two phonon sidebands 0-0 and 0-1 of PDTP-DFBT singlet exciton emission, respectively, that match well with the position of 0-0 and 0-1 emission peaks of pristine films (blue curve), and 3) a broad band below 1.2eV that is due to the emission of the PP_S. After subtracting the shoulder PL band of pristine films from that of blend films, the PP_S emission band is clearly emerged as shown in Figure 3.11b. The PL spectrum of singlet CT peaks around 0.95eV

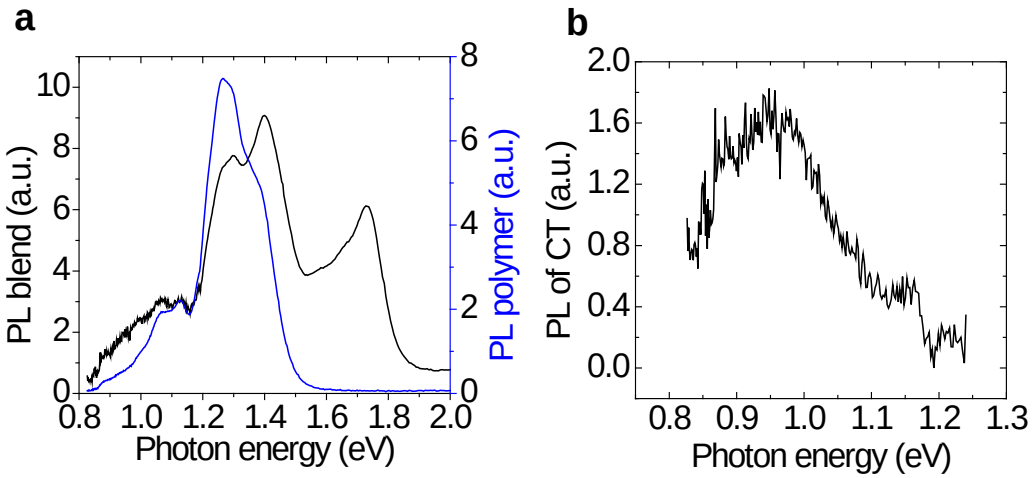

Figure 3.11: CT emission measurement (a) Photoluminescence spectra of PDTP-DFBT/PCBM films (black curve) and PDTP-DFBT pristine films measured at room temperature. (b) PL spectrum of PP_S or CT state in the blend, derived from the difference in the PL spectra of blend and pristine films at below 1.2 eV.

which is equivalent to the lowest energy of PP_S state. Noting that the energy of PP_T is within 0.1 eV of that of PP_S, we assign 0.9eV to $E(PP_T)$. For the reaction (3.1) to be allowed energetically, E(TT) should be at least equals to the sum of E(T) and $E(PP_T)$ which is ~ 1.73eV, 100meV higher than twice E(T), which is consistent with the previous report by Chan et al. [105].

Reaction (3.2) dynamics are also reflected in the high energy PA dynamics (Figure 3.10b); PA(t) comprises a fast decay into a plateau, similar to that of the lower energy PA band. However, in contrast to the lower energy PA, the plateau here is due to long-lived triplets that result from reaction (3.2), as identified in the ss-PA (Figure 3.10a).

In order to monitor the counterpart PP dynamics that are free of other PA(t) interferences, we note that the PP dynamics are obtained more easily at the P_2 band (~1.25 eV). To operate the mid-infrared laser system at this probe energy, we used a nonlinear crystal and optics (see section 2.2) for obtaining a weak probe beam at 1.25 eV,

as shown in Figure 3.10c. We note that the transient build-up of P_2 is too fast to be determined only by the PA_{SE} decay via the SE dissociation into PP. We thus conclude that another photoexcitation species is involved in the charge photogeneration process in the D-A blend, namely the TT pair. Since the TT dynamics contains a plateau at long time (Figure 3.10c), we calculated the time derivative of its decay function at 0.82 eV, namely $d(PA(t))/dt$ as seen in Figure 3.10d. As is clearly seen in Figure 3.10d, the polarity-changed dynamics, namely $-d(PA(t))/dt$, exactly matches $P_2(t)$ build-up. This is a strong indication that reaction (3.1) is operative here. As also seen in Figure 3.10d when calculating $d(PA(t))/dt$ of the lower PA band, it shows a slower dynamics compared to that of $P_2(t)$ build-up. This shows that reaction (3.1) is the main process that generates PP across the D-A interface in the PDTP-DFBT/PCBM blend. We therefore conclude that the TT pair ionization substantially contributes to the charge photogeneration efficiency in the blend.

We followed the ps transient PA_T dynamics in the D-A blend to a longer time. Figure 3.12a shows the t-PA spectrum evolution of the PDTP-DFBT/C_{71}-PCBM blend up to 1ns. As a reminder, there is a build-up of PA_T up to 20 ps as a result of TT dissociation at the D-A interfaces described by equation (3.1) (see Figure 3.10d). Surprisingly, PA_T continues to increase at t>20 ps reaching saturation at t~1ns (see Figure 3.12b). At the same time, $P_2(t)$ band decays with exactly the same dynamics to that of $PA_T(t)$ increase, but with opposite sense. This shows that the triplet exciton population in the copolymer chains increases at the expense of the PP density at the D-A interfaces, indicating that a "back reaction" occurs, where the PP at the D-A interfaces decay into triplets in the copolymer chains (i.e. $PP_T \rightarrow T$).

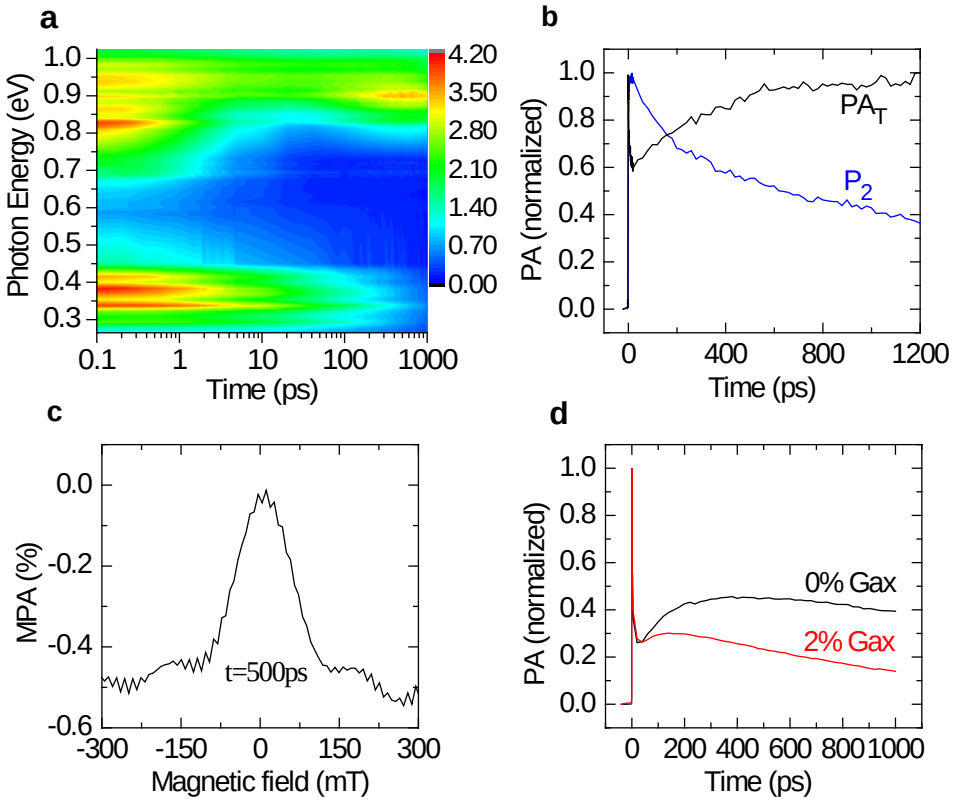

Figure 3.12: Picosecond transient spectroscopies of PDTP-DFBT/C_{71}-PCBM blend film up to 1.2 ns. (a) 2D presentation of the t-PA spectrum evolution with time, *t* excited at 1.55 eV, using false colors. (b) The t-PA dynamics measured at 1.25 eV (P_2; blue line) and 0.95 eV (PA_T; black line). (c) The t-MPA(*B*) response up to *B*=300 mT measured at *t* =500 ps. (d) Comparison of the t-PA_T dynamics of PDTP-DFBT/C_{71}-PCBM blend film with (black line) and without (red line) galvinoxyl (Gax) spin ½ radical additives, at a concentration of 2% weight.

The "back reaction" $PP_T \rightarrow T$ is actually a drawback that may lead to a decrease in the charge photogenerated efficiency of OPV cells. This can be ameliorated, however, by adding spin ½ galvinoxyl radicals into the blend [91,117,118]. Figure 3.12d shows the PA_T transient dynamics in two different D-A blend films, with and without galvinoxyl radical additives. It is clearly seen that the PA_T build-up is substantially reduced when galvinoxyl radicals are added to the blend. This may originate from the spin-spin interaction between the spin ½ radicals and the PP_T species at the D-A interfaces that

accelerates the $PP_T \rightarrow PP_S$ intersystem crossing, similar to that induced by the field. This supports our model dynamics and interpretation.

Figure 3.13 shows the t-PA spectra evolution of blend films when excited at 3.1eV. It is noteworthy that at high pump energy, we excited not only the donor copolymer but also the fullerene PCBM. The t-PA spectrum at t=0 shows an early appearance of two bands at 0.4eV and 0.82eV, which were assigned to the optical transitions of PA_{SE} and PA_{TT}, respectively. Within t=5ps, the TT band decayed in exchange of building up the P_1 and PA_T bands that peaks at 0.34eV and 0.95eV correspondently, which also follows the reaction (3.2). At longer time scale, the P_1 and PA_T bands continues developing up to 1ns; the latter exemplifies the back reaction of $PP_T \rightarrow T$ as observed previously when pumped at 1.55eV (Figure 3.11). However, the interesting buildup of P_1 band at later times contradicts the "back reaction" which should drain the polaron population, therefore depleting the P_1 band. The growth of P_1 band might be interpreted as the hole transfer from the lower HOMO of PCBM to the higher HOMO of the copolymer upon excitation of the PCBM, which would replenish the population lost due to the back reaction.

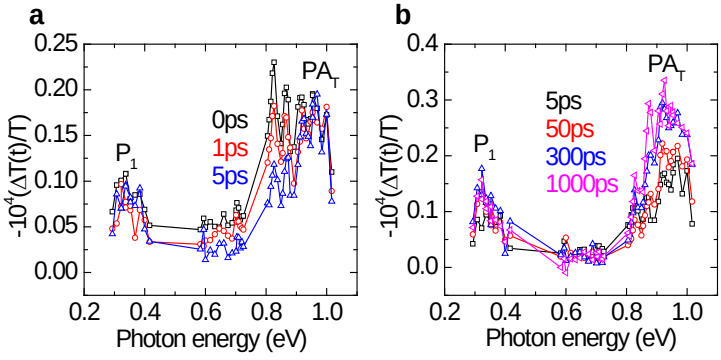

Figure 3.13: t-PA spectra of PDTP-DFBT/PCBM blend films measured at room temperature and its evolution up to 5ps (a), and 1ns (b).

3.4.2 Photophysics of PTB7/$PC_{71}BM$ Blend

Similarly, we now determine the role of TT pairs in the PTB7 solar cell device, in particular whether it can dissociate into electrons and holes at the D-A interfaces in the PTB7-doped C_{71} film which has an optimized ratio (1:2) for the maximum power conversion efficiency in solar cell devices. Before that, we first locate the signature of charge photoexcitations by measuring the DIA spectrum of the pristine PTB7 film doped with Iodine vapor (see the Materials section 3.2). The DIA spectrum (see Figure 3.8d) shows two broad bands peaking at 0.3eV and 1.1 eV which are equivalent to two optical transitions P_1 and P_2 of charge polarons. Figure 3.14a shows the ss-PA spectrum of a PTB7/$PC_{71}BM$ blend film. The spectrum peaks at 0.35eV and 1.1 eV which are similar to two polaron bands P_1 and P_2 from the DIA measurement. Since the triplet exciton band is also located at 1.1eV as indentified from the ss-MPA spectrum in the blend (see Figure 3.14b), which is the same as that in the pristine film, the 1.1eV peak would be a mixture of two PA bands, PA_T of triplets and P_2 of polarons, while the 0.35eV band is the lower P_1 transition.

Figure 3.14c depicts the transient PA(t) spectrum evolution in the D-A blend. At t=0ps, within 300fs system resolution, the spectrum is similar to that in the pristine film, consisting of two PA bands PA_{SE} at 0.4eV and PA_{TT} at 0.95eV. At t>0 the spectra evolutions show a blue-shift of the TT band towards the PA_T and P_2 bands, the TT band decays very fast within 20ps into a plateau in exchange for building up of the blue-shifted band which is beyond the limit of the highest probe photon energy of our transient MIR setup. However, we interpret the blue-shift of the TT band as the dissociation of TT pair into polaron pairs, PPs, resulting in either (1) two PP_Ts (polaron pair in triplet

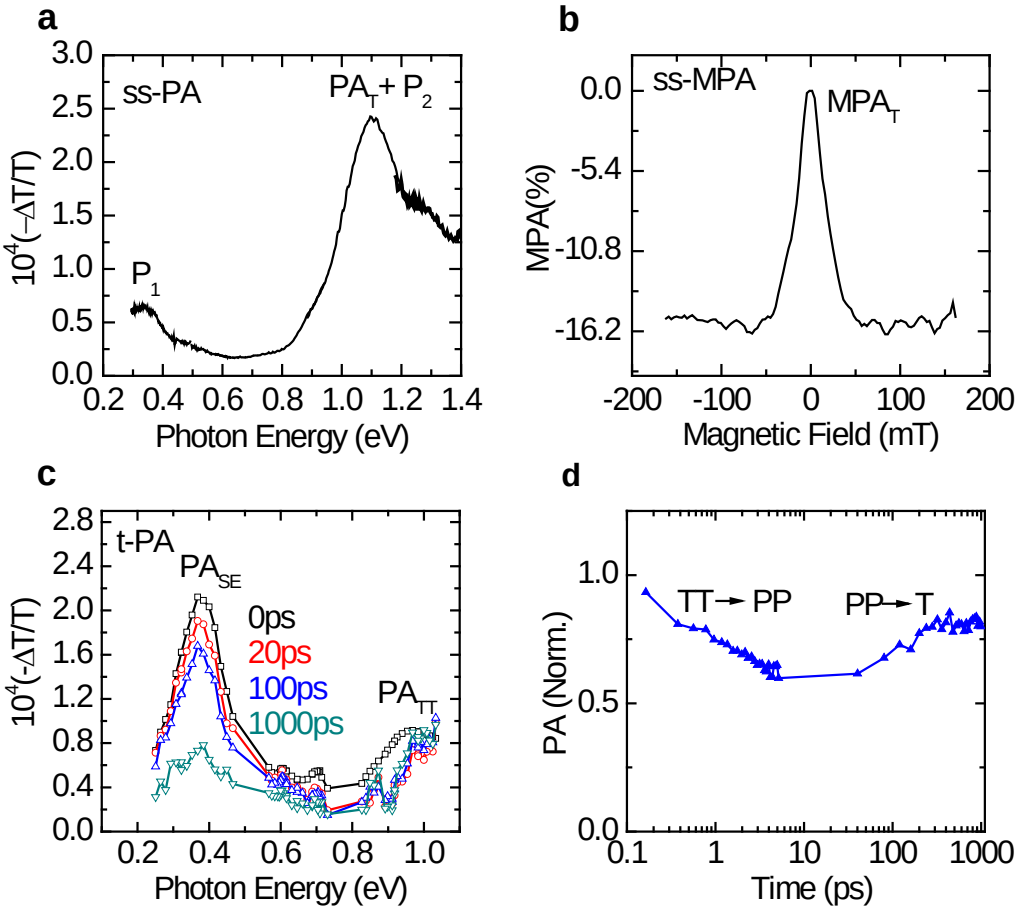

Figure 3.14: PA spectra of PTB7/$PC_{71}BM$ blend (a) Steady state PA of PTB7/$PC_{71}BM$ blend films measured at 40K. (b)The ss-MPA response of 1.1eV band shows a triplet pattern, signaling the triplet excitons is stable in this blend. (c) Transient PA spectrum of the blend film up to 1ns shows a blue-shift of triplet pair band into triplet exciton and P_2 bands at 1.1eV. (d) Dynamics of 1eV probe's band up to 1ns. The first 20ps shows triplet pairs might dissociate into triplet polaron pairs which later recombine back to triplet excitons on the copolymer chains in the time regime from 20ps to 1ns.

configuration) or (2) one PP_T leaving behind one triplet [105], conforming to the spin conserved process since the total spin in both cases is zero, S=0. Unfortunately, the spectral overlaps at 1.1eV high energy band between PA_T and P_2; and low energy band at 0.4eV between PA_{SE} and P_1 complicate our effort to further determine which reaction would dominate the TT dissociation. Our interpretation of the TT pair dissociation is further supported by observing more build-up of the blue-shifted band at a later time

(Figure 3.14d), showing the increasing of dynamics taken at 1eV probe right after the first 20ps up to 1ns, which would be due to the geminate recombination of triplet polaron pairs back to triplet excitons on the copolymer chains. If the optical cross section of triplets are larger than that of PP, our reasoning for the geminate recombination of PP → T should be justified. In addition the build-up at 1eV probe's dynamics after 20ps in Figure 3.14d is also an indirect proof for dissociation of the TT pair which is more likely to take place rather than the singlet dissociation which results in the PPs in singlet configuration and the recombination of singlet PP at a later time in picosecond time scale should show the dynamics decay with time.

3.5 Conclusion

Photophysics of pristine copolymers embedded in polystyrene matrix revealed the magnificent intrachain singlet fission in which the lowest energy of the excited state of singlet excitons is approximately twice as that of triplet excitons, which calls for high singlet fission yields. The triplet pair, a new species composed of two correlated triplet excitons, is formed instantaneously within 350fs, the time resolution of our femtosecond experimental setup, right after the formation of the singlet exciton. Surprisingly, in the copolymers/ $PC_{71}BM$ fullerene blend film, the triplet pair dissociates at the donor and acceptor interfaces into one triplet polaron pair PP_T, therefore leaving behind one triplet exciton on the copolymer chains. The ionization of triplet pairs is a unique and spin allowed process which occurs as fast as and lasts for ~ 20ps. The PP_T which is a product of the TT ionization reaction later recombines back into the triplet exciton observed up to 1ns. The "back reaction" is in fact another significantly lost mechanism for charge

photogeneration in the BHJ solar cell device. Finally, we demonstrated that the spin ½ additives can help prevent the "back reaction" lost channel by accelerating the $PP_T \rightarrow PP_S$ intersystem crossing process.

CHAPTER 4

TRANSIENT MAGNETO-PHOTOINDUCED ABSORPTION STUDIES OF SINGLET FISSION IN COPOLYMERS

4.1 Introduction

In Chapter 3, we have shown the existence of the intrachain singlet fission SF in the isolated chains of pristine copolymers. Our hypothesis about the SF was mainly based on the observation of a new band peaked at 0.82eV in the t-PA spectrum (Figures 3.3 and 3.7) which does belong to neither the singlet exciton, nor the triplet. Therefore, we assigned it to an optical transition of the triplet pair, which is a quantum state of two coherent triplets formed through the singlet fission. There was no other direct evidence to show that the assumed triplet pair is actually neither a lower energy $2\ ^1Ag$ state (see Chapter 1, excited state ordering), nor a CT state that might exist in these D-A copolymers. If they were ever observed as the 0.82eV band, both $2\ ^1Ag$ and CT states would have been formed initially in the spin singlet which is immune to the magnetic field effect. In this chapter, we prove that the 0.82eV band is indeed the absorption of triplet pair using a new technique, dubbed transient magneto-photoinduced absorption or t-MPA.

4.2 t-MPA Studies of Pristine Films

4.2.1 PDTP-DFBT Pristine Films

We found that the bands PA_{SE} and PA_{TT} are in 'dynamic equilibrium' with each other. As seen in Figures 4.1a and 1b, there is a substantial t-MPA(*B*) response for both PA bands, starting from few picoseconds. This shows that the spin degree of freedom is involved in the underlying photoexcitations; therefore, they cannot be simply due to SE alone, which has total spin S=0. In contrast, the TT state is expected to be in dynamic equilibrium with two separated triplet excitons, even if the actual efficiency of the SF may be small [119]. Consequently, PA_{TT} involves some S≠0 components, which is the only explanation possible for the high energy t-MPA(*B*). We also note that t-MPA_{SE}(*B*) response decreases with *B*, whereas t-MPA_{TT}(*B*) increases with *B* (Figure 4.1a). Furthermore, the two t-MPA responses increase with time in the same way, reaching saturation at t_0~200 ps (Figure 4.1b). Taken together, these observations have an unambiguous explanation, namely, the SE and TT states are in 'dynamic equilibrium', whereby the photoexcitation population goes back and forth between them. This is the process by which MPA_{SE}, which should have been null (since S=0), gets its strength from MPA_{TT}. As a control experiment, we verified that PA_{SE} in a traditional PCP such as DOO-PPV lacks t-MPA response (Figure 4.2). Moreover, from the relatively slow evolution of the t-MPA with time for both PA bands, we conclude that SE and TT species coherently interact until ~t_0; otherwise MPA would be observed within the first 300 fs. We may thus obtain the spin exchange coupling, $J_{SE\text{-}TT}$, between the SE and TT pair from t_0. Using the time-energy uncertainty principle, we get from t_0 that $J_{SE\text{-}TT}$≈30 mT, which is a much larger interaction than the hyperfine in PCPs (~3 mT) [77,120]. This shows that

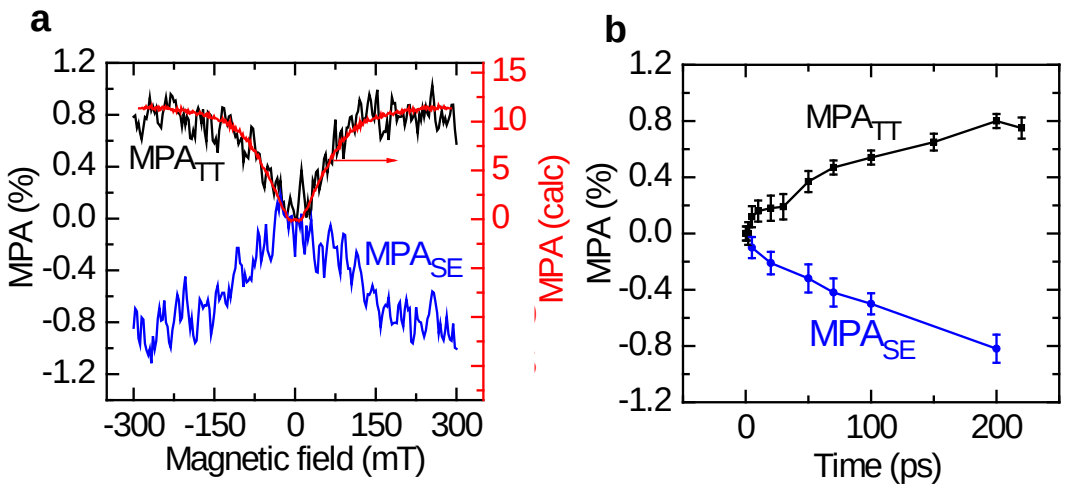

Figure 4.1: Picosecond t-MPA responses (a) The transient MPA (t-MPA(*B*)) response of PA_{SE} (blue line) and PA_{TT} (black line) measured at *t*=200 ps up to *B*=300 mT. The red line through the data points of the t-PA_{TT}(*B*) response is a fit using a model based on transient singlet-fission (see Appendix). (b) The evolution of the t-MPA(*B*=300 mT) for PA_{SE} (blue) and PA_{TT} (black) up to *t*=200 ps.

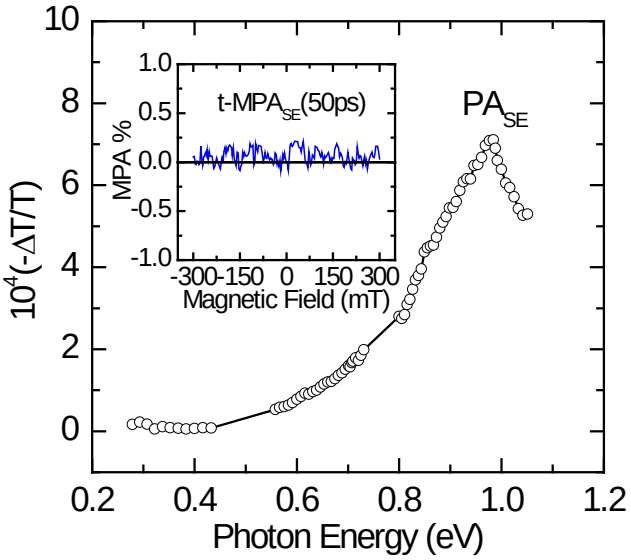

Figure 4.2: The mid-IR t-PA spectrum of DOO-PPV polymer film at '*t*=0' measured at 3.1 eV pump excitation. The PA from singlet exciton (PA_{SE}) is assigned. We note that there is only one PA band in this traditional PCP homo-polymer, in contrast to PDTP-DFBT copolymer that shows two PA bands (see Figure 3.3). The inset shows the t-MPA(B) response measured at *t*=50 ps. The null result here is in sharp contrast with the t-MPA in pristine PDTP-DFBT discussed in the text.

the spin lattice relaxation time among the nine spin states in the TT species is much longer than the interaction time with the SE, justifying the following model for calculating the t-MPA(*B*) response. It is noteworthy that t-MPA(*B*) and ss-MPA(*B*) responses are *different* from each other (Figures 4.1a and 3.2d, respectively). This shows that the two triplets in the TT pair at early time are spin-entangled, and thus do not behave as two independent species as in ss condition.

Interestingly, the observed t-MPA(*B*) response in the sub-ns time domain (Figures 4.1a) which is due to SF is quite different from magnetic-field responses that are typical of the SF process, which have been used in the literature to identify the SF process [112,121,122]. This is due to the finite time evolution of the t-MPA(*B*) that originates from the magnetic field manipulation of the nine TT spin sublevels, as follows (see Appendix). We assume that the TT pair is held together by a small exchange interaction (X<<*D*), and write the TT spin Hamiltonian in a magnetic field as,

$$H_{TT} = \sum_{j=1}^{2} [g_j \mu_B \vec{S}_j \cdot \vec{B} + \vec{S}_j \cdot \tilde{\tau}_j \cdot \vec{S}_j] + \mathrm{X}\vec{\mathrm{S}}_1 \cdot \vec{\mathrm{S}}_2 \quad , \tag{4.1}$$

where g_j is the g-factor of each triplet S_j=1, $\boldsymbol{B}$ is the magnetic field, μ_B is Bohr magneton, and $\boldsymbol{\tau}$ is a symmetric traceless tensor of rank 2, which is uniquely determined by the ZFS parameters, as well as its space orientation with respect to $\boldsymbol{B}$. At *B*=0, three of the nine TT spin levels have a singlet character [119,123]. However, when *B* increases, then the distribution of singlet character among the nine Zeeman split spin sublevels changes (Figure 4.3), leading to variations in the initially populated levels by the internal

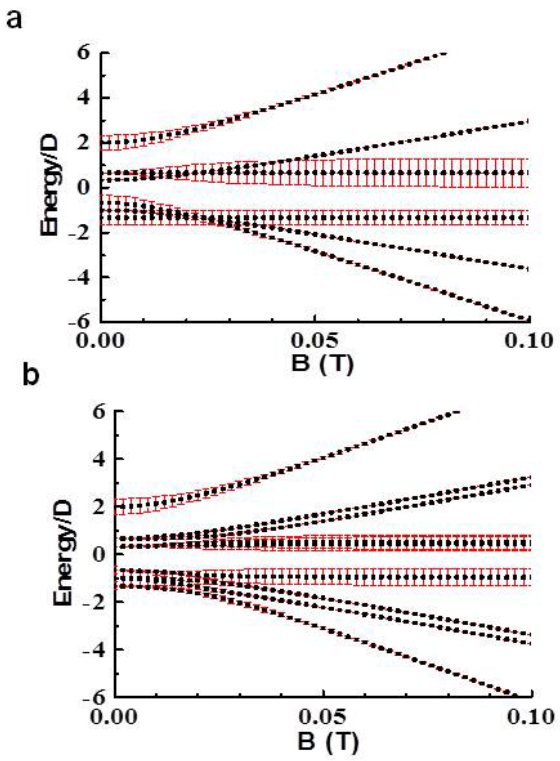

Figure 4.3: The calculated energies of the nine spin sublevels of a TT pair and their singlet content, as a function of magnetic field for two field orientations. The calculation method is described in the Appendix. (a) The TT angle β=0; where β is the angle between *B* orientation and the triplet #1; the angle, θ between the two triplets in the TT pair is θ=0. (b) β=0.55π; θ=0.15π. The size of the y-bar (red color) for each line indicates the relative singlet content of the level. The ZFS parameters for both triplets are *D*=38mT, *E*=15 mT; and the exchange interaction is X=0.

conversion SE→TT process [119]. As time progresses and with spin-dependent lifetime for the nine TT spin sublevels that is faster than the spin-lattice relaxation time, the total population of the TT pair becomes magnetic field-dependent, rendering a field-dependent photoexcitations density related to PA, namely MPA(*B*) (Figure 4.4). There are two important angles that should be taken into account for fitting the experimental t-MPA results. One angle, θ, is between the spin direction of the two individual triplets in the TT pair; and the other angle, β, is between the spin direction of one of the triplets and $\boldsymbol{B}$

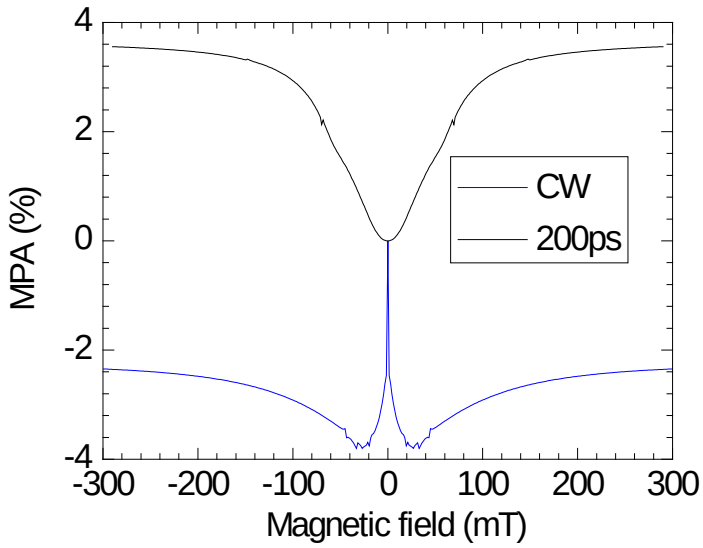

Figure 4.4: Time-resolved (t-MPA(*B*)) and steady state (ss-MPA(*B*)) responses of singlet fission-born TT pair. *Bottom panel*: ss-MPA(*B*) using the parameters D=35 mT, E=10 mT, X=0.05 mT, k~10^{10} s^{-1}. *Top panel*: transient MPA(*B*) response at *t*=200 ps, using the parameters D=60 mT, E=0.01mT, X=0.01 mT, k~10^{10} s^{-1}. The calculations for both MPA(*B*) responses were done with full powder pattern, in which *B* angle, β and TT angle, θ are averaged; and long spin-lattice relaxation time is assumed. Note the sharp contrast between the two MPA(*B*) responses.

direction. To fit the t-MPA(*B*) response, we averaged the t-MPA(θ,β) over all possible angles in order to get a 'powder pattern' suitable for MPA(*B*) (see Appendix for the model for t-MPA(B)). The excellent fit seen in Figure 4.1a upper panel for $t=t_0$=200 ps was obtained using *D*=60 mT, while taking into account the limited time evolution of the nine TT spin states. We note that the *D* parameter here is larger than that by which the ss-MPA is fitted; this may be caused by a shorter triplet wavefunction extent (and thus larger ZFS parameter [99]) for the individual triplets within the TT pair state.

Figure 4.5 shows the evolution of the t-MPA in the microsecond time domain (see chapter 2, section 2.3). Figure 4.5a shows that the PA decay at 0.9 eV (where both PA_{TT} and PA_T contribute) is strongly magnetic field-dependent. From the change, ΔPA(t) in

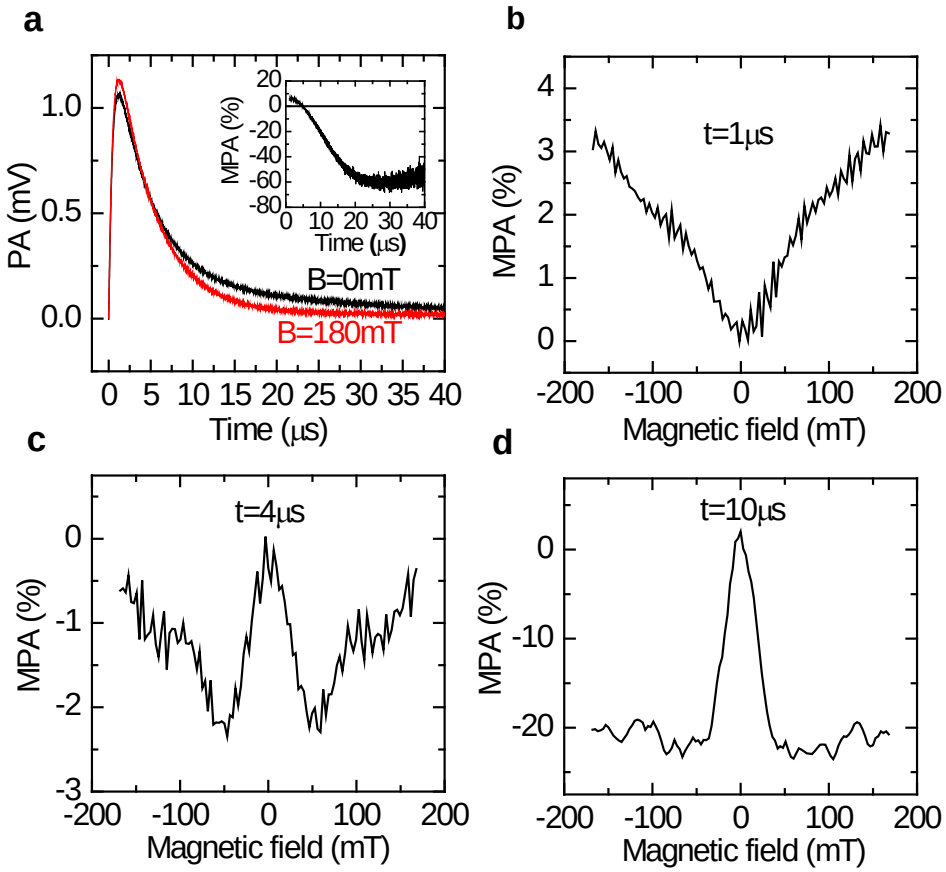

Figure 4.5: Microsecond transient spectroscopies of pristine PDTP-DFBT film measured at 0.9 eV and 80K. (a) The PA decays measured at magnetic field B=0 (black line) and B=180 mT (red line) up to t=40 μsec. The inset shows the calculated t-MPA at B=180 mT up to 40 μsec. (b) to (d) The transient MPA(B) response up to B=180 mT measured at different times, t as indicated.

PA(t) with B, we obtain the t-MPA(B,t) response and study its time evolution. Figure 4.5a inset shows that t-MPA at B=180 mT changes polarity at ~4 μsec. This is reflected in the t-MPA(B) response (Figure 4.5b-d), which dramatically changes from t=1 μsec to t=10 μsec. t-MPA(B) response changes from an early time lineshape that is similar to that measured in the ps time domain due to SE-TT interaction (Figure 4.1a), to a longer time lineshape similar to that of individual, uncorrelated triplets as in ss-MPA (Figure 3.2d). We therefore interpret this surprising t-MPA(B) evolution as decomposition of the TT

pair (where the two triplets are spin-entangled) into two separated triplets having uncorrelated spins. This enlightening experimental result is the strongest evidence for the SF process in PDTP-DFBT that supports our interpretation.

4.2.2 PTB7 Pristine Films

Similar to the PDTP-DFBT pristine, the t-MPA spectrum (Figure 4.6) measured at 200ps time delay on the singlet exciton band of PTB7 pristine, namely t-MPA_{SE}, and the 0.95eV HE peak, t-MPA_{HE} (Figure 3.7a), shows a correlation; the t-MPA_{HE} increases with magnetic field in expense of the decrease of t-MPA_{SE}. Since a singlet exciton is not a composite S=0 species such as polaron pair singlet PP_S, we expect the t-MPA_{SE} to be null. Therefore, the observed t-MPA_{SE} should get its strength indirectly from the t-MPA_{HE} through the closed-loop process where the SE populates the HE band species through the singlet fission and the HE species gives its feedback to the SE through the fusion reaction; the whole process eventually establishes the dynamics equilibrium between SE and HE states. To make the whole thing work, the t-MPA_{HE} spectrum has to be involved directly in its own spin degree of freedom. From all above evidence, we can assign the HE band as an optical transition in the TT manifold, namely PA_{TT}.

Interestingly the two t-MPA responses (Figure 4.6b) progress with time in the same way, increasing with B field and approaching a saturation at t_0 ~ 200ps, which shows that the SE and TT coherently interact until ~ t_0. Using the uncertainty principle, we can estimate from t_0~ 200ps the coupling strength $J_{SE\text{-}TT}$ ~30mT between the two species, which is much larger than the typical hyperfine coupling constant in PCP, about ~ 3mT. It means that the interaction time between the SE and nine spin states in the TT species is

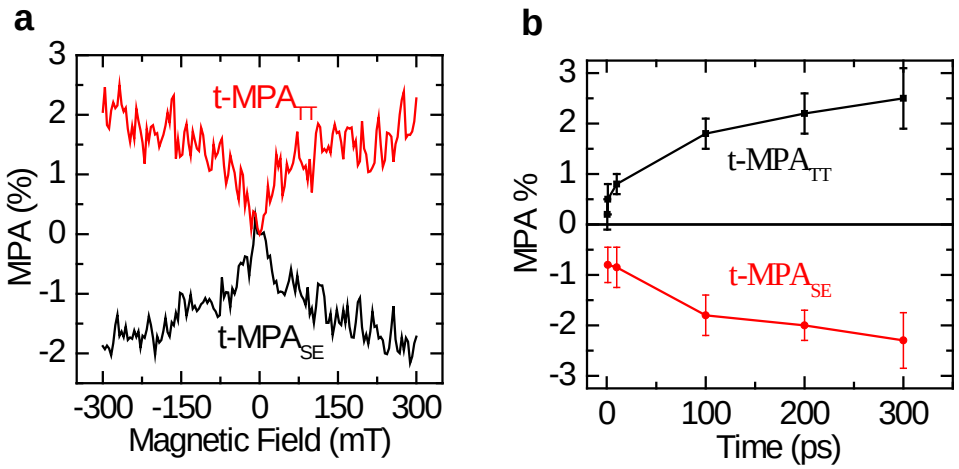

Figure 4.6: Pristine PTB7 in PS (a) The transient MPA (t-MPA(*B*)) response of PA_{SE} (blue line) and PA_{TT} (black line) measured at *t*=200 ps up to *B*=300 mT. (b) The evolution of the t-MPA(*B*=300 mT) for PA_{SE} (blue) and PA_{TT} (black) up to *t*=300 ps.

much shorter than the spin lattice relaxation time constant, justifying the model for calculating the t-MPA(B) response (see Appendix) that was used to fit the t-MPA response of the TT band of the PDTP-DFBT pristine (see Figure 4.1a).

The fact that two triplets in the TT pair are spin-entangled and do not behave like independent triplets was revealed by the t-MPA response; the t-MPA_{TT} spectrum is very different from the ss-MPA_T (Figure 3.6). The t-MPA_{TT} response in the picosecond time domain can generally be explained due to the magnetic field manipulation of nine TT spin states. At B=0, three of the nine TT spin states have the singlet character. The applied B field splits the TT pair into nine spin sublevels, redistributing the singlet character among the nine states, leading to variations in the initially populated nine levels through the singlet fission process. As time progresses and with different spin-dependent decay rates for the nine TT sublevels which are faster than the spin lattice relaxation time, the total population of the TT pair becomes magnetic field-dependent.

It is interesting to follow the t-MPA_{TT} responses in longer time scale to see when the

TT pair dissociates into two uncorrelated triplets. For that purpose, we measured the magnetic field dependence PA(t) at 0.95eV probe using the microsecond to millisecond PA setup described in Chapter 2, section 2.3. Figure 4.7 shows the t-PA dynamics at 0.95eV with two different magnetic field strengths. It is clear to see the PA(t) is field-dependent; at time t<5μs, the PA(t) at B=180mT is larger than that at B=0mT; but at longer time, it becomes smaller. To check the spectral evolution of t-MPA(B), we measured it at different delay times (Figure 4.7b to d). Obviously, the spectral shape at t = 2us is similar to that of TT pair in the picosecond time range (Figure 4.6a). However, at t=6us, we start to see a narrow component emerge, which then dominates the t-MPA response at t> 20us. In fact the t-MPA(t>20us) spectrum is the same as the ss-MPA_T that characterizes independent triplets, measured at the PA_T band (Figure 3.6). We therefore conclude that the TT pair disintegrates into two independent triplets in the microsecond time range; confirming our identification of the TT pair and the SF process in the PTB7 copolymer.

Surprisingly, the microsecond t-MPA spectrum of pristine films measured at 0.95eV probe continues to evolve at much longer delay time until ~1ms, which shows that the FWHM of narrow features decreases over time and disappears after 900μs (Figure 4.7e-h). The underlying mechanism for this spectral narrowing is still unknown, given that uncorrelated triplet excitons are the only long-lived species surviving in this time regime (>20 microseconds) and the ZFS parameters D and E do not depend on the population density of triplets.

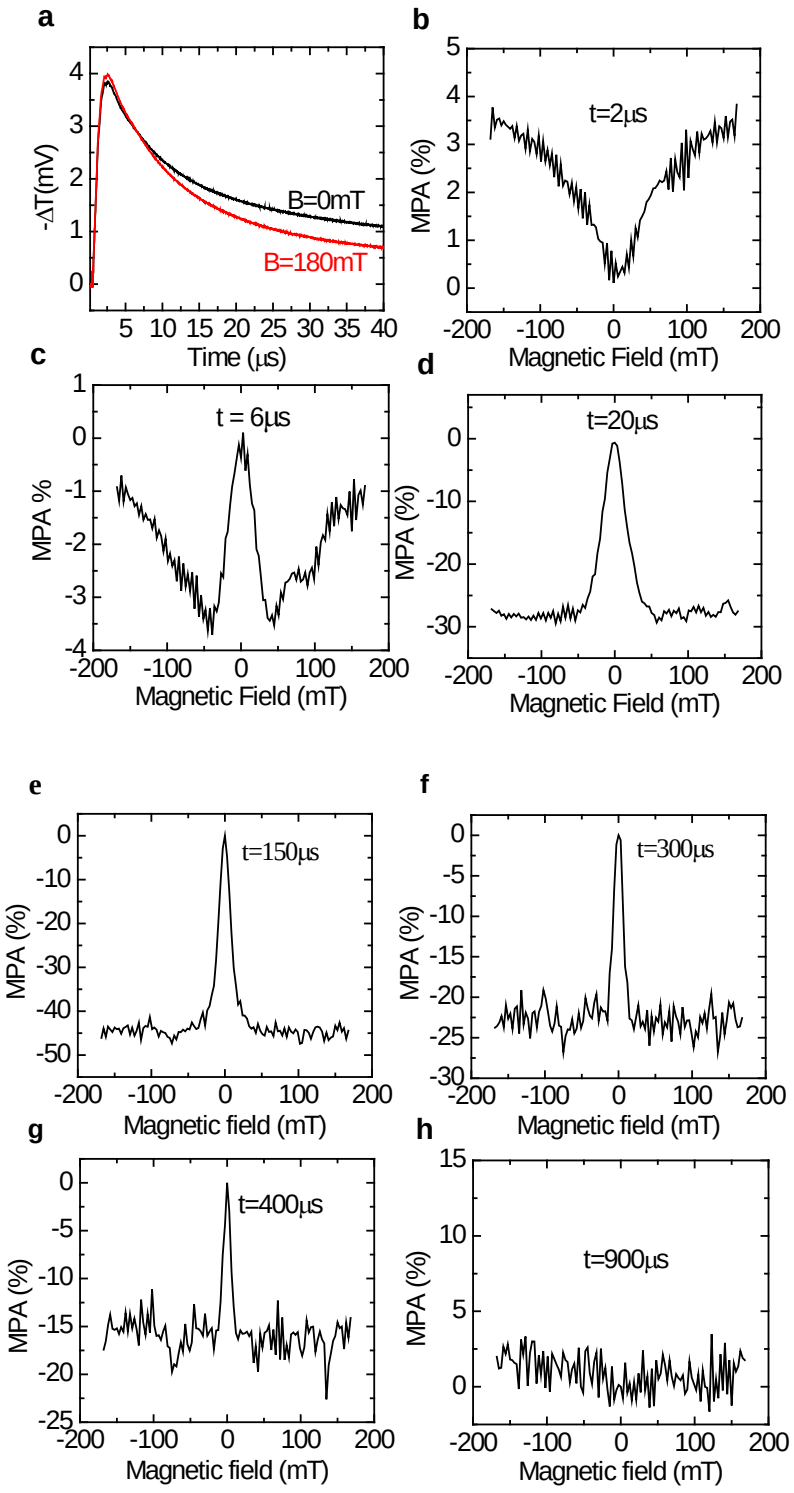

Figure 4.7: Microsecond transient spectroscopies of pristine PTB7 film measured at 0.95 eV and 80K. (a) The PA decays measured at magnetic field *B*=0 (black line) and *B*=180 mT (red line) up to *t*=40 μsec. (b) to (h) The transient MPA(*B*) response up to *B*=180 mT measured at different times, *t* as indicated.

4.3 t-MPA Studies of PDTP-DFBT/PCBM Blend

In Chapter 3, we reported that the PP_T recombines back to triplet excitons on the copolymer chains up to 1ns, which shows that the decay of the P_2 dynamics in fact matches with the build-up of the PA_T band (Figure 3.8d). Apart from the observed dynamics correlation, the following t-MPA responses measured on the triplet band further support the "back reaction" $PP_T \rightarrow P_T$.

Figure 4.8a shows the dynamics of PA_T taken at two different B fields, B=0 (black) and B=300mT (red) up to 4ns, and Figure 4.8b indicates a fractional change of t-PA_T with B field according to the formula of t-MPA(t,B) = (t-PA(B) – t-PA(B=0mT)/t-PA(B=0mT) with B=300mT. The t-MPA(t,B=300mT) shows a distinct half bow shape which changes the polarity from negative to positive with the zero crossing point at ~1ns, and approaches a saturation at ~4ns. We also measured the t-MPA(*B*) responses of PA_T at different delay times (Figure 4.8c-d), focusing on the t-MPA(B) at t=500ps, during which the "back reaction" occurs, and the t-MPA(B) at t > 1ns that have the positive responses. The negative t-MPA(*B*) response measured at *t*=500 ps is broad and unsaturated up to 300 mT. We estimate the FWHM of t-MPA response in this field interval ~110 mT, which is narrower than that of t-MPA response of TT pair in the pristine film measured at t=200 ps (Figure 4.1a) ~150 mT. Also the t-MPA in the blend has opposite polarity from that in the pristine film. We thus conclude that the t-MPA response of PA_T in the blend originates from spin-mixing process other than that measured in the pristine copolymer. The spin-mixing in the blend occurs between PP_T and PP_S (i.e. intersystem crossing) at the D-A interfaces, mediated by the difference in the *g*-factor of electron and hole polarons (so-called 'Δg mechanism [77,124,125]). The conversion of the initially

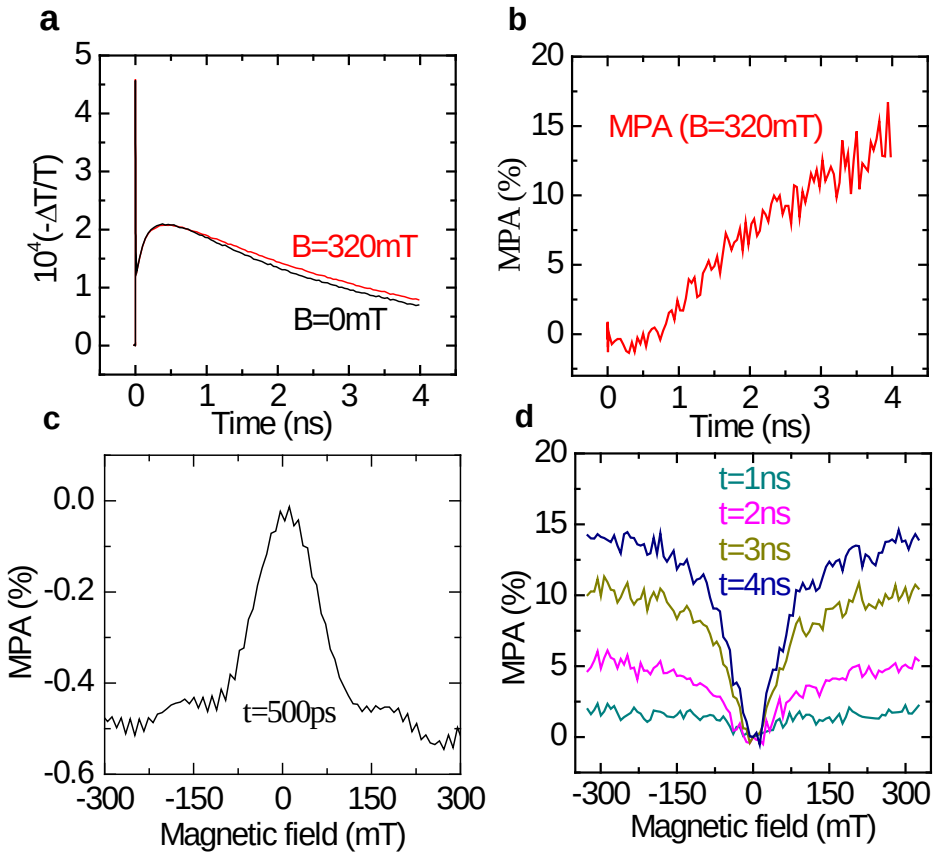

Figure 4.8: Sub-nanosecond transient spectroscopies of PDTP-DFBT/PCBM blend films measured at 0.82 eV at room temperature. (a) The PA decays measured at magnetic field B=0 (black line) and B=300 mT (red line) up to t=4 ns. (b) The calculated t-MPA at B=180 mT up to 40 ns. (c) to (d) The transient MPA(B) response up to B=300 mT measured at different times, t as indicated.

populated PP_T (see equation (3.1)) into PP_S that increases upon the application of the magnetic field reduces the population of PP_T available for the "back reaction" and this, in turn, decreases PA_T, in agreement with the reverse polarity of the obtained t-MPA(B) response (Figure 4.8b). The positive t-MPA responses at times t>1ns, which are also broad and nonsaturated up to 300mT, have the FWHW of ~110mT that is similar to that of t-MPA at 500ps, indicating that they come from the same spin-mixing mechanism between PP_T and PP_S but in a reversed order with the initially dominant populated singlet

PP_S. The majority of PP_S population left over after 1ns is a product of the previous conversion cycle from $PP_T \rightarrow PP_S$. The conversion from $PP_S \rightarrow PP_T$ upon applied magnetic field in this time domain would increase the PP_T population available for the "back reaction", which subsequently increases the triplet population and PA_T, in agreement with the positive responses of t-MPA(B) measured at PA_T.

4.4 Conclusion

We introduced a new method, dubbed transient-magneto photoinduced absorption t-MPA from sub-nanosecond to millisecond time domain, to elucidate the singlet fission in low bandgap copolymers. Using this novel technique in combination with the t-PA spectroscopies, we detected in the pristine copolymers a dynamic equilibrium between the SE and TT that was held by their spin exchange interaction with the interaction strength as large as ~30mT at early time, and the TT splitting into separated triplet excitons at later times. Using this tool in the copolymers/fullerene blend, we also identify the charge carrier loss mechanism by the "back reaction" of PP into triplet excitons on the copolymer chains.

CHAPTER 5

SUMMARY AND FUTURE RESEARCH OUTLOOK

We have used various optical spectroscopies to thoroughly study a new class of OPV materials, namely the low bandgap π-conjugated polymers. These copolymers exhibit the intrachain singlet fission SF which has never been reported previously because of the lack of spectroscopic tools which can probe in the MIR spectral range. With our unique capability for doing pump/probe in the MIR probe range couple with the new nanosecond to millisecond PA spectroscopies and the transient magneto-photoinduced absorption, we have discovered the singlet fission and various dissociation mechanisms of TT state in the pristine copolymers and their blend with $PC_{71}BM$ fullerene. The 'smoking gun' proof for the TT photogeneration and its dissociation mechanisms is provided by the novel technique of t-MPA(*B*) response.

In addition, the t-MPA may be applied for studying spin dynamics in OSEC having fast triplet generation other than LBG copolymers. One example is SF that occurs at high excitation photon energies in regular polymers, where the photon energy is larger than that of twice the triplet lowest energy. Yet another example is the ultrafast intersystem crossing that occurs in Pt-polymers; this process was measured to be in the ps time domain. It can also be measured in the time domain of nanoseconds to millisecond, which does not require ps pump-probe correlation. We note that the t-MPA(*B*) response in

this time interval may be very different from that in the ps time domain since the processes that lead to MPA may be different.

Together with t-MPA, the transient magneto-photoluminescence (t-MPL) can be used to study the process of reversed intersystem crossing, including the thermal activated delay fluorescence and triplet-triplet up conversion. These processes have attracted significant research efforts for increasing the OLED efficiency by harvesting more triplets. These processes occur in the nanosecond to microsecond time range and thus would be ideal for transient t-MPA and t-MPL in that time interval.

Amid potential applications in OPVs, the ultrafast spin-conserved singlet fission has attracted many researchers working in the field of device physics, optical spectroscopy, and chemical synthesis. The spectroscopic study has demonstrated the possibility of harvesting triplet excitons from SF in pentacene onto PbSe nanocrystals through the resonant energy transfer [126]. On the other hand, there would be another advance that may have shown the triplet transfer from a low bandgap copolymer, which is known as the strong intrachain SF from our study, to amorphous Si at their interfaces in a bi-layer solar cell device structure. According to his 2015 APS meeting talk, Prf. Yang Yang has mentioned the bi-layer cell of a-Si and a copolymer with a PCE of 10.5% which is much higher than that of individual cells: 6% in the a-Si and 8% in the copolymer. This achievement may not be a breakthrough when comparing with the tandem or perovskite cells which already obtained more 15% in average. However, it may have demonstrated the capability of extracting more charges from triplets or triplet pairs in the copolymer chains onto the a-Si which may have its optical gap in resonance with the triplet energy in the copolymer. There are two possibilities to explain for 6% + 8% = 10.5% , either

increasing the short circuit current I_{sc} or open circuit voltage V_{oc}. Increasing V_{oc} in a tandem cell has explained its higher PCE, but not with the bi-layer structure. We speculate that in this bi-layer cell, the SF in the copolymer would add an extra amount of photocurrents that may be generated from triplet excitons or triplet pairs dissociated at the copolymer and a-Si interfaces.

From the spectroscopic point of view, the SF is rich and interesting research subject to be explored, given that there is still a debate about its origin which involves either electronic or vibronic couplings between SE and TT states. Apart from the energetic constraint which requires the energy of singlet excitons twice as that of triplets, a strong electronic interaction between the TT and SE has been considered as a main driving force for efficient SF yield [105]. In fact, our experimental results in the copolymers have shown the coupling strength of ~30mT, in agreement with the previous reports. However recent studies on pentacene polycrystalline and its derivatives using three pulses technique and broadband 2DES [127] indicated that “overlap and mixing of the vibronic manifolds of singlet exciton and TT state play a key role in ultrafast dynamics of SF”, disagreeing with the previous claims [105].

On the other side of molecular design, understanding the root of SF would help effectively design and synthesize efficient SF materials that can be used in the BHJ solar cell structure, taking advantage of its easy and cost-effective fabrication process. Harvesting charges from triplet excitons or even directly from triplet pairs which were formed through the SF is crucial for boosting the power conversion efficiency (PCE) beyond the Shockley-Queisser limit. Therefore, we notice that the next adventure in OPV field would be to design dimers serving as good SF materials from acenes, known as

having strong SF in polycrystalline phase, and D-A polymers with different D and A molecules that can be used as electron donors as well as triplet sensitizers in the effective BHJ cells. As a final remark, the field of organic solar cells already approached 10% of PCE in a single cell OPV with new low bandgap copolymers [87].The future of OPVs with a higher PCE targeting beyond 10% in single cells would be achievable with singlet fission, but would need a balancing between the research triangle, which is molecular designs /syntheses, device fabrication techniques, and spectroscopic studies.

APPENDIX A

CALCULATION METHODS FOR THE t- MPA(B) AND ss-MPA(B) RESPONSES

We used different methods for calculating the t-MPA(B) and ss-MPA(B) response, respectively. The ss-MPA(*B*) calculation method is for an isolated triplet that gives a PA band, namely PA_T, whereas the calculation of t-MPA(B) response is based on singlet fission of the SE into TT pair state.

A.1 t-MPA(*B*) Response Related To SF

We used a simple model for explaining the magnetic field response appropriate for a singlet fission (SF) process following photo-excitation. The model is a follow-up of our earlier studies [77,128].

As described in the text, the SF process creates a triplet-triplet (TT) pair initially in an overall singlet state, $S_{TT}=0$. SF occurs within ~0.1 ps after photoexcitation and the $S_{TT}=0$ state is maintained for times, $t<\tau_{SL}$, where τ_{SL} is the spin lattice relaxation time in the copolymer. Both transient-MPA (in the time interval 1ps-200ps) and steady state MPA are therefore described here within the TT pair system having spin $S_{TT}=0$.

The general form of a triplet exciton Hamiltonian may be written as [129]

$$H_T = \vec{S}_T \cdot \tilde{\tau} \cdot \vec{S}_T \ , \qquad \text{(A.1)}$$

where S_T=1 is the triplet exciton spin and $\tilde{\tau}$ is a symmetric traceless tensor of rank 2. The tensor $\tilde{\tau}$ is uniquely determined by the characteristic zero field splitting (ZFS) parameters *D* and *E* and its space orientation with respect to the field, $\boldsymbol{B}$. The angular dependence formulae in an arbitrary frame of reference can be found in references [128,129]. We assume that the TT pair is held together by a small exchange interaction $X\vec{S}_1 \cdot \vec{S}_2$ (X<<*D*,*E*) and write the TT Hamiltonian in a magnetic field, $\vec{B}$ as,

$$H_{TT} = \sum_{j=1}^{2} [g_j \mu_B \vec{S}_j \cdot \vec{B} + \vec{S}_j \cdot \tilde{\tau}_j \cdot \vec{S}_j] + \mathrm{X}\vec{\mathrm{S}}_1 \cdot \vec{\mathrm{S}}_2 \quad , \qquad \text{(A.2)}$$

where g_j is the g-factor of each triplet S_j=1, $\boldsymbol{B}$ is the magnetic field, and μ_B is Bohr magneton. A pair of triplets may assume a state of total angular momentum $\vec{S}_{TT} = \vec{S}_1 + \vec{S}_2$ (with S_{TT}=0,1,2) and for the SF process, we concentrate on the case $\vec{S}_{TT} = 0$. In the absence of magnetic field, *B*=0, three of the nine TT states have a singlet character [130]; however, when *B* increases the distribution of singlet character among the nine states, changes leading to variations in the initially populated levels by the SF process. As time progresses and with spin-dependent decay, the total population of the SF-born TT pair becomes magnetic field-dependent [119] rendering a field-dependent photoexcitations density related to PA, namely MPA(*B*). The spin-dependent level decay rate is given by:

$$\gamma_n = \sum_{\alpha} \kappa_{\alpha} P_{nn}^{\alpha}, \tag{A.3}$$

where n=1,…,9 is the level index of the TT state; α=S,T,Q is the spin configuration index for singlet, triplet and quintet; κ_{α} is the characteristic configuration decay rate; and P_{nn}^{α} is the α projection onto the n^{th} level. In Figure 4.3, we show the magnetic field-dependent energy levels of a TT pair and the singlet character of each level for two magnetic field orientations; it is clearly seen that the spread of the singlet character among the nine TT levels depends on both the magnitude and orientation of the magnetic field.

When we incorporate the level decay rates into consideration, we find for the time-dependent probability of the system in the α^{th} spin configuration:

$$\rho_{\alpha}(t) = Tr(P^{\alpha}\sigma(t)) = \frac{L_{\alpha}}{9} \sum_{n,m=1}^{9} P_{nm}^{\alpha} P_{mn}^{S} \cos(\omega_{mn} t) \exp(-\gamma_{mn} t) \quad , \tag{A.4}$$

where $E_n = \hbar\omega_n$ are the level energies, $\omega_{nm} = \omega_n - \omega_m$; $\gamma_{nm} = \gamma_n + \gamma_m$ and $L_{\alpha} = 1,3,5$ for α=S,T,Q, respectively. In equation (A.4), P^{α} is α-configuration projection operator and $\sigma(t)$ is the time-dependent density operator with $\sigma(0) = P^{S}$ for the SF process. Importantly, when the decay rates κ_{α} are spin-dependent, γ_{nm} in equation (A.4) are not uniform and the decay of $\rho_{\alpha}(t)$ becomes spin-dependent; this assures a finite magnetic field effect (or MPA(*B*) response).

Transient-PA (t-PA) measures the optical transition from the TT state to an excited state and is therefore proportional to $\sum_{\alpha} R_{\alpha}\rho_{\alpha}(t,B)$ where $\rho_{\alpha}(t,B)$ is given by equation

(A.4) and R_α is the transition probability for configuration α. Therefore, t-MPA(*B*) response is given by:

$$tMPA(t,B) = \frac{\sum R_\alpha \rho_\alpha(t,B)}{\sum R_\alpha \rho_\alpha(t,0)} - 1, \tag{A.5}$$

In contrast, steady state PA measures the time integrated optical transition, and is thus given by

$$\begin{aligned} &PA(B) \propto \sum_\alpha \int_0^{t_0} R_\alpha \rho_\alpha(t,B)dt = \\ &\sum_{\alpha mn} R_\alpha L_\alpha P_{nm}^\alpha P_{mn}^S \frac{\gamma_{nm}}{\gamma_{nm}^2 + \omega_{nm}^2}[1 - e^{-\gamma_{nm}t_0}(\cos\gamma_{nm}t_0 - \frac{\omega_{nm}}{\gamma_{nm}}\sin\omega_{nm}t_0)] \end{aligned} \tag{A.6}$$

where $t_0 \sim \tau_{SL}$ is the time during which the system spin is conserved. MPA(*B*) response is defined as,

$$MPA(B) = \frac{PA(B) - PA(0)}{PA(0)}, \tag{A.7}$$

Comparing equations (A.4) and (A.6) we may expect different field-responses for the transient and steady state MPA(*B*). Figure 4.4 shows the two responses for parameters relevant to the pristine copolymer studied. For these calculations, we performed a full 'double average' on the angle, β, between the two triplets comprising the TT pair and θ, the angle between one of them and the magnetic field direction. As we can see, the t-MPA is broad and does not contain an abrupt change at *B*=0. In contrast, the ss-MPA

response develops a sharp feature at ~ B=0; this shape was taken in the literature as evidence for SF.

A.2 ss-MPA(B) Response Related to Isolated Triplet Exciton

In order to describe the photoexcitation density dynamics, we introduce a relaxation term, H_R, in the spin Hamiltonian [128] ,

$$H = H_Z + H_{HF} + H_R \ , \tag{A.8}$$

where H_R is the non-Hermitian relaxation term that describes the decay pathways of the spin sub-levels:

$$H_R = -i\frac{\hbar}{2}\sum_{\alpha=1}^{L}\kappa_\alpha P^\alpha \ , \tag{A.9}$$

where P^a ($\sum P^\alpha = \tilde{1}$) are the relevant state projection operators. In equation (A.8) the Zeeman term is $H_Z = \mu_B \sum_n g_n \vec{S}_n \cdot \vec{B}$, where the summation is over all species (1 for a single triplet exciton, TE) with spin S and (assumed) isotropic g-factor; $H_{HF} = \sum_n a_n \vec{I}_n \cdot \vec{S}_n$ is the isotropic HFI term; we also assume that the exchange interaction can be ignored. The time evolution of the density operator is now expressed as,

$$\sigma(t) = \exp(-iHt/\hbar)\sigma(0)\exp(iH^{\dagger}t/\hbar)\,, \tag{A.10}$$

where $H^{\dagger}$ is the Hermitian conjugate of H, and the t=0 density matrix $\sigma(0)$ is controlled by the generation process. The time-dependent probability for the system to be in the α^{th} spin state may now be written as

$$\rho_{\alpha}(t) = Tr(P^{\alpha}\sigma(t)) = \frac{L}{M}\sum_{n,m} P^{\alpha}_{n,m}\sigma_{m,n}(0)\cos(\omega_{mn}t)\exp(-\gamma_{mn}t)\,, \tag{A.11}$$

where $E_n = \hbar(\omega_n - i\gamma_n)$ (n=1,…M) are the complex eigen-values of the non-Hermitian *H*, M=L(2I+1)^2 is the total number of states, and $\omega_{nm} = \omega_n - \omega_m$; $\gamma_{nm} = \gamma_n + \gamma_m$. The measured ss-MPA(*B*) response may be readily calculated using equation (A.11). Let R_{α} be the reaction rate constant, then the total yield of the reaction is

$$\Phi_R = \sum_{\alpha}\int_0^{\infty} R_{\alpha}\rho_{\alpha}(t)dt = \frac{L}{M}\sum_{\alpha} R_{\alpha}\sum_{n,m} P^{\alpha}_{n,m}\sigma_{m,n}(0)\,\frac{\gamma_{nm}}{\gamma_{nm}^2 + \omega_{nm}^2}\,. \tag{A.12}$$

For PA, assuming that the optical cross section is spin-independent, $R_{\alpha}\equiv R$ and equation (A.12) yields $\Phi_{PA} = R\sum_{\alpha}\int\rho_{\alpha}(t)dt = (2RL/M)\sum_n \sigma_{nn}(0)/\gamma_n \propto N_{SS}$, the TE density.

In pristine PDTP-DFBT films, the steady state photoexcited TE density is low and thus effects of TE-TE annihilation are small. In this case, the TE density is determined by a nonradiative recombination process, for which the spin sub-level recombination constants κ_{α} (α=±1,0) are different from each other. The principal TE zero-field splitting

(ZFS) parameters were obtained in PDTP-DFBT by the PL detected magnetic resonance technique; D≈38 mT and E≈15 mT. Using these ZFS parameters, we calculated the TE energy levels and wavefunctions in ***B*** applied in a general direction. The MPA(*B*) powder pattern (Figure 3.2d) was calculated using $\kappa_1=\kappa_{-1}= 0.25\kappa_0=1.3x10^7 s^{-1}$.

REFERENCES

[1] H. Shirakawa, E. J. Louis, A. G. MacDiarmid, C. K. Chiang, and A. J. Heeger, J. Chem. Soc., Chem. Commun. **16**, 578 (1977).

[2] C. K. Chiang, C. Fincher Jr, Y. Park, A. Heeger, H. Shirakawa, E. Louis, S. Gau, and A. G. MacDiarmid, Physical Review Letters **39**, 1098 (1977).

[3] J. Burroughes, D. Bradley, A. Brown, R. Marks, K. Mackay, R. Friend, P. Burns, and A. Holmes, Nature **347**, 539 (1990).

[4] D. Braun and A. J. Heeger, Applied Physics Letters **58**, 1982 (1991).

[5] N. Sariciftci, L. Smilowitz, A. J. Heeger, and F. Wudl, Science **258**, 1474 (1992).

[6] J. Peet, J. Kim, N. E. Coates, W. L. Ma, D. Moses, A. J. Heeger, and G. C. Bazan, Nature Materials **6**, 497 (2007).

[7] Z. Bao and J. Locklin, *Organic field-effect transistors* (CRC press, 2007).

[8] Z. Xiong, D. Wu, Z. V. Vardeny, and J. Shi, Nature **427**, 821 (2004).

[9] V. Dediu, M. Murgia, F. Matacotta, C. Taliani, and S. Barbanera, Solid State Communications **122**, 181 (2002).

[10] M. Gerard, A. Chaubey, and B. Malhotra, Biosensors and Bioelectronics **17**, 345 (2002).

[11] S. W. Thomas, G. D. Joly, and T. M. Swager, Chemical Reviews **107**, 1339 (2007).

[12] M. Chandross, S. Mazumdar, S. Jeglinski, X. Wei, Z. Vardeny, E. Kwock, and T. Miller, Physical Review B **50**, 14702 (1994).

[13] P. Atkins and J. De Paula, Oxford University Press, ca **57**, 80.

[14] N. W. Ashcroft and N. D. Mermin, *Solid State Physics* (Holt, Rinehart and Winston, New York, 1976).

[15] M. Pope and C. E. Swenberg, *Electronic processes in organic crystals* (Clarendon Press Oxford, 1982), Vol. 1.

[16] A. Köhler and D. Beljonne, Advanced Functional Materials **14**, 11 (2004).

[17] D. Guo, S. Mazumdar, S. Dixit, F. Kajzar, F. Jarka, Y. Kawabe, and N. Peyghambarian, Phys. Rev. B **48**, 1433 (1993).

[18] W. Barford, *Electronic and optical properties of conjugated polymers* (Oxford University Press, 2005), 129.

[19] K. Wong, C. Lee, and B. Tang, Synthetic Metals **101**, 505 (1999).

[20] S. Califano, *Vibrational states* (Wiley London, 1976).

[21] G. D. Scholes, D. S. Larsen, G. R. Fleming, G. Rumbles, and P. L. Burn, Physical Review B **61**, 13670 (2000).

[22] T. E. Dykstra, V. Kovalevskij, X. Yang, and G. D. Scholes, Chemical Physics **318**, 21 (2005).

[23] X. Yang, T. E. Dykstra, and G. D. Scholes, Physical Review B **71**, 045203 (2005).

[24] Y. Liang, Z. Xu, J. Xia, S. T. Tsai, Y. Wu, G. Li, C. Ray, and L. Yu, Advanced Materials **22**, E135 (2010).

[25] L. Dou, C.-C. Chen, K. Yoshimura, K. Ohya, W.-H. Chang, J. Gao, Y. Liu, E. Richard, and Y. Yang, Macromolecules **46**, 3384 (2013).

[26] R. E. Peierls, *Quantum theory of solids* (Clarendon, 1955).

[27] H. R. Zeller, in *Festkörperprobleme 13* (Springer, 1973), pp. 31.

[28] W.-P. Su, J. Schrieffer, and A. Heeger, Physical Review B **22**, 2099 (1980).

[29] S. Frolov, Z. Bao, M. Wohlgenannt, and Z. Vardeny, Physical Review B **65**, 205209 (2002).

[30] R. Farchioni and G. Grosso, Springer Ser. Mater. Sci **41** (2001).

[31] A. J. Heeger, Angewandte Chemie International Edition **40**, 2591 (2001).

[32] C. Kittel and P. McEuen, *Introduction to solid state physics* (Wiley New York, 1976), Vol. 8.

[33] V. Coropceanu, J. Cornil, D. A. da Silva Filho, Y. Olivier, R. Silbey, and J.-L. Brédas, Chemical Reviews **107**, 926 (2007).

[34] M. Winokur, P. Wamsley, J. Moulton, P. Smith, and A. Heeger, Macromolecules **24**, 3812 (1991).

[35] Y. Shirota and H. Kageyama, Chemical Reviews **107**, 953 (2007).

[36] T. D. Nguyen, G. Hukic-Markosian, F. Wang, L. Wojcik, X.-G. Li, E. Ehrenfreund, and Z. Vardeny, in *SPIE NanoScience+ Engineering* (International Society for Optics and Photonics, 2010), pp. 77601A.

[37] V. Dyakonov and E. Frankevich, Chemical Physics **227**, 203 (1998).

[38] H. Hayashi, *Introduction to dynamic spin chemistry* (World Scientific, 2004).

[39] F. Hide, M. A. DÍaz-GarcÍa, B. J. Schwartz, and A. J. Heeger, Accounts of Chemical Research **30**, 430 (1997).

[40] M. Chandross, S. Mazumdar, M. Liess, P. Lane, Z. Vardeny, M. Hamaguchi, and K. Yoshino, Physical Review B **55**, 1486 (1997).

[41] J. Leng, S. Jeglinski, X. Wei, R. Benner, Z. Vardeny, F. Guo, and S. Mazumdar, Physical Review Letters **72**, 156 (1994).

[42] J. J. Burdett, A. M. Müller, D. Gosztola, and C. J. Bardeen, The Journal of Chemical Physics **133**, 144506 (2010).

[43] J. Lee, P. Jadhav, and M. Baldo, Applied Physics Letters **95**, 033301 (2009).

[44] A. Rao, M. W. Wilson, J. M. Hodgkiss, S. Albert-Seifried, H. Bassler, and R. H. Friend, Journal of the American Chemical Society **132**, 12698 (2010).

[45] J. C. Johnson, A. J. Nozik, and J. Michl, Journal of the American Chemical Society **132**, 16302 (2010).

[46] C. Wang and M. J. Tauber, Journal of the American Chemical Society **132**, 13988 (2010).

[47] E. Busby, J. Xia, Q. Wu, J. Z. Low, R. Song, J. R. Miller, X. Y. Zhu, Luis M. Campos, and M. Y. Sfeir, Nat. Mater. **advance online publication** (2015).

[48] R. Hosteny, T. Dunning Jr, R. Gilman, A. Pipano, and I. Shavitt, The Journal of Chemical Physics **62**, 4764 (1975).

[49] N. Geacintov, M. Pope, and F. Vogel, Physical Review Letters **22**, 593 (1969).

[50] R. Groff, P. Avakian, and R. Merrifield, Physical Review B **1**, 815 (1970).

[51] A. Kazzaz and A. Zahlan, The Journal of Chemical Physics **48**, 1242 (1968).

[52] J. C. Johnson, A. J. Nozik, and J. Michl, Accounts of Chemical Research **46**, 1290 (2013).

[53] W.-L. Chan, M. Ligges, and X. Zhu, Nat. Chem. **4**, 840 (2012).

[54] M. B. Smith and J. Michl, Ann. Rev. Phys. Chem. **64**, 361 (2013).

[55] D. Beljonne, H. Yamagata, J. Brédas, F. Spano, and Y. Olivier, Phys. Rev. Lett. **110**, 226402 (2013).

[56] A. J. Musser, M. Al-Hashimi, M. Maiuri, D. Brida, M. Heeney, G. Cerullo, R. H. Friend, and J. Clark, Journal of the American Chemical Society **135**, 12747 (2013).

[57] D. Kearns and M. Calvin, Journal of Chemical Physics **29** (1958).

[58] G. Delacote, J. Fillard, and F. Marco, Solid State Communications **2**, 373 (1964).

[59] C. W. Tang, Applied Physics Letters **48**, 183 (1986).

[60] D. E. Markov, E. Amsterdam, P. W. Blom, A. B. Sieval, and J. C. Hummelen, The Journal of Physical Chemistry A **109**, 5266 (2005).

[61] J. Halls, K. Pichler, R. Friend, S. Moratti, and A. Holmes, Applied Physics Letters **68**, 3120 (1996).

[62] G. Yu and A. J. Heeger, Journal of Applied Physics **78**, 4510 (1995).

[63] J. Halls, C. Walsh, N. Greenham, E. Marseglia, R. Friend, S. Moratti, and A. Holmes, Applied Physics Letters **68**, 3120 (1996).

[64] B. Hu and Y. Wu, Nature Materials **6**, 985 (2007).

[65] P. Bobbert, T. Nguyen, F. Van Oost, v. B. Koopmans, and M. Wohlgenannt, Physical Review Letters **99**, 216801 (2007).

[66] F. Bloom, W. Wagemans, M. Kemerink, and B. Koopmans, Physical Review Letters **99**, 257201 (2007).

[67] F. Bloom, M. Kemerink, W. Wagemans, and B. Koopmans, Physical Review Letters **103**, 066601 (2009).

[68] J. Bergeson, V. Prigodin, D. Lincoln, and A. Epstein, Physical Review Letters **100**, 067201 (2008).

[69] Ö. Mermer, G. Veeraraghavan, T. Francis, Y. Sheng, D. Nguyen, M. Wohlgenannt, A. Köhler, M. Al-Suti, and M. Khan, Physical Review B **72**, 205202 (2005).

[70] P. Desai, P. Shakya, T. Kreouzis, W. Gillin, N. Morley, and M. Gibbs, Physical Review B **75**, 094423 (2007).

[71] S. Majumdar, H. S. Majumdar, H. Aarnio, and R. Österbacka, physica status solidi (RRL)-Rapid Research Letters **3**, 242 (2009).

[72] T. Nguyen, Y. Sheng, J. Rybicki, and M. Wohlgenannt, Physical Review B **77**, 235209 (2008).

[73] T. D. Nguyen, G. Hukic-Markosian, F. Wang, L. Wojcik, X.-G. Li, E. Ehrenfreund, and Z. V. Vardeny, Nature Materials **9**, 345 (2010).

[74] V. Prigodin, J. Bergeson, D. Lincoln, and A. Epstein, Synthetic Metals **156**, 757 (2006).

[75] Y. Iwasaki, T. Osasa, M. Asahi, M. Matsumura, Y. Sakaguchi, and T. Suzuki, Physical Review B **74**, 195209 (2006).

[76] Y. Wu, Z. Xu, B. Hu, and J. Howe, Physical Review B **75**, 035214 (2007).

[77] B. R. Gautam, T. D. Nguyen, E. Ehrenfreund, and Z. V. Vardeny, Physical Review B **85**, 205207 (2012).

[78] B. R. Gautam, T. D. Nguyen, E. Ehrenfreund, and Z. V. Vardeny, Journal of Applied Physics **113**, 143102 (2013).

[79] S. Singh, B. Pandit, T. P. Basel, S. Li, D. Laird, and Z. V. Vardeny, Phys. Rev. B **85**, 205206 (2012).

[80] S. V. Frolov, University of Utah, 1997.

[81] A. Lohner, P. Kruck, and W. Rühle, Applied Physics B **59**, 211 (1994).

[82] S. Singh, University of Utah, 2010.

[83] B. R. Gautam, University of Utah, 2013.

[84] N. S. Sariciftci, *Primary photoexcitations in conjugated polymers: molecular exciton versus semiconductor band model* (World Scientific, 1997).

[85] F. Schindler, J. M. Lupton, J. Müller, J. Feldmann, and U. Scherf, Nature Materials **5**, 141 (2006).

[86] F. Rohlfing, T. Yamada, and T. Tsutsui, Journal of Applied Physics **86**, 4978 (1999).

[87] Z. He, B. Xiao, F. Liu, H. Wu, Y. Yang, S. Xiao, C. Wang, T. P. Russell, and Y. Cao, Nature Photonics **9**, 174 (2015).

[88] R. Tautz *et al.*, Nature Communications **3**, 970 (2012).

[89] J. M. Szarko, B. S. Rolczynski, S. J. Lou, T. Xu, J. Strzalka, T. J. Marks, L. Yu, and L. X. Chen, Advanced Functional Materials **24**, 10 (2014).

[90] P. Lane, X. Wei, and Z. Vardeny, Physical Review Letters **77**, 1544 (1996).

[91] T. Basel, U. Huynh, T. Zheng, T. Xu, L. Yu, and Z. V. Vardeny, Advanced Functional Materials **25**, 1895 (2015).

[92] T. Drori, J. Holt, and Z. Vardeny, Phys. Rev. B **82**, 075207 (2010).

[93] R. Tautz *et al.*, Nat. Commun. **3**, 970 (2012).

[94] J. You *et al.*, Nat. Commun. **4**, 1446 (2013).

[95] C. X. Sheng, S. Singh, A. Gambetta, T. Drori, M. Tong, S. Tretiak, and Z. V. Vardeny, Sci. Rep. **3** (2013).

[96] M. Rohlfing and S. G. Louie, Phys. Rev. Lett. **82**, 1959 (1999).

[97] S. Frolov, Z. Bao, M. Wohlgenannt, and Z. Vardeny, Phys. Rev. Lett. **85**, 2196 (2000).

[98] M. Liess, S. Jeglinski, Z. Vardeny, M. Ozaki, K. Yoshino, Y. Ding, and T. Barton, Phys. Rev. B **56**, 15712 (1997).

[99] X. Wei, B. Hess, Z. Vardeny, and F. Wudl, Phys. Rev. Lett. **68**, 666 (1992).

[100] P. Lane, J. Shinar, and K. Yoshino, Phys. Rev. B **54**, 9308 (1996).

[101] A. Monkman, H. Burrows, L. Hartwell, L. Horsburgh, I. Hamblett, and S. Navaratnam, Phys. Rev. Lett. **86**, 1358 (2001).

[102] N. Geacintov, M. Pope, and F. Vogel, Phys. Rev. Lett. **22**, 593 (1969).

[103] M. Chandross and S. Mazumdar, Phys. Rev. B **55**, 1497 (1997).

[104] G. Grancini, M. Maiuri, D. Fazzi, A. Petrozza, H. Egelhaaf, D. Brida, G. Cerullo, and G. Lanzani, Nat. Mater. **12**, 29 (2013).

[105] W.-L. Chan, M. Ligges, A. Jailaubekov, L. Kaake, L. Miaja-Avila, and X.-Y. Zhu, Science **334**, 1541 (2011).

[106] W.-L. Chan, T. C. Berkelbach, M. R. Provorse, N. R. Monahan, J. R. Tritsch, M. S. Hybertsen, D. R. Reichman, J. Gao, and X.-Y. Zhu, Accounts of Chemical Research **46**, 1321 (2013).

[107] E. C. Greyson, J. Vura-Weis, J. Michl, and M. A. Ratner, The Journal of Physical Chemistry B **114**, 14168 (2010).

[108] T. Zeng, R. Hoffmann, and N. Ananth, Journal of the American Chemical Society **136**, 5755 (2014).

[109] T. Basel, University of Utah, 2014.

[110] A. Abragan and B. Bleany, *Electron paramagnetic resonance of transient metal ions* (Claredon Press, Oxford, 1970).

[111] A. Rao, M. W. Wilson, J. M. Hodgkiss, S. Albert-Seifried, H. Bässler, and R. H. Friend, Journal of the American Chemical Society **132**, 12698 (2010).

[112] D. N. Congreve *et al.*, Science **340**, 334 (2013).

[113] R. Österbacka, C. An, X. Jiang, and Z. Vardeny, Science **287**, 839 (2000).

[114] K. Aryanpour, J. Munoz, and S. Mazumdar, J. Phys. Chem. C **117**, 4971 (2013).

[115] M. Hallermann, I. Kriegel, E. Da Como, J. M. Berger, E. Von Hauff, and J. Feldmann, Adv.Func. Mater. **19**, 3662 (2009).

[116] J. Piris, T. E. Dykstra, A. A. Bakulin, P. H. v. Loosdrecht, W. Knulst, M. T. Trinh, J. M. Schins, and L. D. Siebbeles, J. Phys. Chem. C **113**, 14500 (2009).

[117] Y. Zhang, T. P. Basel, B. R. Gautam, X. Yang, D. J. Mascaro, F. Liu, and Z. V. Vardeny, Nat. Commun. **3**, 1043 (2012).

[118] Y. Zhang, B. R. Gautam, T. P. Basel, D. J. Mascaro, and Z. V. Vardeny, Synthetic Metals **173**, 2 (2013).

[119] G. B. Piland, J. J. Burdett, D. Kurunthu, and C. J. Bardeen, J. Phys. Chem. C **117**, 1224 (2013).

[120] S. Li, T. F. George, X.-L. He, B.-P. Xie, and X. Sun, J. Phys. Chem. B **113**, 400 (2008).

[121] P. J. Jadhav *et al.*, Adv. Mater. **24**, 6169 (2012).

[122] S. R. Yost *et al.*, Nat. Chem. **6**, 492 (2014).

[123] J. J. Burdett and C. J. Bardeen, J. Am. Chem. Soc. **134**, 8597 (2012).

[124] F. Wang, H. Bässler, and Z. V. Vardeny, Phys. Rev. Lett. **101**, 236805 (2008).

[125] S. Majumdar, H. S. Majumdar, H. Aarnio, D. Vanderzande, R. Laiho, and R. Österbacka, Phys. Rev. B **79**, 201202 (2009).

[126] M. Tabachnyk, B. Ehrler, S. Gélinas, M. L. Böhm, B. J. Walker, K. P. Musselman, N. C. Greenham, R. H. Friend, and A. Rao, Nat. Mater. **13**, 1033 (2014).

[127] A. J. Musser, M. Liebel, C. Schnedermann, T. Wende, T. B. Kehoe, A. Rao, and P. Kukura, Nature Physics (2015).

[128] E. Ehrenfreund and Z. V. Vardeny, Israel Journal of Chemistry **52**, 552 (2012).

[129] A. Abragam and B. Bleaney, *Electron paramagnetic resonance of transition ions* (Oxford University Press, 2012).

[130] R. Merrifield, Pure and Applied Chemistry **27**, 481 (1971).